POLITECNICO DI TORINO

Master Degree in Ingegneria Meccanica (Mechanical Engineering)

Master Degree Thesis

Theoretical and experimental analysis of a TMD device for over head power transmission lines

Academic Tutor

Alessandro Fasana

Student

Giuseppe Vecchio

Academic Year 2021 - 2022

Contents

List of Figures

[1]C. Gazzola, *Modelling and assessment of aeolian vibrations of overhead transmission line conductors: theory and implementation*, PhD Thesis, Polytechnic of Milan, Italy, 2017.

[2]C. Gazzola, *Modelling and assessment of aeolian vibrations of overhead transmission line conductors: theory and implementation*, PhD Thesis, Polytechnic of Milan, Italy, 2017.

[3]Spedona/J.H. Mora, *Lignes à haute tension (Sagy, Val d'Oise),* 16 June 2005, in `https://bit.ly/34UxhaU`.

[4]C. Gazzola, *Modelling and assessment of aeolian vibrations of overhead transmission line conductors: theory and implementation*, PhD Thesis, Polytechnic of Milan, Italy, 2017.

[5]M. Onore, *Smorzatore Stockbridge e soppressione delle vibrazioni dei cavi tesi: analisi numerica e sperimentale*, Polytechnic of Turin, 2018.

[6]D. Bryant, *ACSR and ACCC,* 3 September 2013, in `https://bit.ly/3HRLzrs`.

[7]Electric Research Power Institute EPRI, *Transmission Line Reference Book: Wind- Induced Conductor Motion*, Palo Alto, 2006.

[8]M. Buscemi, *Studio di un Sistema di Controllo Attivo per la Riduzione delle Vibrazioni nelle Linee Aeree di Trasmissione dell'Energia Elettrica*, MA thesis, Polytechnic of Milan, Italy, 1985.

[9]Liang Wang Xiaoyu Luo and Yisheng Zhang, *Nonlinear numerical model with contact for Stockbridge vibration damper and experimental validation*, Journal of Vibration and Control, 2014.

[10]M. Onore, *Smorzatore Stockbridge e soppressione delle vibrazioni dei cavi tesi: analisi numerica e sperimentale*, Polytechnic of Turin, 2018.
[11]M. Onore, *Smorzatore Stockbridge e soppressione delle vibrazioni dei cavi tesi: analisi numerica e sperimentale*, Polytechnic of Turin, 2018.
[12]M. Onore, *Smorzatore Stockbridge e soppressione delle vibrazioni dei cavi tesi: analisi numerica e sperimentale*, Polytechnic of Turin, 2018.
[13]M. Onore, *Smorzatore Stockbridge e soppressione delle vibrazioni dei cavi tesi: analisi numerica e sperimentale*, Polytechnic of Turin, 2018.
[14]M. Onore, *Smorzatore Stockbridge e soppressione delle vibrazioni dei cavi tesi: analisi numerica e sperimentale*, Polytechnic of Turin, 2018.
[15]M. Onore, *Smorzatore Stockbridge e soppressione delle vibrazioni dei cavi tesi: analisi numerica e sperimentale*, Polytechnic of Turin, 2018.
[16]M. Onore, *Smorzatore Stockbridge e soppressione delle vibrazioni dei cavi tesi: analisi numerica e sperimentale*, Polytechnic of Turin, 2018.
[17]M. Onore, *Smorzatore Stockbridge e soppressione delle vibrazioni dei cavi tesi: analisi numerica e sperimentale*, Polytechnic of Turin, 2018.

Abstract

The most common technology in the world for the construction of power transmission over head lines is via suspended conductors attached to towers. As one can easily imagine, these conductors are subjected to vibrations induced by wind. The magnitude of the induced vibrations depends on the cable-wind interaction, but it's pretty right saying that it becomes more dangerous especially when the line is in open spaces without natural obstacles (e.g. deserts, lakes, frees plains) due to possible presence of laminar wind. With the scope of reducing the magnitude of this kind of vibrations and protect the line (and the users) from out of service, many type of dampers have been designed during the years.

The thesis presented in this document analyses one of the most common devices used for this scope: a tuned mass damper invented in the '20s by G. H. Stockbridge, from who inherited its common name "Stockbridge" still used nowadays. This damper can cover a range from few Hz up to maximum 200Hz with amplitude normally less than 100mm, the so called range of Aeolian vibrations, excited by shedding of vortices in the vertical plane: it is this alternative motion in the vertical plan to cause a fatigue stress to the conductor.

The investigation focuses on both modelling and experimental study of this mechanical device: the aim is obtaining the mathematical expression for the *Frequency Response Function* (FRF) of the damper in order to have a powerful tool for optimizing its design with a sensitive analysis, and correlate the FRF parameters thanks to the experimental data obtained in the lab tests of a prototypal damper on the shaker. All the analyses are developed in collaboration with "Officina F.lli Bertolotti" S.p.A., an Italian company with long experience in manufacturing of fittings for power transmission over head lines, and with the Politecnico di Torino, Dynamics & Identification Research Group.

1. State of the art

In the practice, the energy net provider establishes both the mechanical and electrical characteristics of the power transmission line based on available data on the boundary conditions like wind, ground morphology, voltage, power consumption etc., and so for all the fittings and dampers too. For the dampers, this commonly reduces to a target FRF with thresholds on both gain and phase set in order to guarantee the robustness against wind-correlate fatigue phenomena. Here below is shown an example of such FRF for a Stockbridge type damper.

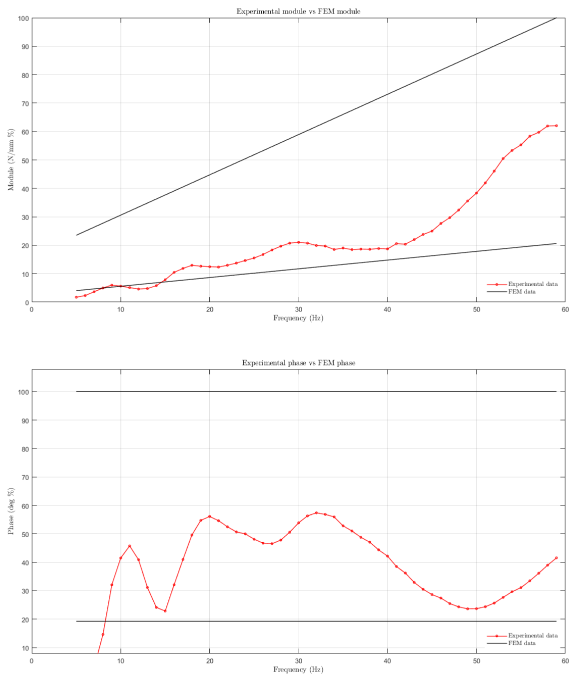

Figure 1.1: Example of the FRF limits required

Therefore, it is necessary to observe the flow characteristics between the air and the power line conductors, as well as the mechanical and technological properties of the system parts, in order to understand the physics that governs the studied situation.

1.1 Wind - Induced Vibration

In the dynamic of air transmission lines, the *wind - induced vibrations* play a significant role; these motions are produced by the wind interaction with the conductors, so there is an energy shift that produces motions of the conductors.

Aeolian Vibrations, *Galloping Motions*, and *Subspan Oscillations* are three of the main kinds of motion described in literature.

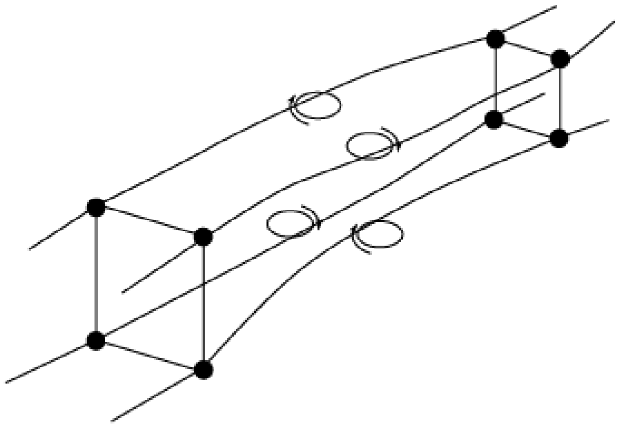

Figure 1.2: Rappresentation of *Wind - Induced Vibrations*[1]

The *Aeolian vibration* are the most common type of dynamic vibration; they are generated by the interaction between the smooth wind, by 1 m/s up to 7 m/s of velocity, with the conductor. The amplitude exceeding the conductor diameter can be experienced with this vibration that has a frequency of 3-150 Hz.

A vortex shedding phenomenon can create dangerous alternating forces between conductors. This can result in bending moments of the conductors for many cycles,

[1]C. Gazzola, *Modelling and assessment of aeolian vibrations of overhead transmission line conductors: theory and implementation*, PhD Thesis, Polytechnic of Milan, Italy, 2017.

causing fatigue stress[2][3][4]. Specifically, when the wind meets the cable, von Karman wakes are created; these vortices are responsible for causing vibrations to occur (see the Figure 1.3). The consequent pressure gradients around the cylindrical cable reflect the presence of periodic lift forces.

According to the Strouhal formula (Equation 1.1)[5][6][7], these are proportional to the wind velocity (V) and the Strouhal number (directly linked to the Reynolds number) and inversely proportional to the conductor diameter (D):

$$f_{VS} = S \cdot \frac{V}{D} \tag{1.1}$$

According to the appropriate wind velocity, the Reynolds number can be by 750 to 6000, while the Strouhal number range is 0.18 to 0.22[8]; analysing the Strouhal formula, it is possible to notice that for low frequencies correspond large conductor diameter and low wind velocity, while for high frequencies correspond small conductor diameter and a high wind velocity.

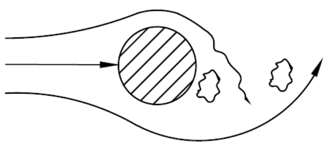

Figure 1.3: von Karman wakes, $150 < Re < 3 \cdot 10^5$ case[9]

[2]Electric Research Power Institute EPRI, *Transmission Line Reference Book: Wind- Induced Conductor Motion*, Palo Alto, 2006.

[3]O. Barry et al., *Analytical and Experimental Investigation of Overhead Transmission Line Vibration*, In: Journal of Vibration and Control 21, 2014, pp. 2825–2837.

[4]N. Barbieri and R. Barbieri, *Linear and Non-Linear Analysis of Stockbridge Damper*, In: Proc. of the 21st Brazilian Congress of Mechanical Engineering, Natal, RN, Brazil. Ed. by Proceedings of COBEM, 2011.

[5]Electric Research Power Institute EPRI, *Transmission Line Reference Book: Wind- Induced Conductor Motion*, Palo Alto, 2006.

[6]M. Ervik et al., *Report on Aeolian Vibration*, In: Electra 124, 1986, pp. 40–77.

[7]P. Hagedorn, *Wind-Excited Vibrations of Transmission Lines: A Comparison of Different Mathematical Models*, In: Mathematical Modelling 8, 1987, pp. 352–358.

[8]C. Gazzola, *Modelling and assessment of aeolian vibrations of overhead transmission line conductors: theory and implementation*, PhD Thesis, Polytechnic of Milan, Italy, 2017.

[9]C. Gazzola, *Modelling and assessment of aeolian vibrations of overhead transmission line conductors: theory and implementation*, PhD Thesis, Polytechnic of Milan, Italy, 2017.

1.2 Conductors

The Stockbridge damper is designed so that can absorb and dissipate the energy transmitted from the external environment to the overhead lines; in order to have a better overview of the physic that governs the Stockbridge dampers, a brief description of the conductors characteristics and their properties are reported. It is important to know that the conductor is the most important component of a power transmission line: in fact it covers about 40 % of the total power line cost[10][11] and that any effort in preventing its damaging must be done in order to avoid possible out of service condition for million euros cost.

Figure 1.4: Typical typologies of power lines[12]

1.2.1 Construction Characteristics

The typical structure of the conductor is shown in Figure 1.5. A conductor is made up of a series of layers of braided wires forming two parts[13]:

[10]Electric Research Power Institute EPRI, *Transmission Line Reference Book: Wind- Induced Conductor Motion*, Palo Alto, 2006.

[11]C. Gazzola, *Modelling and assessment of aeolian vibrations of overhead transmission line conductors: theory and implementation*, PhD Thesis, Polytechnic of Milan, Italy, 2017.

[12]Spedona/J.H. Mora, *Lignes à haute tension (Sagy, Val d'Oise),* 16 June 2005, in `https://bit.ly/34UxhaU`.

[13]Donald G. Fink and H. Wayne Beaty, *Overhead Power Transmission". Standard Handbook for Electrical Engineers (11 ed.)* New York: McGraw-Hill, 1978.

- An external layer, typically in aluminum and its alloys, with high conductivity capacity, called the conductive layer;
- An internal layer in steel or other materials with higher strength capacity than aluminum, called core, which resists the most part of the mechanical pulling;

The two layers could have sub layers, each helically wrapped with a specific β_L angle (Figure 1.6). Every layer is orientated in opposite direction to ensure its global integrity.

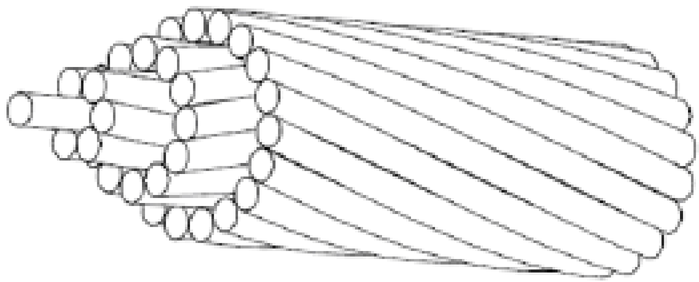

Figure 1.5: Typical conductor structure[14]

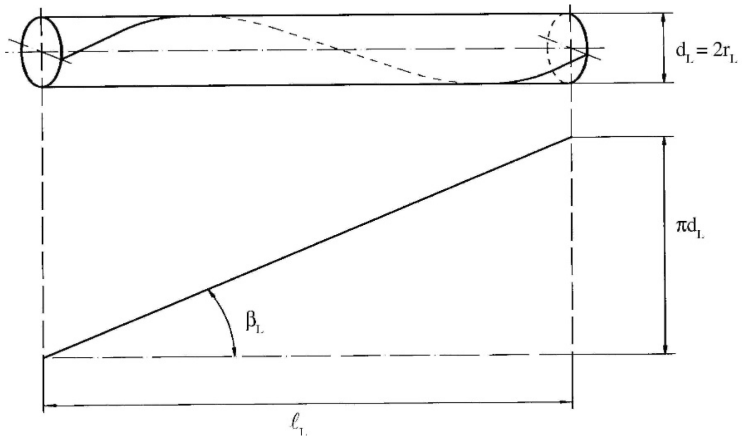

Figure 1.6: Stranded winding in a helical direction on the core[15]

[14]C. Gazzola, *Modelling and assessment of aeolian vibrations of overhead transmission line conductors: theory and implementation*, PhD Thesis, Polytechnic of Milan, Italy, 2017.

The conductor must provide both high conductive and mechanical strength properties, in order to cover decades of non-interrupted service, but also other particular aspects mainly linked to the minimum height of the conductor from the ground.

In particular, regarding the tension to linear mass ratio (catenary constant) is of fundamental importance for the catenary shape of the conductor: its value affects directly the height of the lowest point of a span. The proper combination of mechanical pulling and linear mass must be found to obtain lower power losses (high pulling) and correct catenary shape.

The thermal expansion coefficient is also relevant because it affects the vertical displacement among the lower and the higher points of the line; the higher is the thermal expansion coefficient, the higher will be the cable deformation when temperature variations occurs.

These last properties are used to select the correct type of conductor and according to all of them different combination of materials are exploited. The most common conductors used are[16]: *Aluminum Stranded Conductor* (ASC), entirely made of pure aluminum and used for short span, *Aluminum Alloy Stranded Conductor* (AASC), made of aluminum alloy with a higher streinght-to-wieght ratio than the previous type, *Aluminum Alloy Conductor Steel Reinforced* (AACSR), it is the most common one and it has a steel based core to improve significantly the higher strength-to-weight ratio.

Nowadays a new typology of conductor is employed, the *Aluminum Conductor Composite Core* (ACCC); here the core is made of a composite material like glass fiber or carbon fiber. These materials are lighter and stronger than steel and have a much lower thermal expansion coefficient too: so there is a reduction of the force used to tension the conductor due to a lower weight and smaller dilatation due to thermal gradients. An other advantage is the increase of the fulfilled section of the outer layer with properly designed elementary wires. The final result is a

[15]M. Onore, *Smorzatore Stockbridge e soppressione delle vibrazioni dei cavi tesi: analisi numerica e sperimentale*, Polytechnic of Turin, 2018.

[16]Electric Research Power Institute EPRI, *Transmission Line Reference Book: Wind- Induced Conductor Motion*, Palo Alto, 2006.

considerable reduction of the electric power losses, by 25 % to 40 %[17][18][19][20].

Figure 1.7: Comparison between the ACSR (on the left) and ACCC (on the right)[21]

1.3 Stockbridge Damper

As evidenced by the previous section, the wind gives rise to conductor displacements. This behaviour must be controlled because it leads to a localized stress,

[17]Electric Research Power Institute EPRI, *Transmission Line Reference Book: Wind- Induced Conductor Motion*, Palo Alto, 2006.

[18]CTC Global Corporation, *Engineering Transmission Lines With High-Capacity, Low-Sag ACCC Conductor*, CTC Global, 2011.

[19]B. Wareing, *Types and Uses of High Temperature Conductor*, CIGRÉ (International Council on Large Electric Systems) Seminar. Bangkok: CIGRÉ Study Committee B2 Working group 11, 2011.

[20]J. Slegers, *Transmission Line Loading: Sag Calculations and High-Temperature Conductor Technologies*, Iowa State University, 2011.

[21]D. Bryant, *ACSR and ACCC,* 3 September 2013, in `https://bit.ly/3HRLzrs`.

[22]Electric Research Power Institute EPRI, *Transmission Line Reference Book: Wind- Induced Conductor Motion*, Palo Alto, 2006.

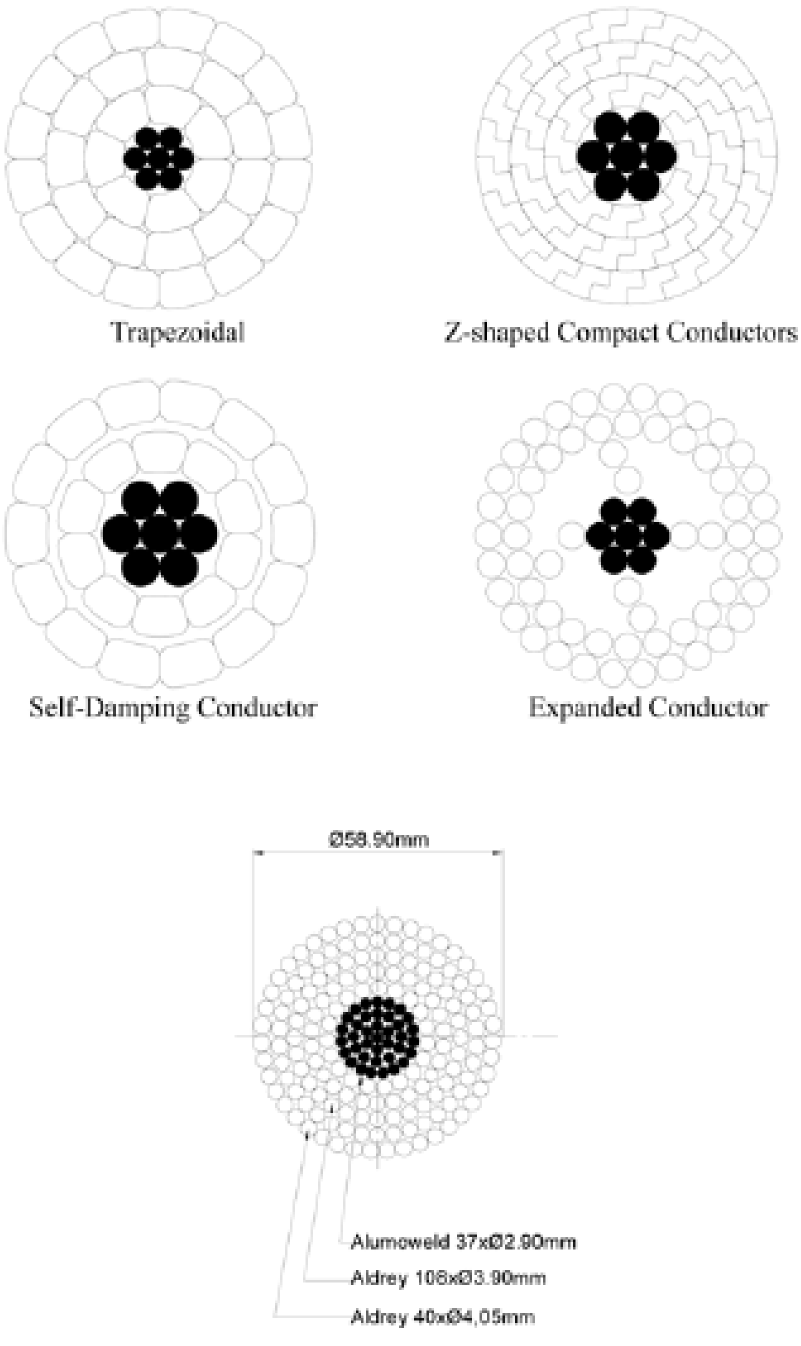

Figure 1.8: Cross-sections of different conductors[22]

called fretting fatigue; this trend causes surface cracks and their progressive growth because of the alternating motion of the strands that slip each other relatively. In order to control and prevent this stress, some dampers are mounted on the main conductor; in this way some of the energy transferred from the wind to the conductor is dissipated, effectively reducing the conductor oscillation amplitude. The most common used is the Stockbridge type and in the next section characteristics and mechanical properties are reported.

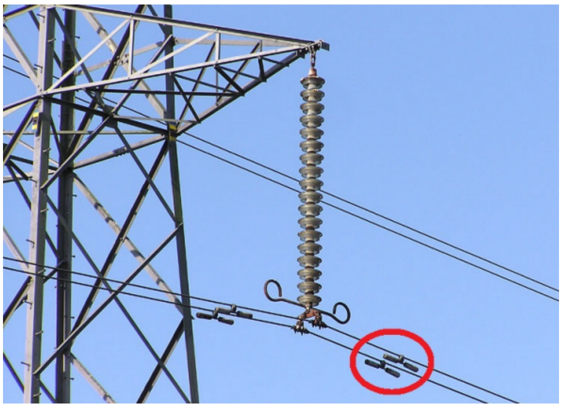

Figure 1.9: Stockbridge dampers mounted on the overhead lines[23]

1.3.1 Construction Characteristics

The Stockbridge damper was developed by George Stockbridge in 1925. It is an inertial damper and it is the most common type of damper used on overhead power lines[24][25].

The device consists of a messenger cable, made of a steel rope, at whose ends Zamak masses are cast, while in the central part the aluminum alloy clamp body is cast. This latter, together with the track cover, allows the mounting of the damper on the overhead line main conductor. The cast parts are realized with

[23] M. Buscemi, *Studio di un Sistema di Controllo Attivo per la Riduzione delle Vibrazioni nelle Linee Aeree di Trasmissione dell'Energia Elettrica*, MA thesis, Polytechnic of Milan, Italy, 1985.

[24] C.N. Canales et al., *Optimal Design of Stockbridge Dampers*, In: Ingenieria Mecanica Tecnologia y Desarollo 2, 2008, pp. 193–199.

[25] Electric Research Power Institute EPRI, *Transmission Line Reference Book: Wind- Induced Conductor Motion*, Palo Alto, 2006.

appropriate inertial characteristics as well as their relative distances and messenger cable dimensions (diameter, length, number of wires, etc.).

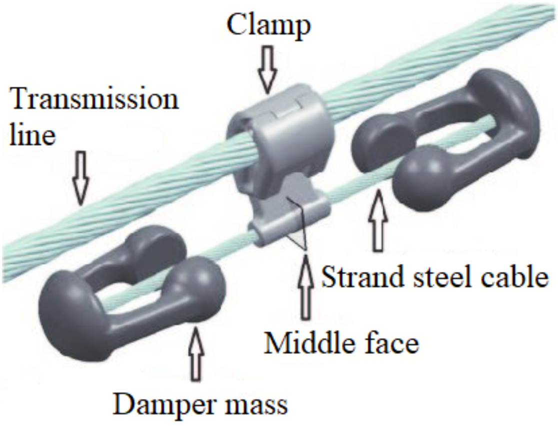

Figure 1.10: Stockbridge damper components[26]

The messenger cable arrangements on the clamp body, and that of the masses connected to it, is done in such a way as to make the geometry asymmetrical: the masses are different from each other and the distance between the junction mass-clamp body is different between the left side and the right side, making consequently different each moment of inertia[27].

1.3.2 Mechanical Properties

In this way it is possible to identify four resonance frequencies, to which correspond four mode shapes (see the Figure 1.12); moreover, the resonance frequencies of the device are distributed and it is possible to allow the vibrations attenuation induced by external forces in the whole range of frequencies at which they excite the conductor[28].

[26]Liang Wang Xiaoyu Luo and Yisheng Zhang, *Nonlinear numerical model with contact for Stockbridge vibration damper and experimental validation*, Journal of Vibration and Control, 2014.
[27]R. Claren and G. Diana, *Mathematical Analysis of Transmission Line Vibration*, In: IEEE Transactions on Power Apparatus and Systems 88, 1969, pp. 1741–1771.
[28]R. Claren and G. Diana, *Mathematical Analysis of Transmission Line Vibration*, In: IEEE Transactions on Power Apparatus and Systems 88, 1969, pp. 1741–1771.
[29]M. Onore, *Smorzatore Stockbridge e soppressione delle vibrazioni dei cavi tesi: analisi numerica e sperimentale*, Polytechnic of Turin, 2018.

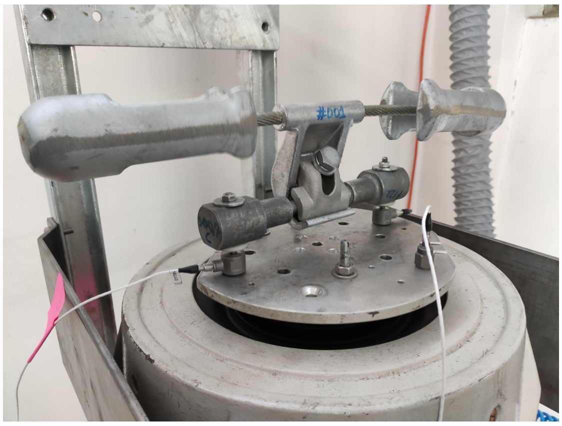

Figure 1.11: Stockbridge type damper used during experimental tests

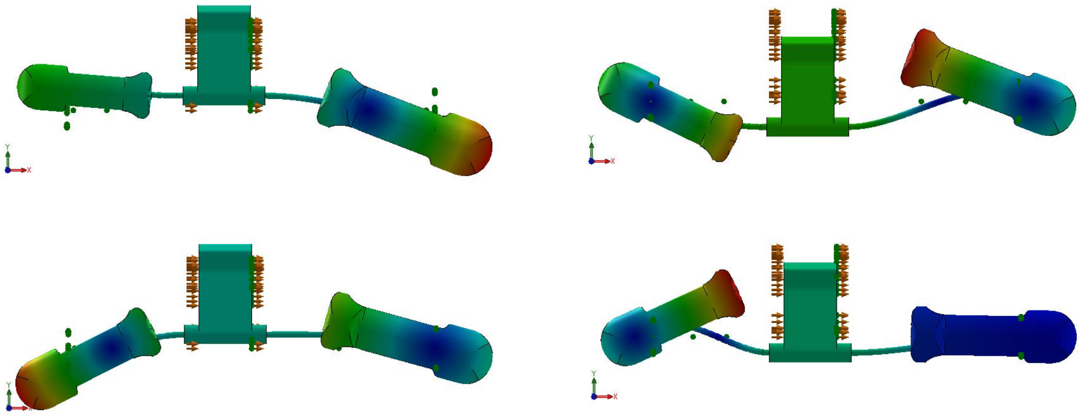

Figure 1.12: FEM mode shapes; at the top left is the 1° one, at the bottom left is the 2° one, at the top right is the 3° one, at the bottom right is the 4°. The colors gradient indicates the amplitude magnitude along the span, by blue the lowest up to red the highest.[29]

The messenger cable constitutes the damping element, whose mechanism depends on friction between the wires that make up the messenger cable. The friction in question is hysteretic; this behavior is characterized by a non-linear dynamic response: the damping and the dynamic stiffness of the messenger cable are functions of the body clamp vibration amplitude; consequently, also the resonance frequencies of the damper depend on it. In addition, the non-linearity of the system makes possible a self-regulation behavior of the damper[30][31][32].

During bending, conductor wires tend to flex according to the modal shape performed; this tendency is hindered by friction occurring between the contact surfaces of braided cables.

If the curvature value is small, the wires do not slide against each other, so this is the *full-stick* state, where all the wires move as one solid body[33]. EI_{max} represents the maximum theoretical cable bending stiffness as determined by averaging the bending stiffness of each braided wire[34].

$$EI_{max} = \sum(E_i \cdot I_i) \tag{1.2}$$

with E_i the i-th Young's modulus and I_i the i-th surface moment of inertia. In particular the surface moment of inertia is computed considering the neutral axis of the cable, so for each wire it is[35]:

$$I_i = I_{0i} + A_i \cdot d_i^2 \tag{1.3}$$

with I_{0i} the surface inertia moment related to the axis of the i-th wire, A_i the cross section of the i-th wire and d_i^2 the distance between the neutral axis of the cable and the neutral axis os the i-th wire.

When the curvature of the cable reaches the sufficient amplitude, the wires start to slip each other and this condition becomes more and more progressive with the curvature. This new situation that takes place is called *full-slip* state[36] and

[30]Electric Research Power Institute EPRI, *Transmission Line Reference Book: Wind- Induced Conductor Motion*, Palo Alto, 2006.

[31]F. Foti and L. Martinelli, *Hysteretic Behaviour of Stockbridge Dampers: Modelling and Parameter Identification*, In: Mathematical Problems in Engineering, 2018.

[32]C. Gazzola, *Modelling and assessment of aeolian vibrations of overhead transmission line conductors: theory and implementation*, PhD Thesis, Polytechnic of Milan, Italy, 2017.

[33]F. Foti and L. Martinelli, *Hysteretic Behaviour of Stockbridge Dampers: Modelling and Parameter Identification*, In: Mathematical Problems in Engineering, 2018.

[34]Electric Research Power Institute EPRI, *Transmission Line Reference Book: Wind- Induced Conductor Motion*, Palo Alto, 2006.

[35]Electric Research Power Institute EPRI, *Transmission Line Reference Book: Wind- Induced Conductor Motion*, Palo Alto, 2006.

[36]F. Foti and L. Martinelli, *Hysteretic Behaviour of Stockbridge Dampers: Modelling and Parameter Identification*, In: Mathematical Problems in Engineering, 2018.

the associated bending stiffness is EI_{min}; it is assumed to be the lowest theoretical possible value and it is computed considering the wires moving independently:

$$EI_{min} = \sum(E_i \cdot I_{0i}) \tag{1.4}$$

Nevertheless the (Equation 1.2) and (Equation 2.1) can give good estimation of these theoretical values, in literature it is possible to find other more complex expressions of EI_{max} and EI_{min} studied with a more precise mechanical model[37][38].

In particular, the model used in this study is the one developed by De Jong[39]; called κ the curvature, it results:

$$EI_{\kappa} = M = M_{\kappa} + \sum_{L=1}^{N} M_{d,L} \tag{1.5}$$

It is assumed that the external moment M is distributed over the cross section of the centered cable (M_K) and over the cross section of each single wire, shown with L, which becomes part of each layer around the core ($M_{d,L}$).

As a result, stiffness is composed of two parts, the primary one, which is constant and is determined by all the cables' cross sections, and the secondary one, which is determined by the amount of sliding and friction among the outer cables just discussed.

At the end, it can be proved as follows:

$$EI_{min} = \frac{E_k \pi \delta_k^4}{64} + \sum(n_L E_{d,L} \delta_{d,L}^4 \cos\beta_L) \tag{1.6}$$

$$EI_{max} = EI_{min} + \sum\left(\frac{n_L}{2} E_{d,L} A_{d,L} r_L^2 \cos^3\beta_L\right) \tag{1.7}$$

[37]F. Foti and L. Martinelli, *Mechanical Modeling of Metallic Strands Subjected to Tension, Torsion and Bending*, n: International Journal of Solids and Structures 91, 2016, pp. 1–17.

[38]A. Cardou, *Taut Helical Strength Bending Stiffness,* 2006, in `http://www.utfscience.deI/2006`.

[39]B.C. De Jong, *Analytical and experimental analysis of the capacity of steel wire ropes subjected to forced bending*, M.Sc Thesis submitted to the faculty of Civil Engineering and Geoscience, TU Delft, 2015.

[40]M. Onore, *Smorzatore Stockbridge e soppressione delle vibrazioni dei cavi tesi: analisi numerica e sperimentale*, Polytechnic of Turin, 2018.

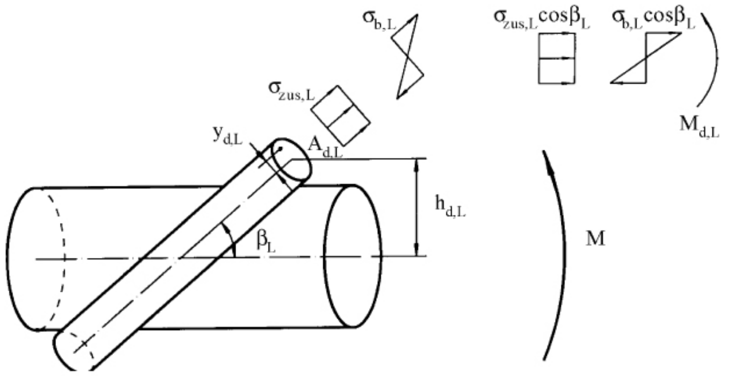

Figure 1.13: Bending stress applied to the core and the wires[40]

With $\delta_{d,L}$ the wires diameter, δ_k the diameter of the central core, E_k and $E_{d,L}$ the material Young's modulus and n_L the wires number per layer.

Generally, there is a smooth transition between the two bending stiffness and the most common value adopted oscillates by the 30 % up to the 50 % of EI_{max}; this value can be assumed independent of frequency and constant along the wire span[41].

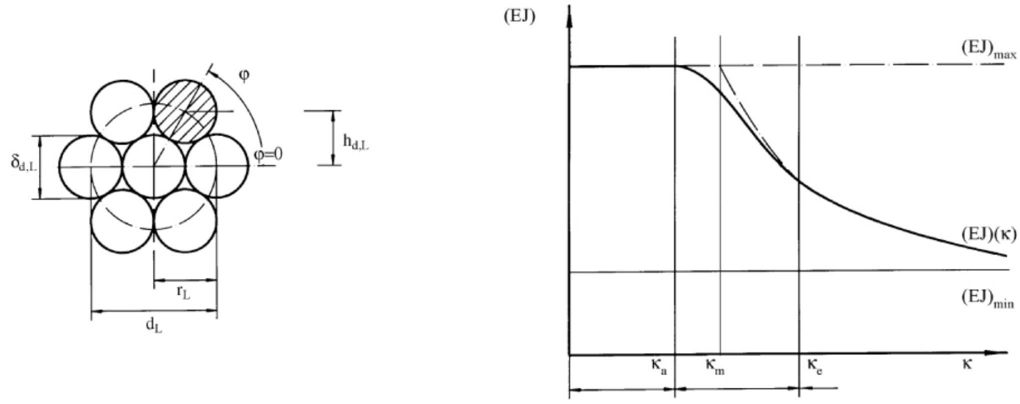

Figure 1.14: Diagram of curving-bending stiffness[42]

[41]CIGRE, *Modeling of Aeolian Vibrations of a Single Conductor Plus Damper - Assessment of Technology*, CIGRE WG B2.11 TF1. Electra Vol. 223, 2005.
[42]M. Onore, *Smorzatore Stockbridge e soppressione delle vibrazioni dei cavi tesi: analisi numerica e sperimentale*, Polytechnic of Turin, 2018.

As explained previously, when the cable is flexed, the braided wires tends to move slipping one another and this generates the friction between the contact surfaces. The self-damping induced by the cable strands is the reason why the system is damped and, therefore, energy is dissipated. This characteristic refers not only to the main conductors of the power lines, but to the messenger cable of the Stockbridge damper too, in fact it represents its damping element.

Differently from the messenger cable, the main conductor self-damping is connected to the tension to which it is subjected; in particular, if the tension increases, the wires does not slip, therefore the conductor self-damping decreases[43].

The Stockbridge damper has a particular characteristic: it behaves as a *tuned mass vibration adsorber*[44][45][46][47]: since it is possible to vary a priori the parameters of the device, such as the masses suspended at the ends of the cable, the mass of the body clamp and of the brace cover, the length and the section of the of the messenger cable, the moments of inertia of the masses, the distances between the barycenter and the suspended mass-clamp body junction, the stiffness and hysteresis factor of the messenger cable, it becomes possible to design the impedance of the damper to coincide with that of the main conductor[48]; the two parts of the messenger cable behave like cantilevered beams with concentrated masses positioned at the ends. In this way, the energy that the wind imprints on it is mostly dissipated by the Stockbridge damper.

If the wind excites the conductor near one of its resonant frequencies and the damping is low, small displacements of the clamp body of the Stockbridge damper may correspond to a large amplitude of oscillations of the main conductor. Then the damper clamp body amplitude increases too, shifting the resonant frequency

[43]CIGRE, *Modeling of Aeolian Vibrations of a Single Conductor Plus Damper - Assessment of Technology*, CIGRE WG B2.11 TF1. Electra Vol. 223, 2005.

[44]P. Hagedorn, *Wind-Excited Vibrations of Transmission Lines: A Comparison of Different Mathematical Models*, In: Mathematical Modelling 8, 1987, pp. 352–358.

[45]M. Buscemi, *Studio di un Sistema di Controllo Attivo per la Riduzione delle Vibrazioni nelle Linee Aeree di Trasmissione dell'Energia Elettrica*, MA thesis, Polytechnic of Milan, Italy, 1985.

[46]**langlois**.

[47]H. Kasap, *Investigation of Stockbridge Dampers for Vibration Control of Overhead Transmission Lines*, MSc Thesis, Middle East Technical University, Turkey, 2012.

[48]R. Claren and G. Diana, *Mathematical Analysis of Transmission Line Vibration*, In: IEEE Transactions on Power Apparatus and Systems 88, 1969, pp. 1741–1771.

away, acting like a dynamic absorber; this trend continues until the maximum amplitude of the modal shape is reached.

The impedance of the damper is calibrated in such a way that when inserted (at a node) into the FEM model of the conductor (hinge-hinge or bogie-bogie ends), it generates the energy dissipation that keeps the conductor deformation within the limits set at each node of the model.

The selection of the node in which to model the impedance has a fundamental role too: to define the installation distance from the conductor ends, models known in literature are used (on dedicated software) that are consolidated by many years of experience and by numerous test campaigns.

2. Analytical model

2.1 Six-degrees of Freedom Model

To make the mathematical model more reliable, several assumptions are adopted.

First, it is assumed that the messenger cable has two distinct values of flexural stiffness: given a certain frequency, the movement of the right side is different from the left, which results in different friction between the contact surfaces of the strands. This causes two distinct values of stiffness.

It is assumed that the clamp body is rigidly attached to the conductor, and that its movement is vertical; under this assumption, there is no rotation of the clamp body.

At last, as a result of the friction generated by the strands of the messenger cable, the physical model is of hysteretic type as it is more accurate than a viscous one. Again, as with flexural stiffness, two different hysteresis coefficients will be assumed, one on each side of the messenger cable, due to the different physics governing the two sides of the cable.

Among the models collected in the literature, the one used to describe the Stockbridge dynamics is with six degrees of freedom with concentrated parameters[1]. In particular, these correspond to the angular and vertical displacements of the cantilevered masses and the body clamp one.

At this point, the degree of freedom vector, $\underline{x}$, is defined as:

$$\underline{x} = \{x_1 \quad \varphi_1 \quad x_c \quad \varphi_c \quad x_2 \quad \varphi_2\}^T \tag{2.1}$$

By studying the free body diagram of the damper, the following system of differential equations can be constructed:

[1] R. Claren and G. Diana, *Mathematical Analysis of Transmission Line Vibration*, In: IEEE Transactions on Power Apparatus and Systems 88, 1969, pp. 1741–1771.

[2] M. Onore, *Smorzatore Stockbridge e soppressione delle vibrazioni dei cavi tesi: analisi numerica e sperimentale*, Polytechnic of Turin, 2018.

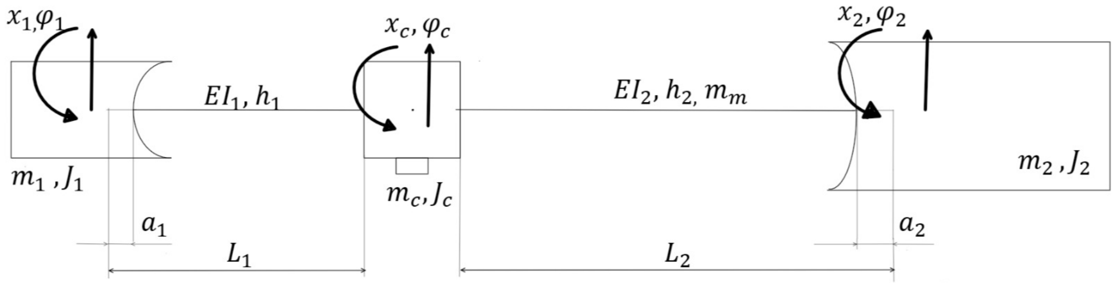

Figure 2.1: Six degrees of freedom adopted[2]

$$[M]\underline{\ddot{x}} + [R]\underline{\dot{x}} + [K]\underline{x} = \underline{F} \tag{2.2}$$

Where $[M]$ is the mass matrix, $[R]$ is the damping matrix, $[K]$ is the stiffness matrix and F is the vector of the external applying stresses.

$$\underline{F} = \{0 \quad 0 \quad F \quad M \quad 0 \quad 0\}^T \tag{2.3}$$

These equations are the base of the FEM analysis. All the parameters used on its development are listed below:

1. The stiffness and hysteresis factor of both sides of messenger cable, respectively indicated with EI_i and h_i;
2. The right and left side lengths of the messenger cable, indicated with L_i;
3. the distances between the barycenter and the suspended mass-clamp body junction, indicated with a_i;
4. The masses and the mass moment of inertia, indicated respectively with m_i and J_i;
5. As for the frequency, this will be converted into the corresponding ω_i pulse;

2.1.1 Mass Matrix $[M]$

This mass matrix is made up of two components: the first, a sub-matrix related to the cantilever-mounted masses and the clamp mass, defined as $[M_{mass}]$ and the second relating to the messenger cable mass, combining both the left and right sides' contributions, defined as $[M_{mm}]$.

$$[M] = [M_{mm}] + [M_{mass}] \tag{2.4}$$

$[M_{mm}]$ **Mass Matrix**

The term M_{mm} is computed exploiting the *Eulero-Bernoulli free-beam* literature. In general, the mass matrix is determined by considering the axial and flexural loads on a beam element of length L, as shown in Figure 2.2 and Figure 2.3.

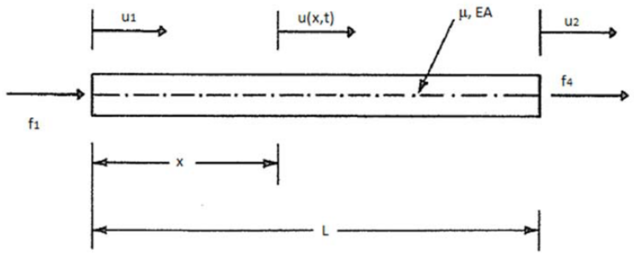

Figure 2.2: Beam element under axial load[3]

Using the shape functions $L(x)$[5], the mass matrix is calculated. So there is:

$$[M] = \int_0^L \mu(x)\{L(x)\}\{L(x)\}^T dx \tag{2.5}$$

The following shape functions are valid for axial strain:

$$L_{ass}(x) = \begin{cases} L_1(x) \\ L_2(x) \end{cases} = \begin{cases} 1 - \frac{x}{L} \\ \frac{x}{L} \end{cases} \tag{2.6}$$

In Equation 2.5, considering linear density μ of the beam constant, we obtain:

[3]M. Onore, *Smorzatore Stockbridge e soppressione delle vibrazioni dei cavi tesi: analisi numerica e sperimentale*, Polytechnic of Turin, 2018.

[4]M. Onore, *Smorzatore Stockbridge e soppressione delle vibrazioni dei cavi tesi: analisi numerica e sperimentale*, Polytechnic of Turin, 2018.

[5]L. Meirovitch, *Elements on vibration analysis*, College of Engineering, Virginia Polytechnic Institute and State University, 1986.

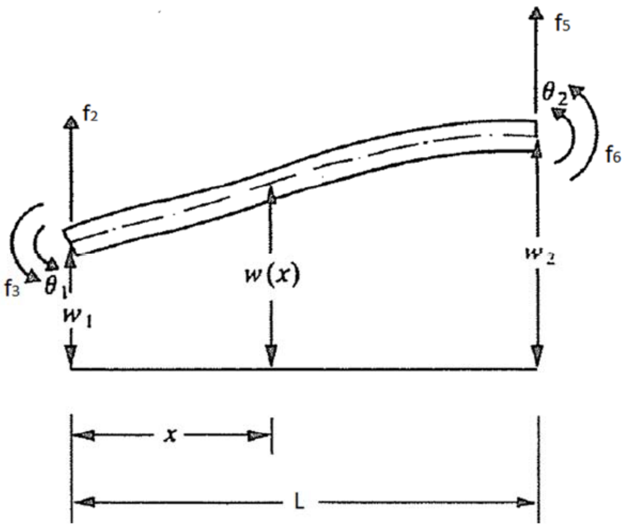

Figure 2.3: Beam element under bending load[4]

$$[m_{axial}] = \mu \int_0^L \begin{bmatrix} (1-\frac{x}{L})^2 & (1-\frac{x}{L})\frac{x}{L} \\ (1-\frac{x}{L})\frac{x}{L} & (\frac{x}{L})^2 \end{bmatrix} dx = \frac{\mu L}{6} \begin{bmatrix} 2 & 1 \\ 1 & 2 \end{bmatrix} \tag{2.7}$$

Applying the same principles to the element which is under bending load, taking into account that:

$$L_{bend}(x) = \begin{cases} L_1(x) \\ L_2(x) \\ L_3(x) \\ L_4(x) \end{cases} = \begin{cases} 1 - 3(\frac{x}{L})^2 + (\frac{x}{L})^2 \\ (\frac{x}{L}) - 2(\frac{x}{L})^2 + 3(\frac{x}{L})^3 \\ 3(\frac{x}{L})^2 - (\frac{x}{L})^3 \\ -(\frac{x}{L})^2 + (\frac{x}{L})^3 \end{cases} \tag{2.8}$$

By integrating, we determine:

$$[m_{bend}] = \frac{\mu L}{420} \begin{bmatrix} 156 & 22L & 54 & -13L \\ 22L & 4L^2 & 13L & -3L^2 \\ 54 & 13L & 156 & 22L \\ -13L & -3L^2 & -22L & 4L^2 \end{bmatrix} \tag{2.9}$$

According to these results, the complete mass matrix for the 6 degrees of freedom looks like this:

$$[M] = \frac{\mu L_i}{420}\begin{bmatrix} 140 & 0 & 0 & 70 & 0 & 0 \\ 0 & 156 & 22L_i & 0 & 54 & -13L_i \\ 0 & 22L_i & 4{L_i}^2 & 0 & 13L_i & -3{L_i}^2 \\ 70 & 0 & 0 & 140 & 0 & 0 \\ 0 & 54 & 13L_i & 0 & 156 & -22L_i \\ 0 & -13L_i & -3{L_i}^2 & 0 & -22L_i & 4{L_i}^2 \end{bmatrix} \tag{2.10}$$

Taking into account the case that is under consideration, as there is no degree of freedom along the direction of the beam (u_1 and u_4 of Figure 2.3), the mass matrix of the left and right halves of the damper messenger cable will be exclusively composed of the smaller 4×4 of degrees of freedom of rotation and translation of the body. So there will be:

$$[M_{mmi}] = \frac{\mu L}{420}\begin{bmatrix} 156 & 22L_i & 54 & -13L_i \\ 22L & 4{L_i}^2 & 13L & -3{L_i}^2 \\ 54 & 13L_i & 156 & 22L_i \\ -13L & -3{L_i}^2 & -22 & 4{L_i}^2 \end{bmatrix} \tag{2.11}$$

The total matrix of the messenger cable can be obtained by superimposing left and right sides, both having different lengths, but having in common degrees of freedom corresponding to the clamp.

$[M_{mass}]$ Mass Matrix

Taking into account the two masses at the end of the messenger cable and the clamp, the M_{mass} represents the mass contribution. Furthermore, as already stated, the barycentre of a mass is considered distant a_i from the conjunction of the mass with the messenger cable. So, there will be:

$$[M_{mass}] = \begin{bmatrix} m_1 & m_1a_1 & 0 & 0 & 0 & 0 \\ m_1a_1 & J_1 + m_1{a_1}^2 & 0 & 0 & 0 & 0 \\ 0 & 0 & m_c & 0 & 0 & 0 \\ 0 & 0 & 0 & J_c & 0 & 0 \\ 0 & 0 & 0 & 0 & m_2 & m_2a_2 \\ 0 & 0 & 0 & 0 & m_2a_2 & J_2 + m_2{a_2}^2 \end{bmatrix} \tag{2.12}$$

2.1.2 Stiffness Matrix $[K]$

The definition of the stiffness matrix considers the displacements of the cable ends. So in the free body diagram of the beam element L are shown in Figure 2.4 and fig:30.

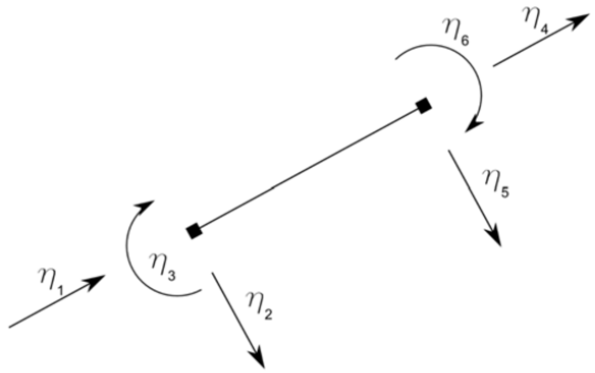

Figure 2.4: Degrees of freedom of the ends of a beam element[6]

The stiffness matrix is constructed again using shape functions, however, for axial loads we will use its first derivative (Equation 2.13), and for bending loads we will use its second derivative (eq:17).

[6]M. Onore, *Smorzatore Stockbridge e soppressione delle vibrazioni dei cavi tesi: analisi numerica e sperimentale*, Polytechnic of Turin, 2018.

[7]M. Onore, *Smorzatore Stockbridge e soppressione delle vibrazioni dei cavi tesi: analisi numerica e sperimentale*, Polytechnic of Turin, 2018.

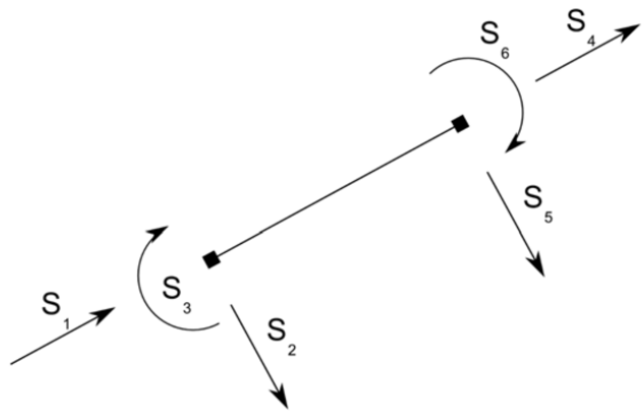

Figure 2.5: Stresses applied to the ends of the beam element[7]

$$\{L'(x)\} = \frac{d}{dx}\{L(x)\} \tag{2.13}$$

$$\{L''(x)\} = \frac{d^2}{dx^2}\{L(x)\} \tag{2.14}$$

The stiffness matrix related to axial load is Equation 2.15, while that related to bending load is Equation 2.16.

$$[K] = \int_0^L EA(x)\{L'(x)\}\{L'(x)\}^T dx \tag{2.15}$$

$$[K] = \int_0^L EI(x)\{L''(x)\}\{L''(x)\}^T dx \tag{2.16}$$

So the shape functions for the axial load will be:

$$L'_{ass}(x) = \begin{cases} L'_1(x) \\ L'_2(x) \end{cases} = \begin{cases} \frac{d}{dx}(1 - \frac{x}{L}) \\ \frac{d}{dx}(\frac{x}{L}) \end{cases} = \begin{cases} -1 \\ 1 \end{cases} \tag{2.17}$$

Hence, including Equation 2.17 in Equation 2.15, the following expression is obtained:

$$[k_{axial}] = \frac{EA}{L^2}\int_0^L \begin{Bmatrix} -1 \\ 1 \end{Bmatrix}\begin{Bmatrix} -1 \\ 1 \end{Bmatrix}^T dx = \frac{EA}{L}\begin{bmatrix} 1 & -1 \\ -1 & 1 \end{bmatrix} \tag{2.18}$$

The same procedure is adopted for the bending load case. Considering that:

$$L''_{bend}(x) = \begin{cases} L''_1(x) \\ L''_2(x) \\ L''_3(x) \\ L''_4(x) \end{cases} = \frac{2}{L^2} \begin{cases} -3 + 6(\frac{x}{L}) \\ -2 + 3(\frac{x}{L}) \\ 3 - 6(\frac{x}{L}) \\ -1 + 3(\frac{x}{L}) \end{cases} \tag{2.19}$$

Including Equation 2.19 into Equation 2.16, the stiffness matrix obtained is:

$$[k_{bend}] = \frac{EI}{L^3} \begin{bmatrix} 12 & 6L & -12 & 6L \\ 6L & 4L^2 & -6L & 2L^2 \\ -12 & -6L & 12 & -6L \\ 6L & 2L^2 & -6L & 4L^2 \end{bmatrix} \tag{2.20}$$

As a result of these results, the complete stiffness matrix corresponds to the following:

$$[K] = \begin{bmatrix} \frac{EA}{L} & 0 & 0 & -\frac{EA}{L} & 0 & 0 \\ 0 & \frac{12EI}{L^3} & \frac{6EI}{L^2} & 0 & -\frac{12EI}{L^3} & \frac{6EI}{L^2} \\ 0 & \frac{6EI}{L^2} & \frac{4EI}{L} & 0 & -\frac{6EI}{L^2} & \frac{2EI}{L} \\ -\frac{EA}{L} & 0 & 0 & \frac{EA}{L} & 0 & 0 \\ 0 & -\frac{12EI}{L^3} & -\frac{6EI}{L^2} & 0 & \frac{12EI}{L^3} & -\frac{6EI}{L^2} \\ 0 & \frac{6EI}{L^2} & \frac{2EI}{L} & 0 & -\frac{6EI}{L^2} & \frac{4EI}{L} \end{bmatrix} \tag{2.21}$$

As in the case of the mass matrix, contributions associated with degrees of freedom along the direction of the beam axis are ignored (η_1 and η_4 of Figure 2.4) and the stiffness matrix, related to each side of the messenger cable, will consider a 4×4 matrix system. At the end the result is:

$$[K_i] = \frac{EI_i}{L^3} \begin{bmatrix} 12 & 6L_i & -12 & 6L_i \\ 6L_i & 4{L_i}^2 & -6L_i & 2{L_i}^2 \\ -12 & -6L_i & 12 & -6L_i \\ 6L_i & 2{L_i}^2 & -6L_i & 4{L_i}^2 \end{bmatrix} \tag{2.22}$$

The total stiffness matrix considers the two messenger cable sides contributions together.

2.1.3 Damping Matrix $[R]$

It should be noted that in some cases, the hysteretic damping model is closer to reality than the viscous model[8]. The Equation 2.23 represents the adopted model:

$$[M]\{\ddot{x}\} + [\tilde{K}]\{x\} = \{F_0\}e^{i\Omega t} \tag{2.23}$$

Furthermore, it can be demonstrated that the damping matrix R comes from the stiffness matrix K: the stiffness of a structure, which has hysteretic damping, can be expressed in the form of a complex stiffness; therefore it is:

$$[\tilde{K}] = [K] + i[R] \tag{2.24}$$

Where the real part correspond to the stiffness matrix $[K]$, studied in the previous section, and the imaginary part correspond to the damping matrix $[R]$, which indicates the energy dissipation capability of the system.

This matrix is proportional to the frequency and to the damping coefficient; in particular, in this case, considering the asymmetrical geometry of the Stockbridge damper messenger cable, there are two damping coefficients considered, h_1 and h_2[9]. There are two sub-matrices which describe the damping behavior of each part of the messenger cable:

$$[R_{1,2}] = \frac{h_{1,2}}{\Omega}[K_{1,2}] \tag{2.25}$$

Like what has already been said for the mass and stiffness matrix, the damping matrix is obtained by superimposing the single damping matrices of the left and right sides of the Stockbridge damper.

2.1.4 Impedance Matrix $[H]$ and Mathematical Models

At this point, knowing the 6×6 mass, stiffness and damping matrices, it possible to proceed with the resolution of the linear system.

[8] S. Marchesiello A. Fasana, *Meccanica delle Vibrazioni*, CLUT, Politecnico di Torino, 2006.

[9] N. Amati G. Genta, *On the equivalent viscous damping for systems with hysteresis*, Trabalho de Conclusão de Curso, Universidade Tecnológica Federal do Paraná, Curitiba, 2018.

The *assembling method*[10] is used to this purpose; it consists in the exchange of the rows of the matrices according to the contributions of the every freedom degree as read in the free body diagram. There will be a 4×4 sub-system that refers to the cantilever masses movements contributions, x_L vector, and a 2×2 sub-system that refers to the body clamp movements contributions ones, x_V vector.

By the way, the input quantities are the vertical displacement and rotation of the body clamp, which are assumed to be harmonics:

$$\begin{bmatrix} x_c \\ \varphi_c \end{bmatrix} = \begin{bmatrix} x_{c0} \\ \varphi_{c0} \end{bmatrix} e^{i\Omega t} \tag{2.26}$$

So there is a sub-vector for the body clamp movements:

$$\underline{x_V} = \{x_c \quad \varphi_c\}^T \tag{2.27}$$

While the cantilever masses coordinates are contained in the following sub-vector:

$$\underline{x_L} = \{x_1 \quad \varphi_1 \quad x_2 \quad \varphi_2\}^T \tag{2.28}$$

So, it results:

$$\underline{x} = \left\{ \begin{matrix} \underline{x_L} \\ \underline{x_V} \end{matrix} \right\} \tag{2.29}$$

With the same idea, the mass matrix, the stiffness matrix and the damping matrix are arranged in the following ways:

$$[M] = \begin{bmatrix} \begin{bmatrix} & M_{LL} & \\ & & \end{bmatrix} & \begin{bmatrix} M_{LV} \\ \end{bmatrix} \\ \begin{bmatrix} & M_{VL} & \end{bmatrix} & \begin{bmatrix} M_{VV} \end{bmatrix} \end{bmatrix} \tag{2.30}$$

[10] L. Meirovitch, *Elements on vibration analysis*, College of Engineering, Virginia Polytechnic Institute and State University, 1986.

$$[K] = \begin{bmatrix} \begin{bmatrix} & K_{LL} & \\ & & \end{bmatrix} & \begin{bmatrix} K_{LV} \\ \end{bmatrix} \\ \begin{bmatrix} & K_{VL} & \end{bmatrix} & \begin{bmatrix} K_{VV} \end{bmatrix} \end{bmatrix} \tag{2.31}$$

$$[R] = \begin{bmatrix} \begin{bmatrix} & R_{LL} & \\ & & \end{bmatrix} & \begin{bmatrix} R_{LV} \\ \end{bmatrix} \\ \begin{bmatrix} & R_{VL} & \end{bmatrix} & \begin{bmatrix} R_{VV} \end{bmatrix} \end{bmatrix} \tag{2.32}$$

As will be evident from the following equation, considering the Equation 2.2, the matrices can be reordered as follows:

$$\begin{cases} [M_{LL}]\underline{\ddot{x_L}} + [R_{LL}]\underline{\dot{x_L}} + [K_{LL}]\underline{x_L} = -[M_{LV}]\underline{\ddot{x_V}} - [R_{LV}]\underline{\dot{x_V}} - [K_{LV}]\underline{x_V} \\ [M_{VL}]\underline{\ddot{x_L}} + [R_{VL}]\underline{\dot{x_L}} + [K_{VL}]\underline{x_L} = F_V - [M_{VV}]\underline{\ddot{x_V}} - [R_{VV}]\underline{\dot{x_V}} - [K_{VV}]\underline{x_V} \end{cases} \tag{2.33}$$

The displacements and rotations of the two masses are obtained from the first formula; as a result, the resolution of the system gives the force and the moment at the clamp body.

Now, the following matrices are derived, which are constants in time but vary in frequency:

$$\begin{cases} [A] = -\Omega^2[M_{LL}] + i\Omega[R_{LL}] + [K_{LL}] \\ [B] = -(-\Omega^2[M_{LV}] + i\Omega[R_{LV}] + [K_{LV}]) \\ [C] = -\Omega^2[M_{VL}] + i\Omega[R_{VL}] + [K_{VL}] \\ [D] = -(-\Omega^2[M_{VV}] + i\Omega[R_{VV}] + [K_{VV}]) \end{cases} \tag{2.34}$$

The equations of the system are rewritten in a compact manner, obtaining:

$$\begin{cases} [A]\underline{x_{L0}} = [B]\underline{x_{v0}} \\ [C]\underline{x_{L0}} = \underline{F_{V0}} + [D]\underline{x_{V0}} \end{cases} \tag{2.35}$$

$$\underline{x_{L0}} = [A]^{-1}[B]\underline{x_{V0}} \tag{2.36}$$

$$\underline{F_{V0}} = ([C][A]^{-1}[B] - [D])\underline{x_{V0}} = [H(i\Omega)]\underline{x_{V0}} \tag{2.37}$$

In this way a 2×2 complex matrix is obtained: $[H]$ represents the *Impedance Matrix* and it is so defined:

$$[H(i\Omega)] = \begin{bmatrix} f_{uu} & f_{u\varphi} \\ f_{\varphi u} & f_{\varphi\varphi} \end{bmatrix} \tag{2.38}$$

Basically, it represents the connection between input, which is displacement and rotation of the cable terminal or conductor, being these rigidly connected, and output, which is force and moment transmitted from the cable terminal to the cable.

Particularly, the proportionality factor between displacement and force, f_{uu}, is of interest since during laboratory testing the clamp's rotation is assumed to be zero. Therefore, the analytical model proposed can simulate the Stockbridge damper operating curve as determined in the laboratory.

In principle, the modulus and phase of the FRF can be derived from the complex expression f_{uu}:

$$G(\Omega) = |H_{1,1}| = \sqrt{(\Re(f_{uu}))^2 + (\Im(f_{uu}))^2} \tag{2.39}$$

$$\varphi(\Omega) = \angle H_{1,1} = \arctan\left[\frac{\Im(f_{uu})}{\Re(f_{uu})}\right] \tag{2.40}$$

This will give real values, making it possible to compare experimental and theoretical values.

In the presence of Equation 2.39 and Equation 2.40, a numerical model can be developed to estimate the energy and the power dissipated at each cycle.

From the literature, the power can be computed by the inner product between the force and the velocity:

$$[\underline{P}] \doteq \{\underline{F}\}^T \cdot \{\underline{\dot{x}}\} \tag{2.41}$$

With the the force F and the velocity $\dot{x}$ defined as:

$$\{\underline{F}\} = \{\underline{F_0}\}e^{i\Omega t} \tag{2.42}$$

$$\{\underline{\dot{x}}\} = i\Omega\{\underline{x_0}\}e^{i\Omega t} \tag{2.43}$$

Defining the conjugate of $\{\underline{F}\}$:

$$\{\underline{F}\} = \{\underline{F_0^*}\}e^{-i\Omega t} \tag{2.44}$$

The power can be written as:

$$[\underline{P}] = i\Omega\{\underline{F_0}^*\}^T\{\underline{x_0}\} \tag{2.45}$$

Noting that:

$$\{\underline{F}\} = \begin{Bmatrix} \{\underline{F_L}\} \\ \{\underline{F_V}\} \end{Bmatrix} = \begin{Bmatrix} \{\underline{0}\} \\ \{\underline{F_{V0}}\} \end{Bmatrix} e^{i\Omega t} \tag{2.46}$$

$$\{\underline{x}\} = \begin{Bmatrix} \{\underline{x_L}\} \\ \{\underline{x_V}\} \end{Bmatrix} = \begin{Bmatrix} \{\underline{x_{L0}}\} \\ \{\underline{x_{V0}}\} \end{Bmatrix} e^{i\Omega t} \tag{2.47}$$

It follows:

$$[\underline{P}] = i\Omega \left\{ \{\underline{0}\}^T \quad \{\underline{F_{V0}}\}^T \right\} \begin{Bmatrix} \{\underline{x_{L0}}\} \\ \{\underline{x_{V0}}\} \end{Bmatrix} = i\Omega\{\underline{F_{V0}}^*\}^T\{\underline{x_{V0}}\} \tag{2.48}$$

From the Equation 2.37, knowing that:

$$\{\underline{F_{V0}}^*\}^T = \{\underline{x_{V0}}^*\}^T[H^*]^T \tag{2.49}$$

Then there is:

$$[\underline{P}] = i\Omega\{\underline{x_{V0}}^*\}^T[H^*]^T\{\underline{x_{V0}}\} \tag{2.50}$$

Hence at the end the power is:

$$\underline{P} = i\Omega \left\{ \underline{x_{C0}}^* \quad \underline{0} \right\} \begin{bmatrix} f_{uu}{}^* & f_{u\varphi}{}^* \\ f_{\varphi u}{}^* & f_{\varphi\varphi}{}^* \end{bmatrix} \begin{Bmatrix} \underline{x_{C0}} \\ \underline{0} \end{Bmatrix} \tag{2.51}$$

The result of the computations is:

$$\underline{P} = i\Omega\{\underline{x_{C0}}\}^2 f_{uu}{}^* \tag{2.52}$$

Remembering the expression of the impedance:

$$f_{uu}(\Omega) = G(\Omega)e^{i\varphi(\Omega)} \tag{2.53}$$

$$f_{uu}{}^*(\Omega) = G(\Omega)e^{-i\varphi(\Omega)} \tag{2.54}$$

Substituting the Equation 2.54 in the Equation 2.52, the power becomes:

$$\underline{P} = i\Omega\{\underline{x_{C0}}\}^2 G(\Omega)e^{-i\varphi(\Omega)} = \Omega\{\underline{x_{C0}}\}^2 G(\Omega)e^{i[\frac{\pi}{2}-\varphi(\Omega)]} \tag{2.55}$$

Using the goniometric functions it is possible to rewrite the power in the following way:

$$\underline{P} = \Omega\{\underline{x_{C0}}\}^2 G(\Omega)[\cos(-\varphi) + i\sin(-\varphi)] = \Omega\{\underline{x_{C0}}\}^2 G(\Omega)[\sin(\varphi) + i\cos(\varphi)] \tag{2.56}$$

So it is possible to consider a real power and an imaginary power; at the end the equations that can be used to perform the power FEM analysis are:

$$\Re(\underline{P}) = \Omega\{\underline{x_{C0}}\}^2 G(\Omega)\sin\varphi \tag{2.57}$$

$$\Im(\underline{P}) = \Omega\{\underline{x_{C0}}\}^2 G(\Omega)\cos\varphi \tag{2.58}$$

$$\underline{P} = \sqrt{\Re(\underline{P})^2 + \Im(\underline{P})^2} \tag{2.59}$$

Regarding the energy, it is:

$$\underline{E_C} = \int_0^T \underline{P}dt = \underline{P}T = \underline{P}\left(\frac{2\pi}{\Omega}\right) = 2\pi\{\underline{x_{C0}}\}^2 G(\Omega)[\sin(\varphi) + i\cos(\varphi)] \tag{2.60}$$

Considering the real and imaginary parts, the equations used to perform the

FEM analysis are:

$$\Re(\underline{E_C}) = 2\pi\{\underline{x_{C0}}\}^2 G(\Omega)\sin\varphi \tag{2.61}$$

$$\Im(\underline{E_C}) = 2\pi\{\underline{x_{C0}}\}^2 G(\Omega)\cos\varphi \tag{2.62}$$

$$\underline{E_C} = \sqrt{\Re(\underline{E_C})^2 + \Im(\underline{E_C})^2} \tag{2.63}$$

2.2 Sensitive Analyses

The mathematical models derived above are used for numerical simulations. The behavior of the energy, modulus, and phase characteristics in relation to the influence of the parameters involved in the damper dynamics was observed to make a good fitting with the experimental data.

In addition to the geometrical parameters, which have been measured and checked by CAD software, a study is conducted to investigate which has a greater impact on the dynamics of the Stockbridge damper.

The results will be commented in the following chapters.

2.2.1 EI_1 stiffness variation

In this section the plots for the variation of the stiffness EI_1 are shown. This corresponds to the shorter part of the messenger cable. It can be seen that the most sensitive variation in the curves is in the $15-25Hz$ and $60-120Hz$ frequency ranges, where there are the second and the fourth mode shapes respectively. Moreover, from Figure 2.9 there is a divergence of values between FEM curves and experimental data, due to an attenuation of the latter. This problem results due to the experimental errors recorded during the measurements: the machine always provides the same amount of power, and consequently of energy, as the inertia of the machine itself acts as a filter preventing the transfer of energy to the damper. Also for the other sensitive analysis, in the same frequency range the same behavior can be noticed, however the trend of the FEM curves remains correct.

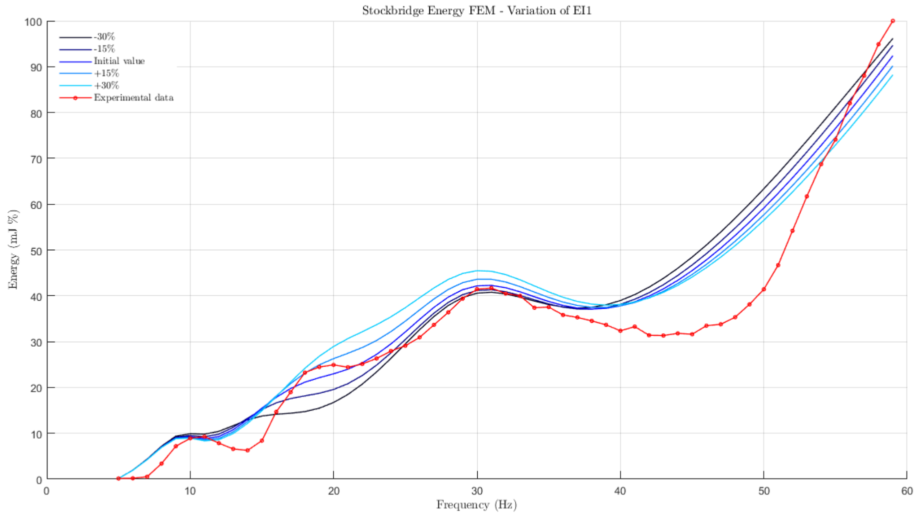

Figure 2.6: Energy curves as a function of EI_1, 5-59 Hz

2.2.2 EI_2 stiffness variation

In this section the plots for the variation of the stiffness EI_2 are shown. On the contrary, this correspond to the one related to the longer part of the messenger cable. Here the most sensitive variation of the numerical results is in the $5 - 15Hz$ and in the $25 - 45Hz$ frequency ranges, where there are the first and the third mode shapes respectively.

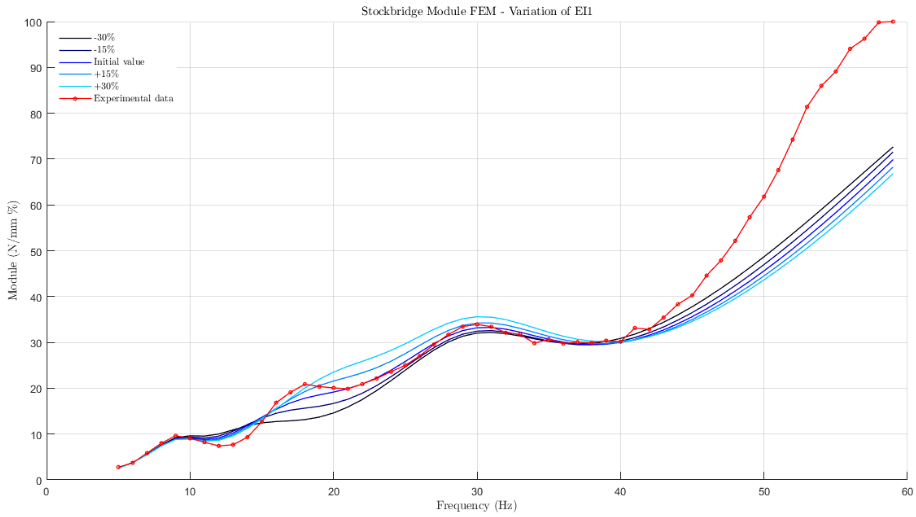

Figure 2.7: Modulus curves as a function of EI_1, 5-59 Hz

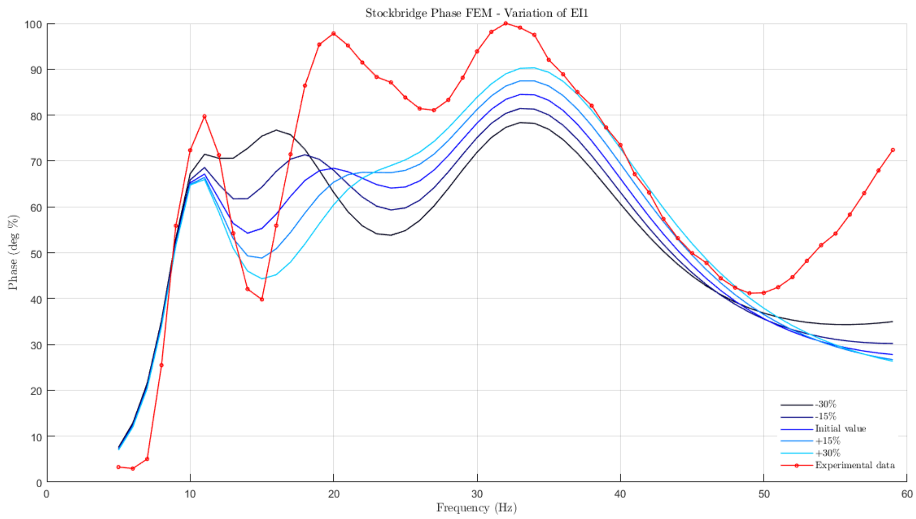

Figure 2.8: Phase curves as a function of EI_1, 5-59 Hz

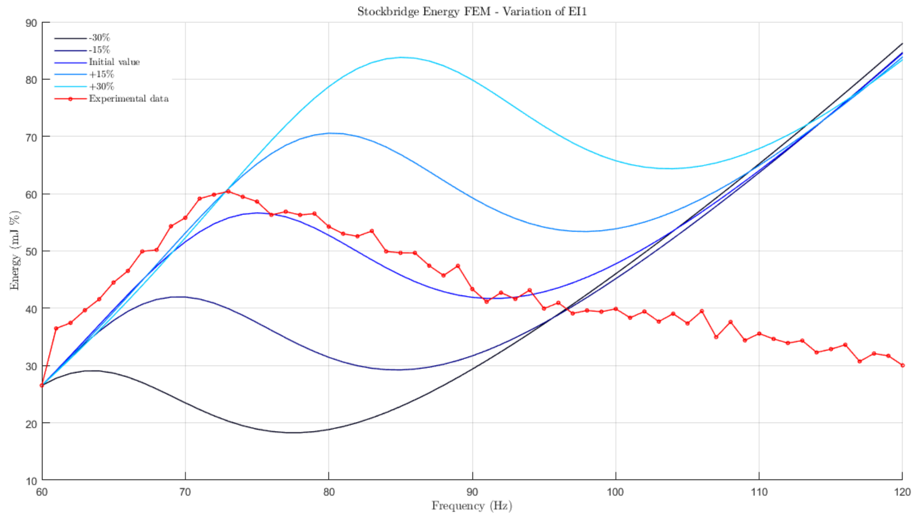

Figure 2.9: Energy curves as a function of EI_1, 60-120 Hz

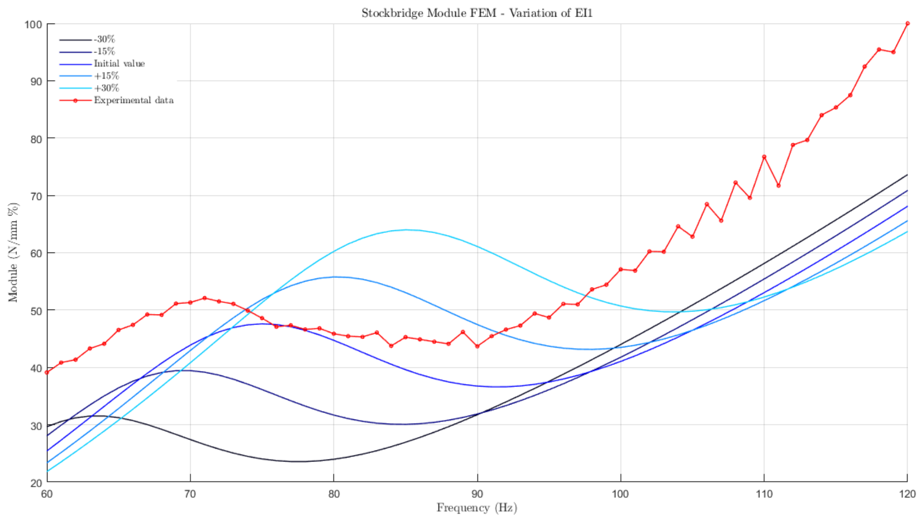

Figure 2.10: Modulus curves as a function of EI_1, 60-120 Hz

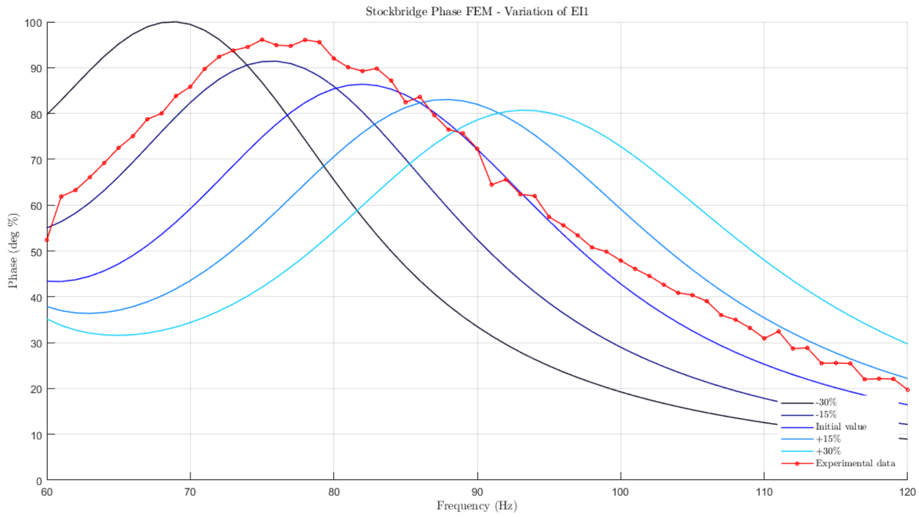

Figure 2.11: Phase curves as a function of EI_1, 60-120 Hz

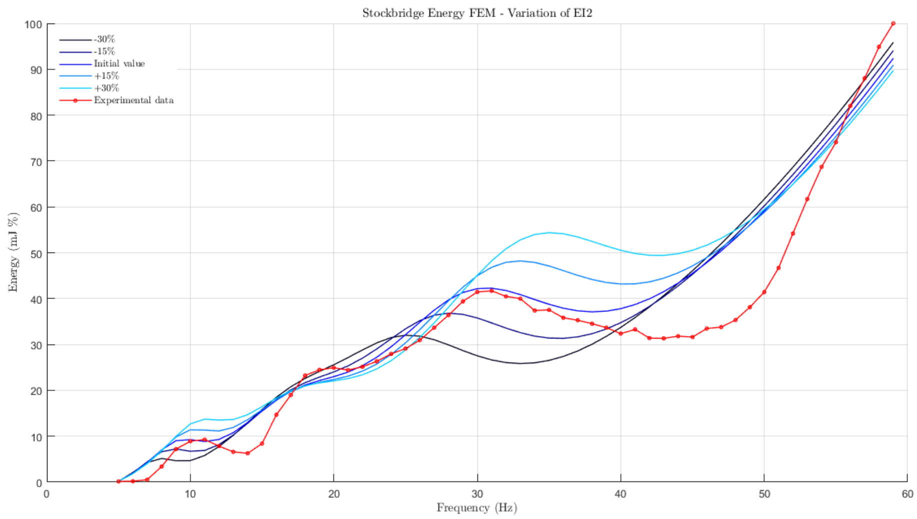

Figure 2.12: Energy curves as a function of EI_2, 5-59 Hz

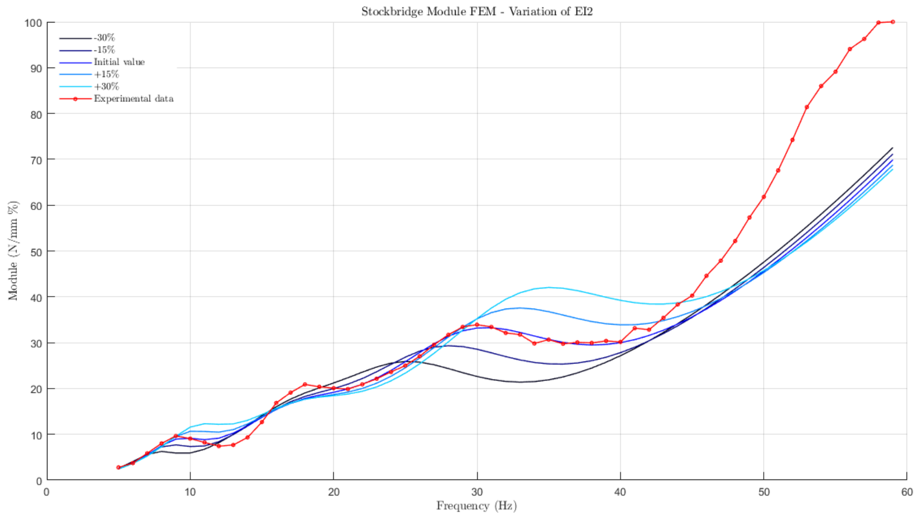

Figure 2.13: Modulus curves as a function of EI_2, 5-59 Hz

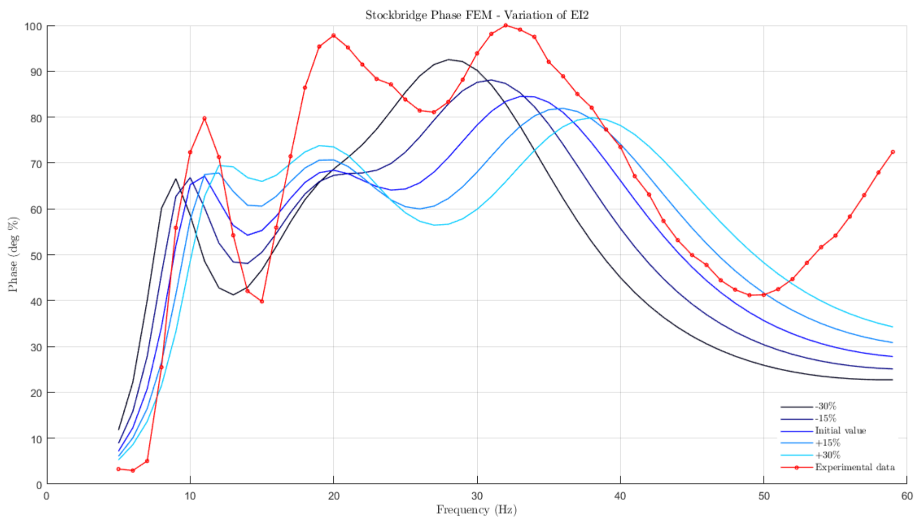

Figure 2.14: Phase curves as a function of EI_2, 5-59 Hz

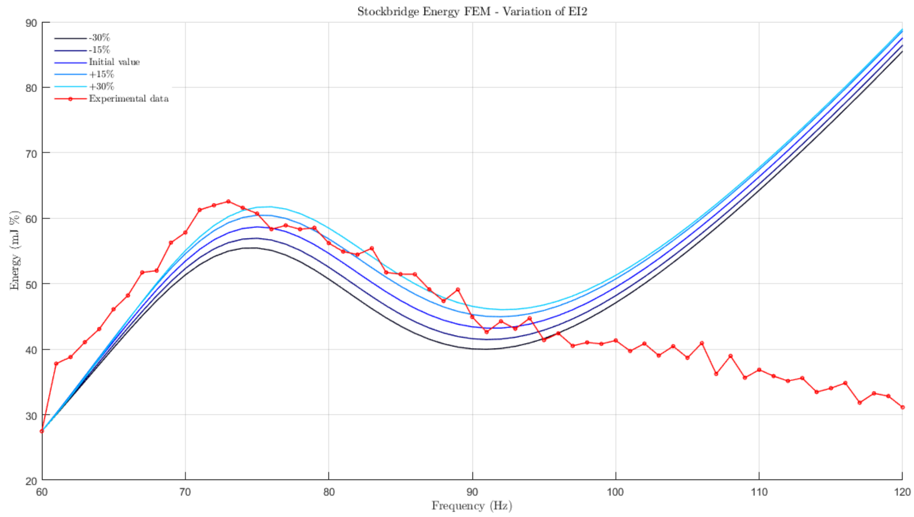

Figure 2.15: Energy curves as a function of EI_2, 60-120 Hz

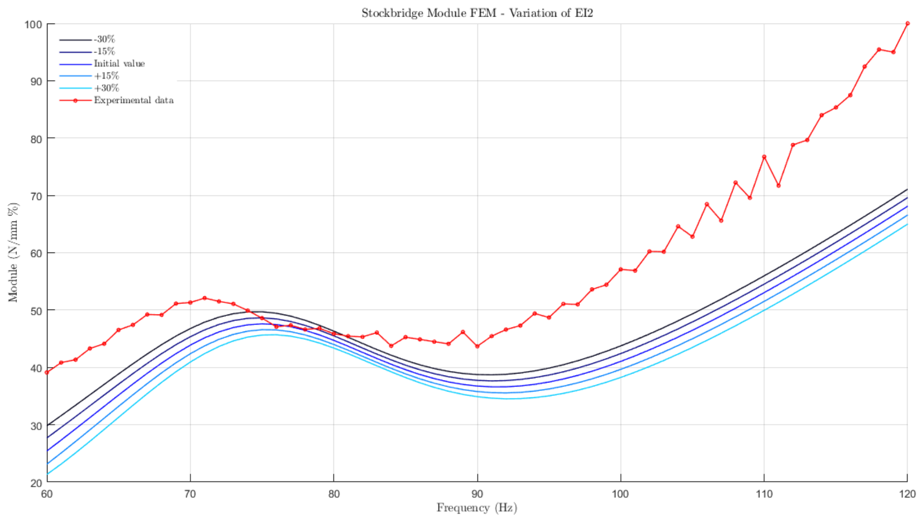

Figure 2.16: Modulus curves as a function of EI_2, 60-120 Hz

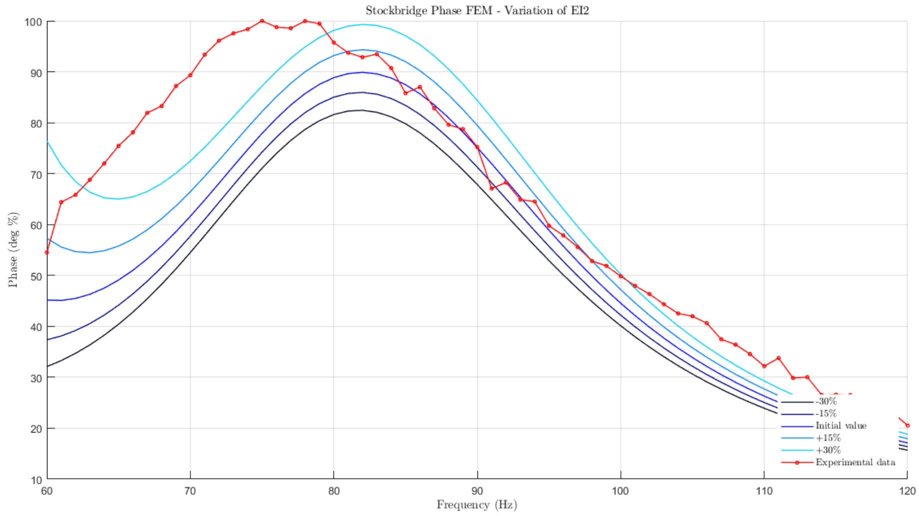

Figure 2.17: Phase curves as a function of EI_2, 60-120 Hz

2.2.3 h_1 hysteresis coefficient variation

In this section the plots for the variation of the hysteresis coefficient h_1 are shown. This corresponds to the hysteresis related to the shorter side of the messenger cable. As expected, the variation of this parameter increases or decreases the bell-shape amplitude curve related to the related to the second and the fourth modal shape.

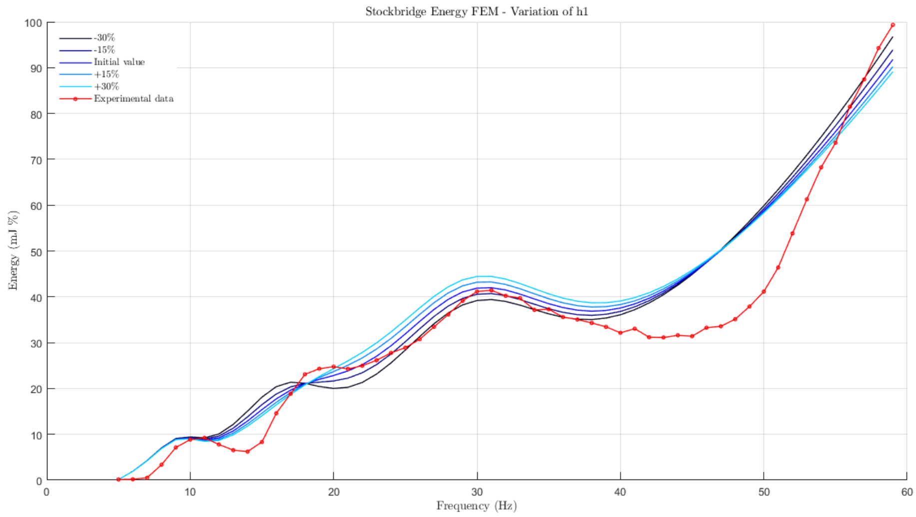

Figure 2.18: Energy curves as a function of h_1, 5-59 Hz

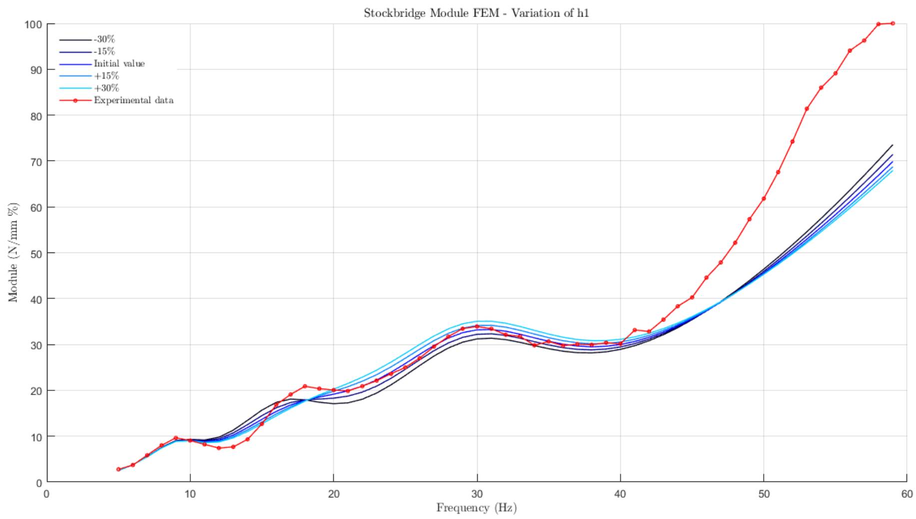

Figure 2.19: Modulus curves as a function of h_1, 5-59 Hz

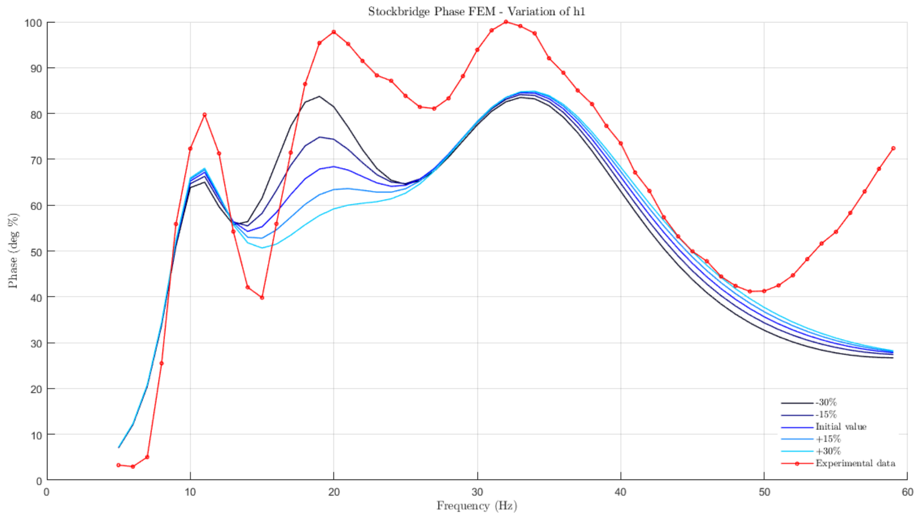

Figure 2.20: Phase curves as a function of h_1, 5-59 Hz

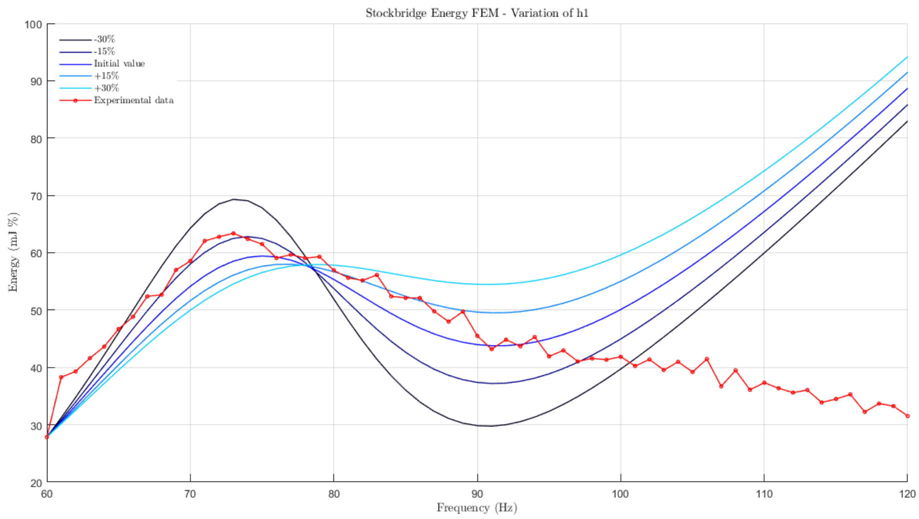

Figure 2.21: Energy curves as a function of h_1, 60-120 Hz

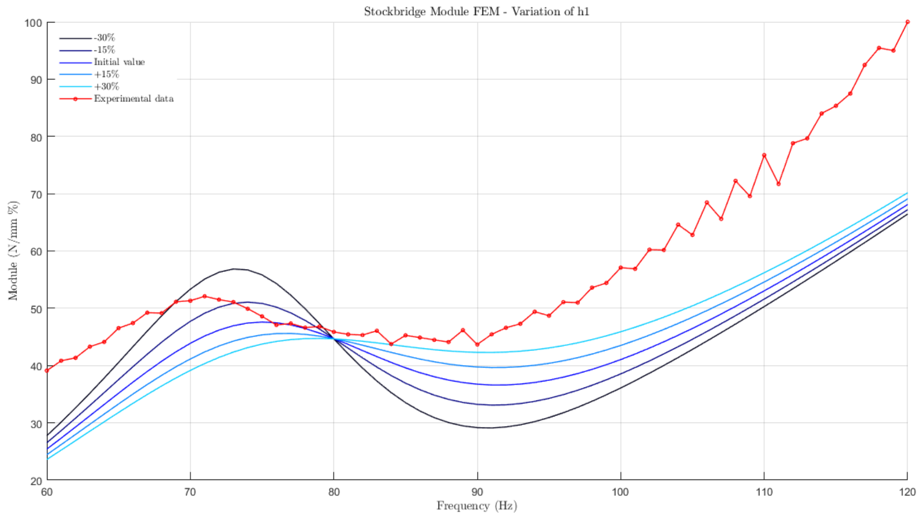

Figure 2.22: Modulus curves as a function of h_1, 60-120 Hz

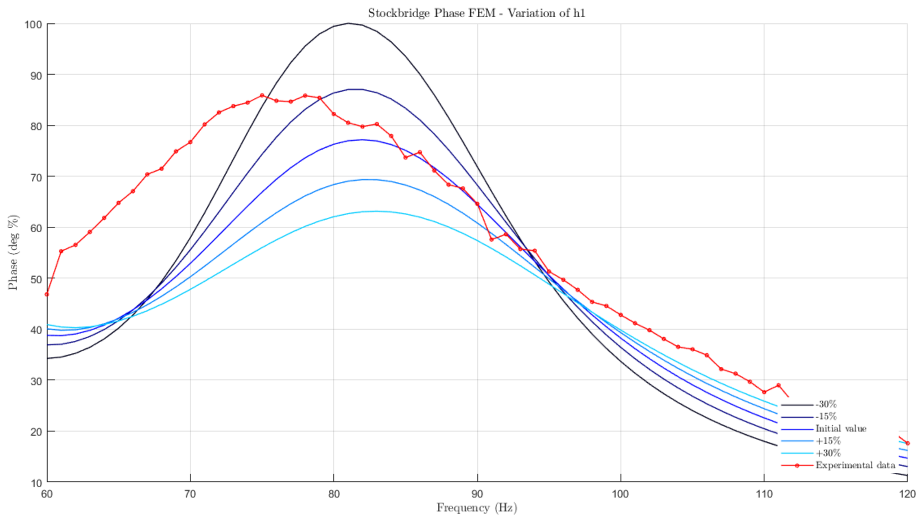

Figure 2.23: Phase curves as a function of h_1, 60-120 Hz

2.2.4 h_2 hysteresis coefficient variation

Here are plots showing the variation of the hysteresis coefficient h_2. Specifically, this corresponds to the hysteresis associated with the shorter side of the messenger cable. The variation of this parameter has the expected effect of increasing or decreasing the bell-shape amplitude curve associated with the first and third modal shapes, respectively.

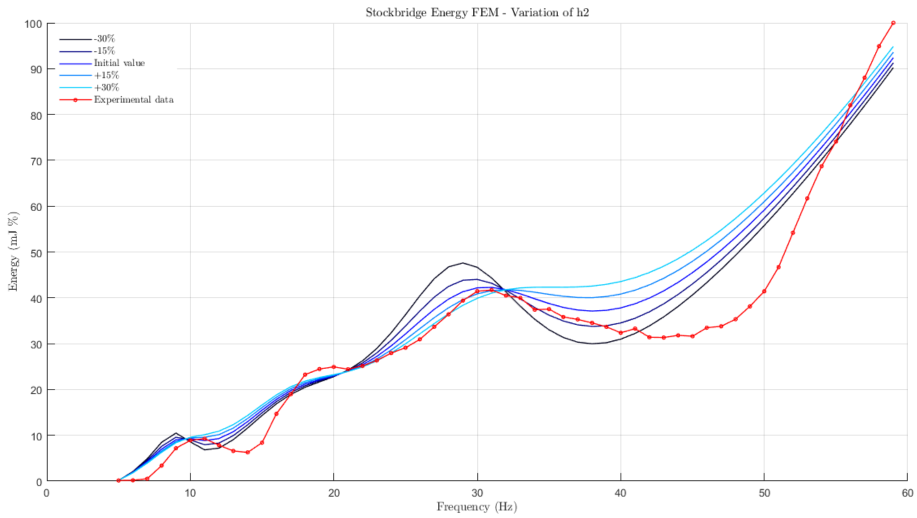

Figure 2.24: Energy curves as a function of h_2, 5-59 Hz

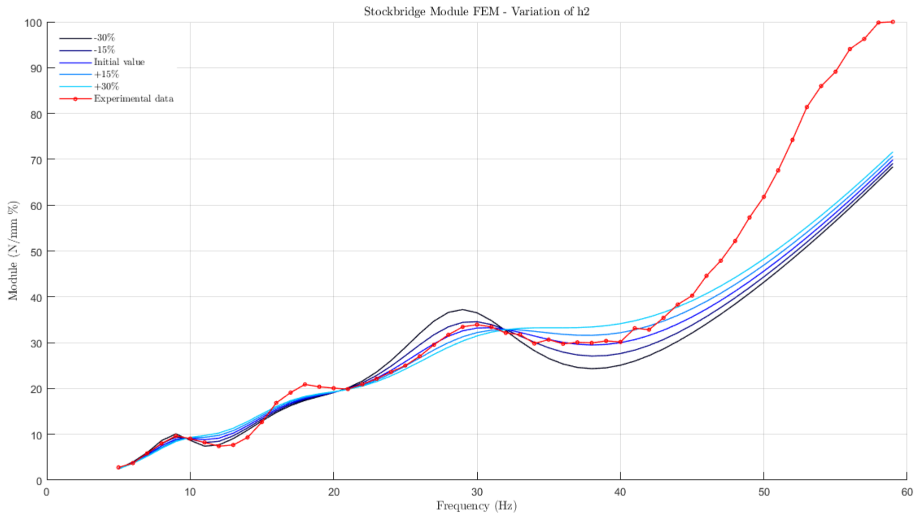

Figure 2.25: Modulus curves as a function of h_2, 5-59 Hz

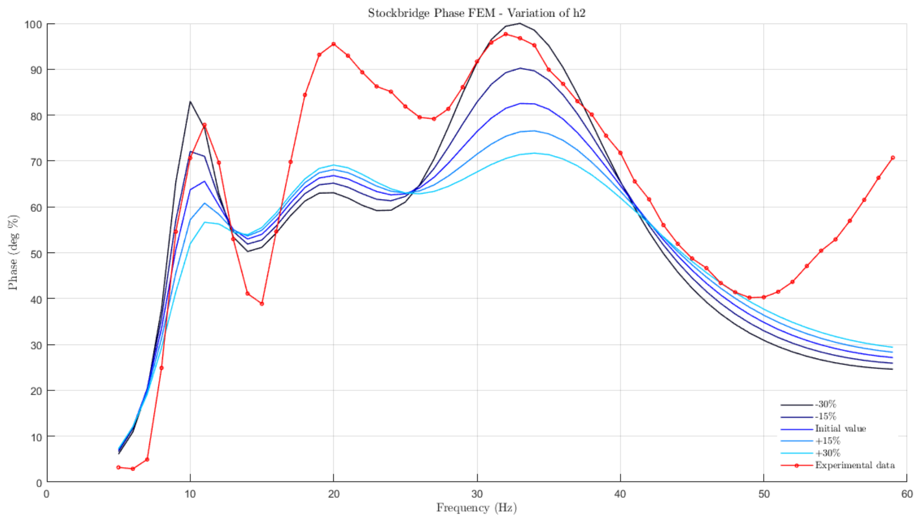

Figure 2.26: Phase curves as a function of h_2, 5-59 Hz

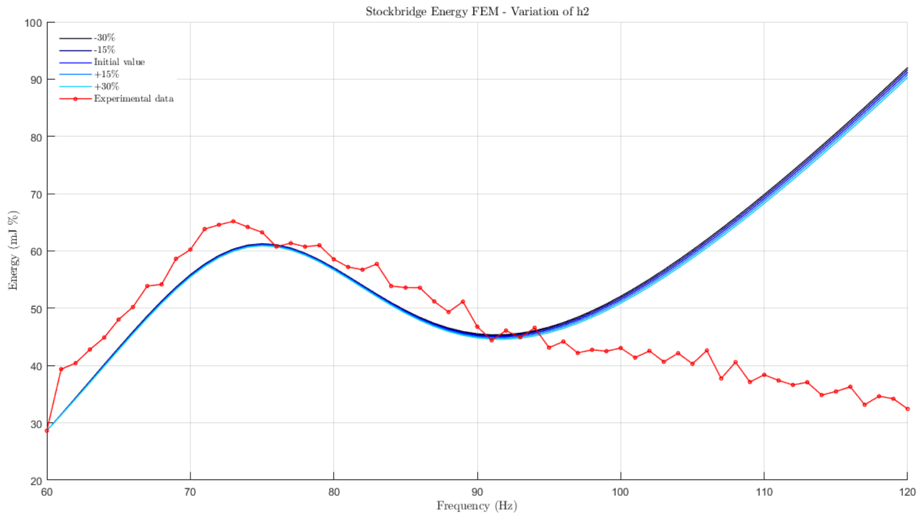

Figure 2.27: Energy curves as a function of h_2, 60-120 Hz

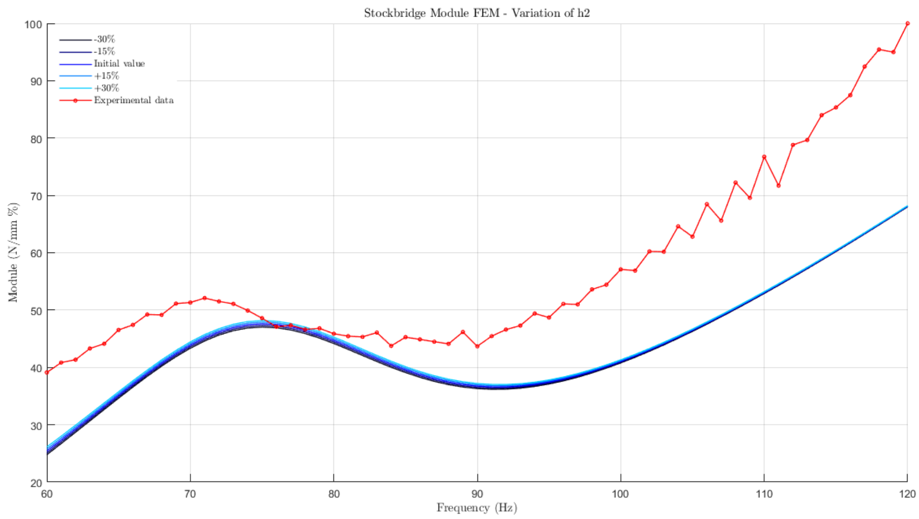

Figure 2.28: Modulus curves as a function of h_2, 60-120 Hz

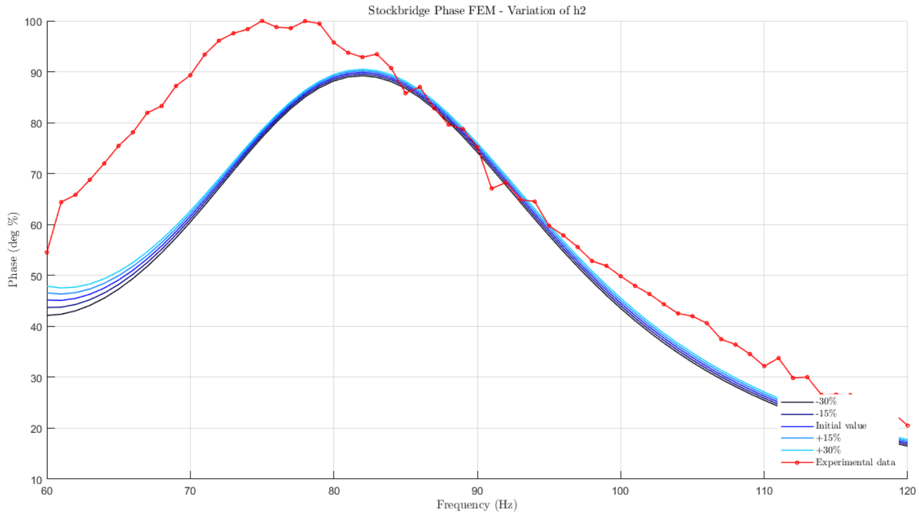

Figure 2.29: Phase curves as a function of h_2, 60-120 Hz

2.2.5 L_1 length variation

In this section the L_1 variation plots are reported. This length corresponds to the length of the shorter part of the messenger cable. This parameter is important since it appears in all matrices. It is related to the contributions of x_1 and φ_1, associated with m_1, as well as to x_c and φ_c, associated with m_c. It turns out that by increasing the length, the relative values of the mass matrix increase while the relative values of the stiffness and damping matrix decrease.

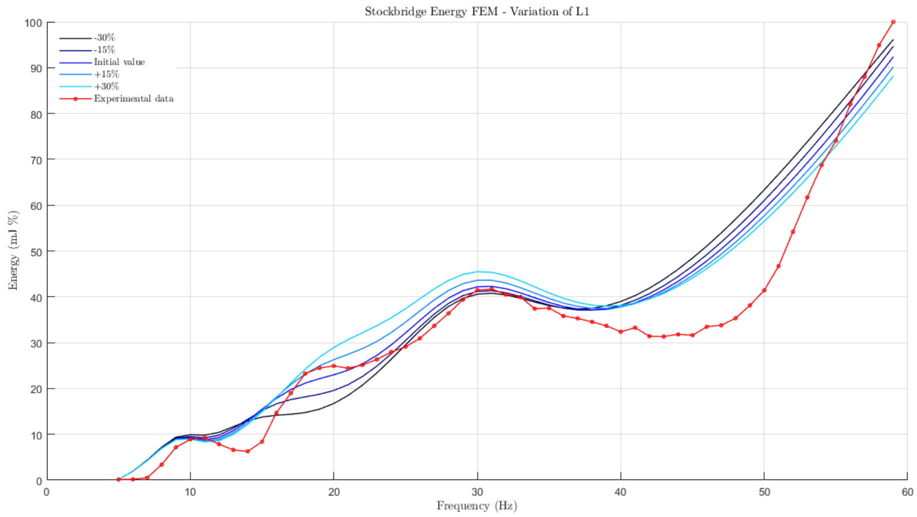

Figure 2.30: Energy curves as a function of L_1, 5-59 Hz

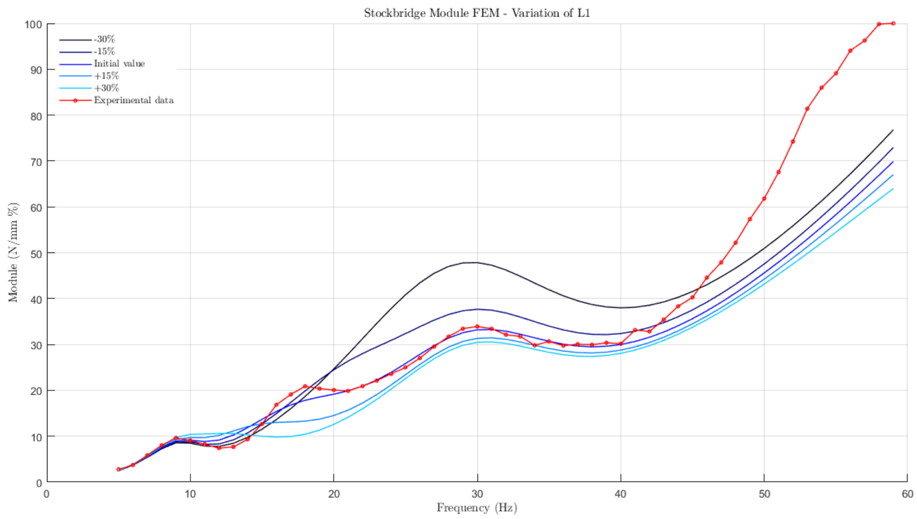

Figure 2.31: Modulus curves as a function of L_1, 5-59 Hz

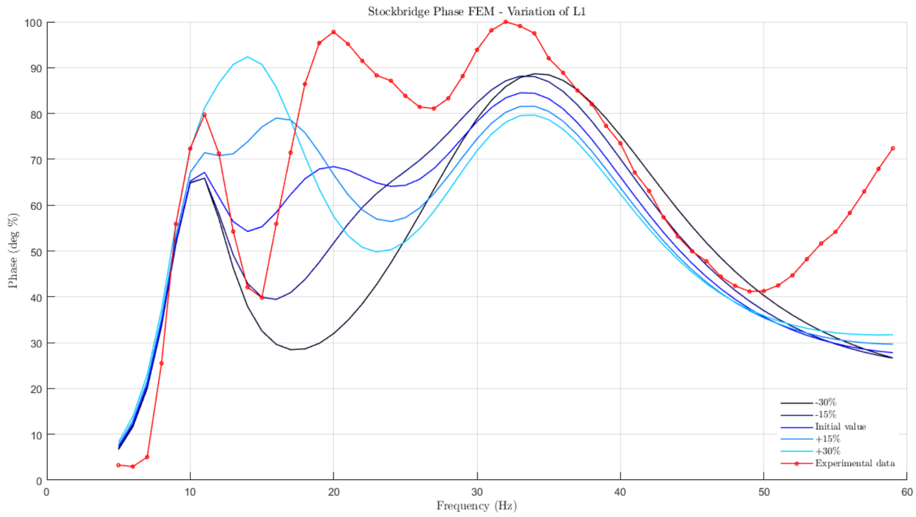

Figure 2.32: Phase curves as a function of L_1, 5-59 Hz

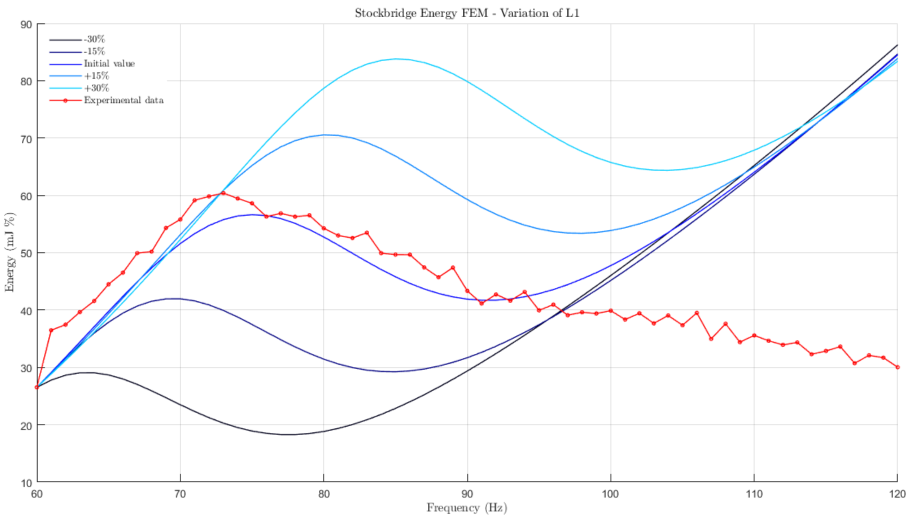

Figure 2.33: Energy curves as a function of L_1, 60-120 Hz

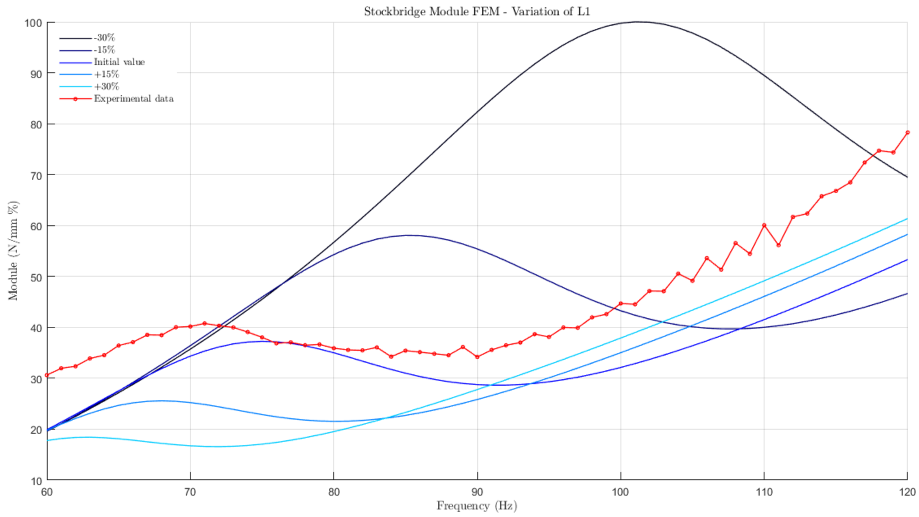

Figure 2.34: Modulus curves as a function of L_1, 60-120 Hz

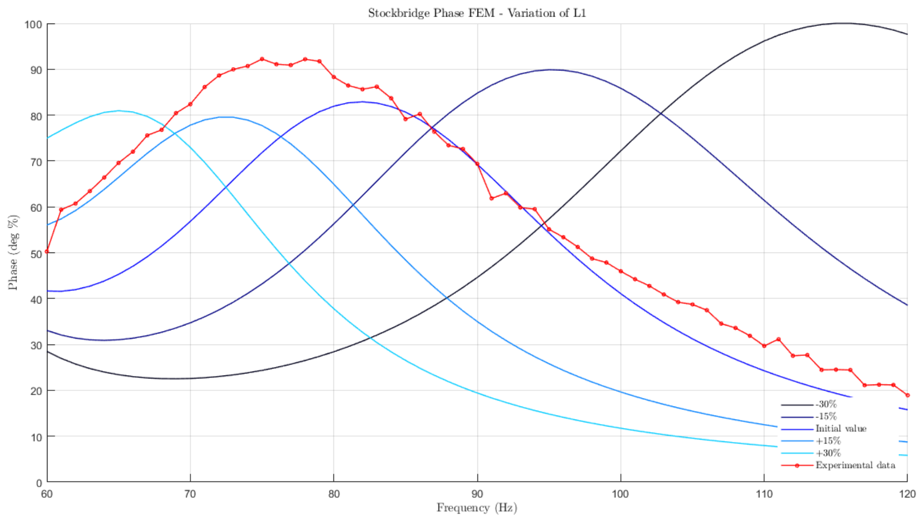

Figure 2.35: Phase curves as a function of L_1, 60-120 Hz

2.2.6 L_2 length variation

This section discusses L_2 variation plots. Respect to the previous, this represents the length of the messenger cable's longer part. The parameter appears in every matrix, like L_1. In this case, it is related to the contributions of x_2 and φ_2, associated with m_2, as well as to x_c and φ_c, associated with m_c. By increasing the length, the mass matrix's relative values increase while the stiffness and damping matrix's relative values decrease.

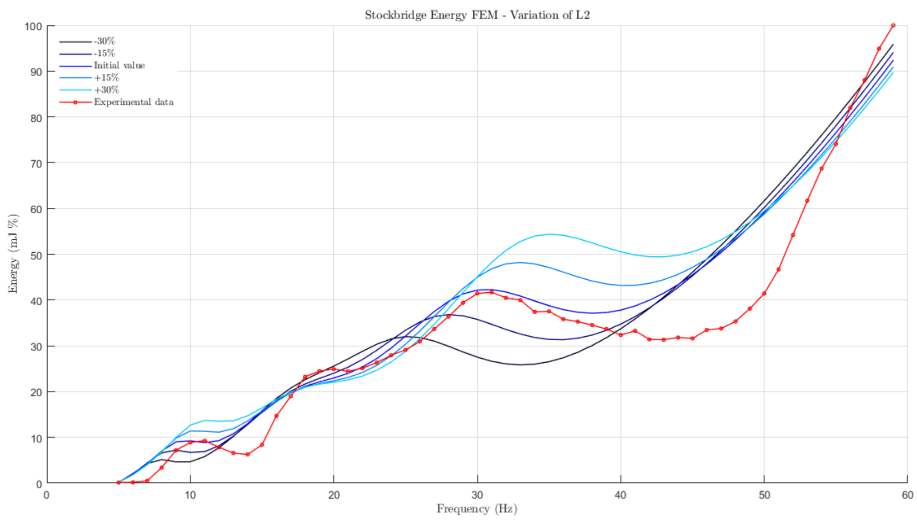

Figure 2.36: Energy curves as a function of L_2, 5-59 Hz

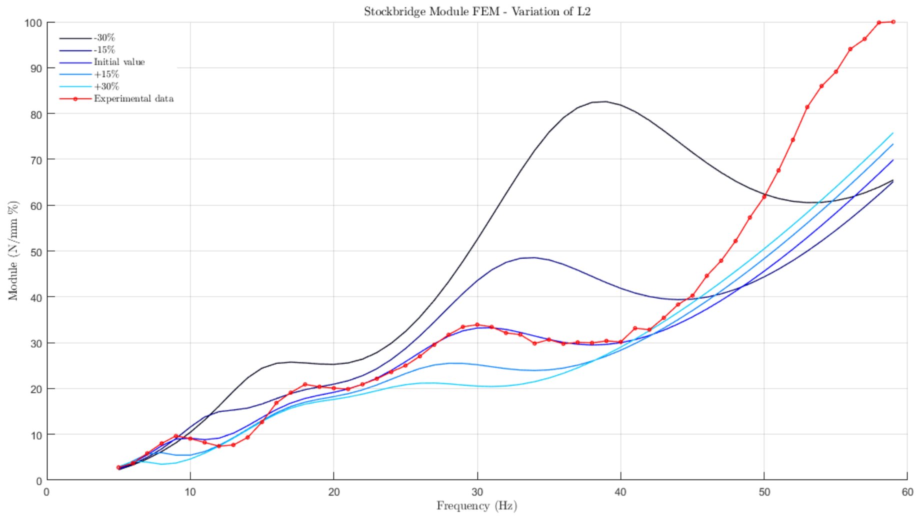

Figure 2.37: Modulus curves as a function of L_2, 5-59 Hz

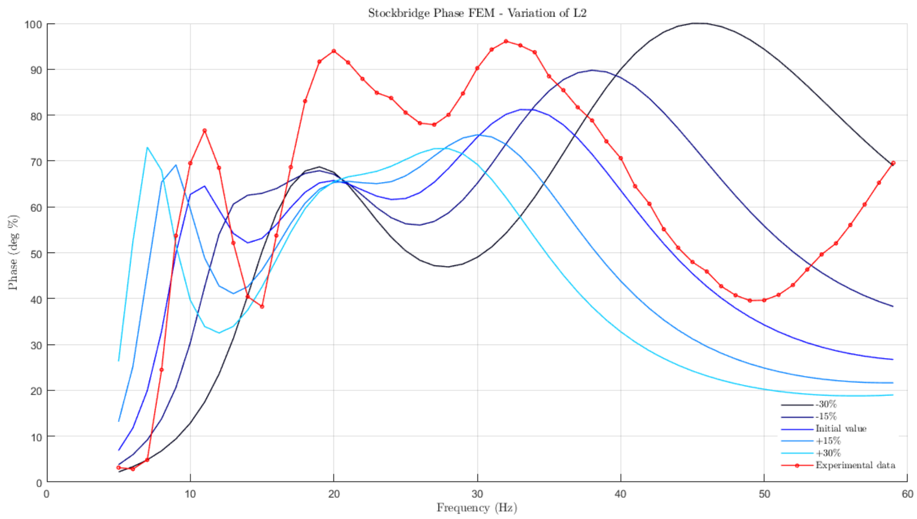

Figure 2.38: Phase curves as a function of L_2, 5-59 Hz

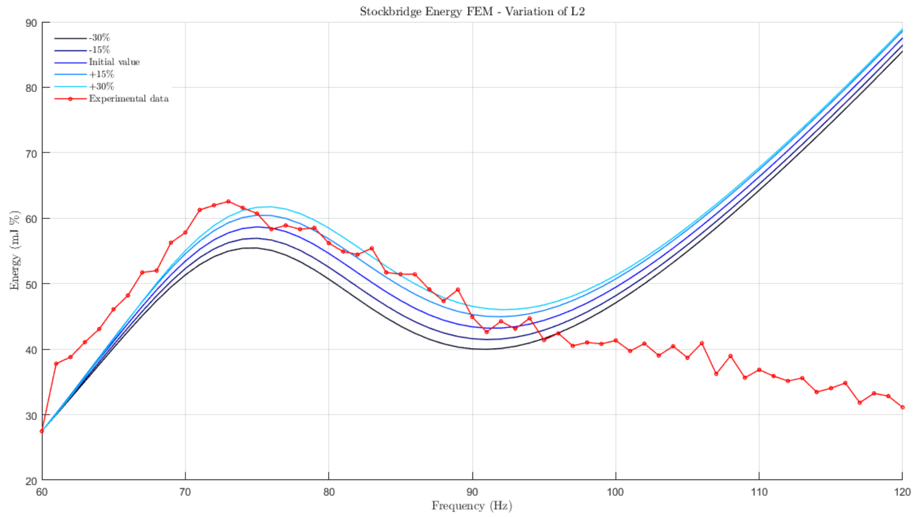

Figure 2.39: Energy curves as a function of L_2, 60-120 Hz

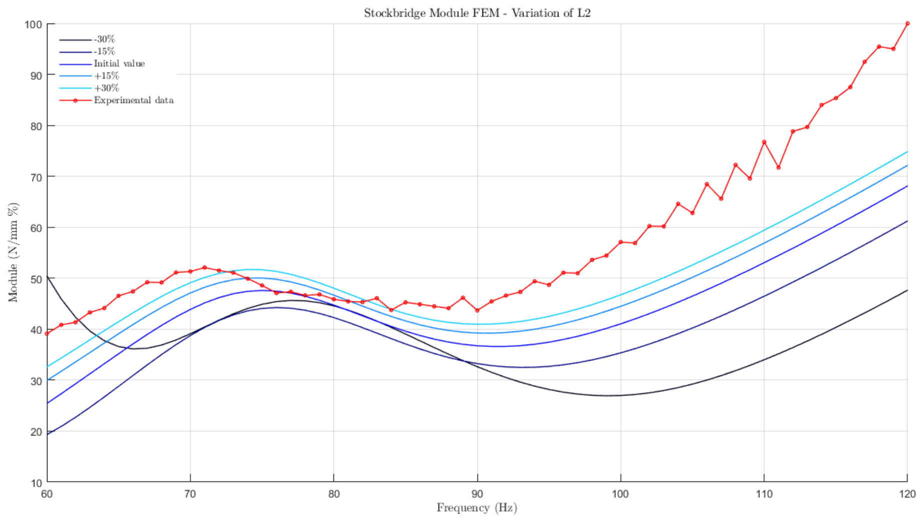

Figure 2.40: Modulus curves as a function of L_2, 60-120 Hz

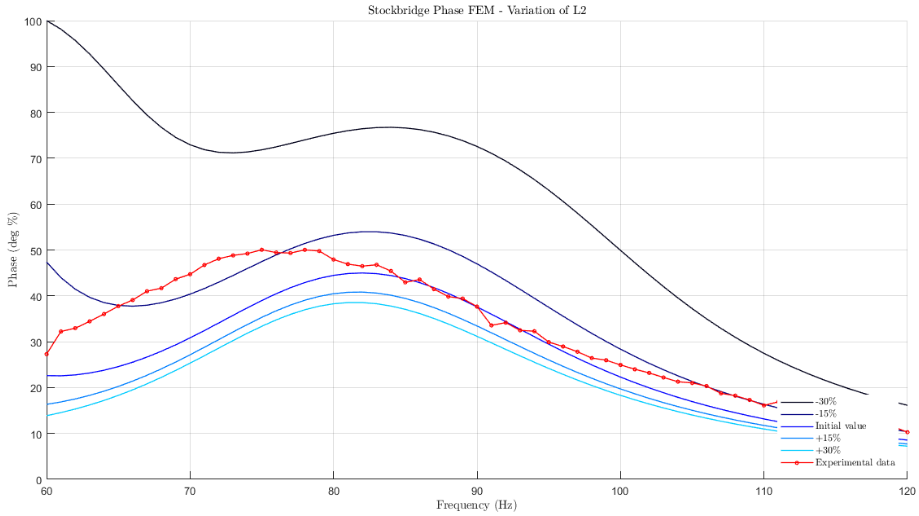

Figure 2.41: Phase curves as a function of L_2, 60-120 Hz

2.2.7 a_1 length variation

Graphs obtained by varying the parameter a_1 are illustrated in this part. As said in the last chapters, it is the distance between the barycenter and the junction of the mass m_1. Mass matrix is affected directly by this parameter.

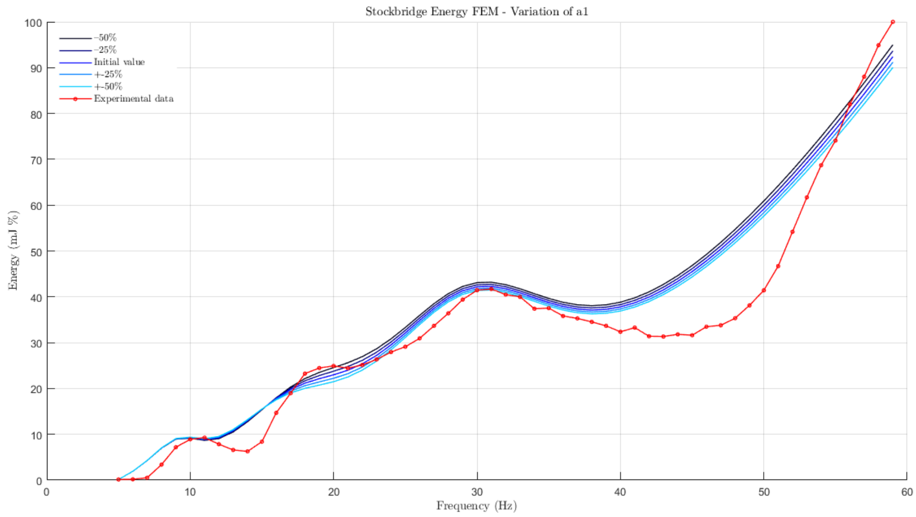

Figure 2.42: Energy curves as a function of a_1, 5-59 Hz

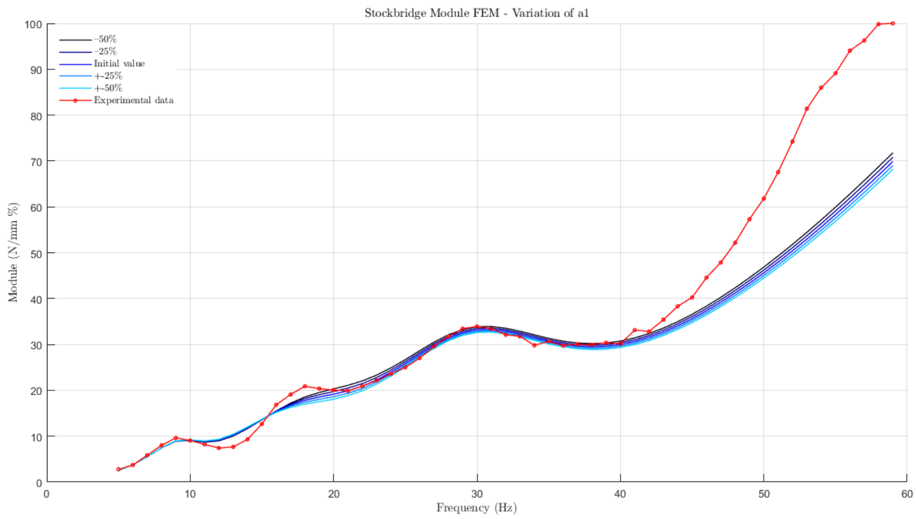

Figure 2.43: Modulus curves as a function of a_1, 5-59 Hz

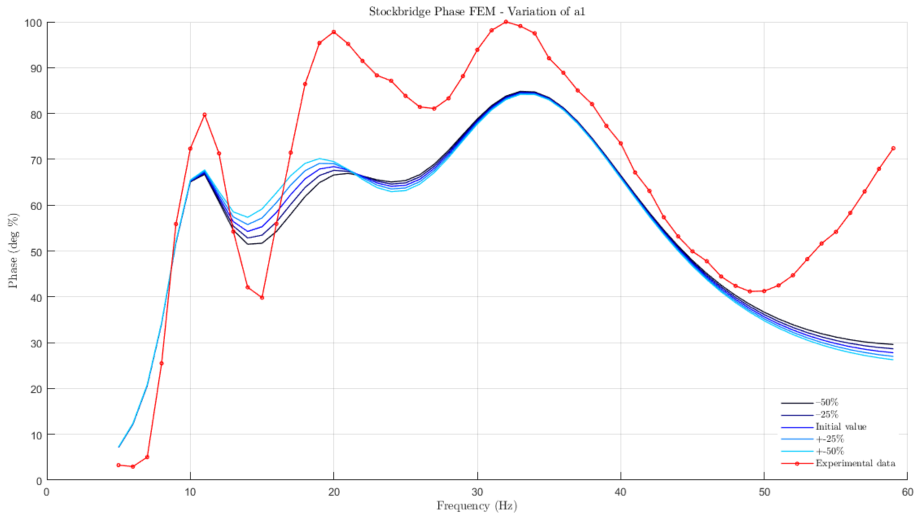

Figure 2.44: Phase curves as a function of a_1, 5-59 Hz

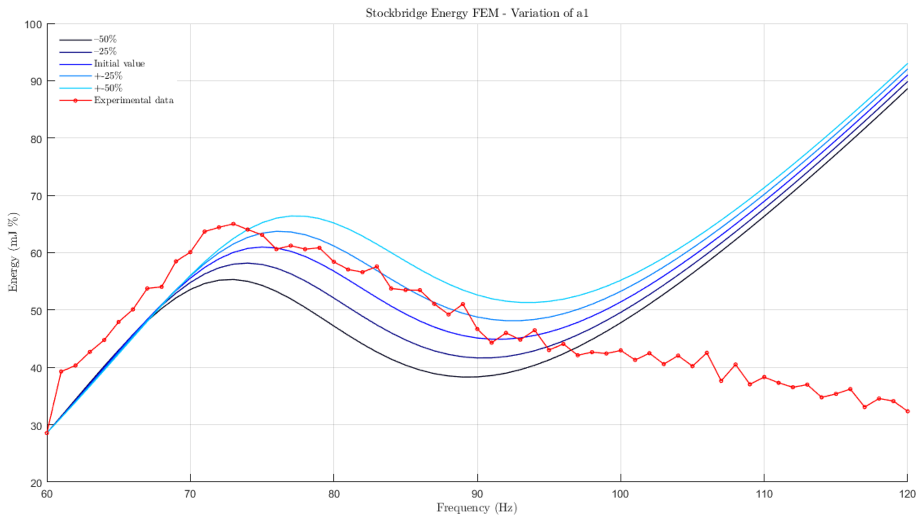

Figure 2.45: Energy curves as a function of a_1, 60-120 Hz

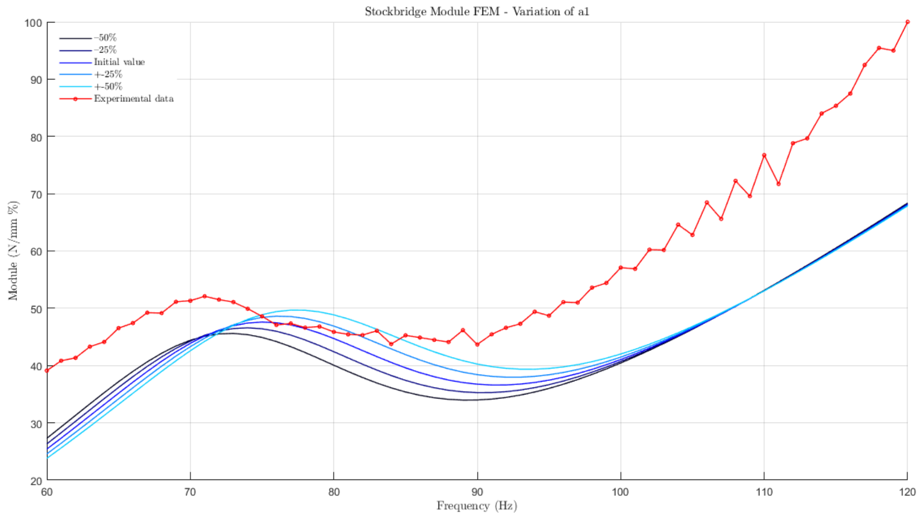

Figure 2.46: Modulus curves as a function of a_1, 60-120 Hz

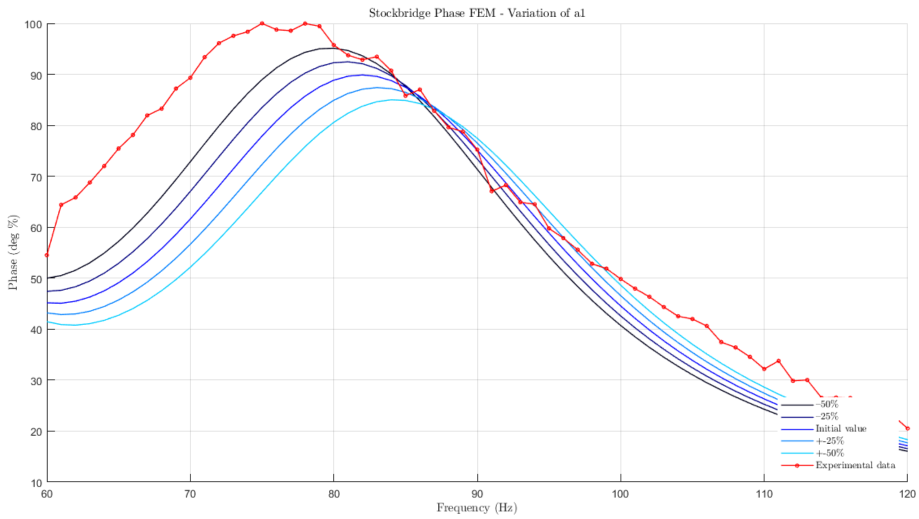

Figure 2.47: Phase curves as a function of a_1, 60-120 Hz

2.2.8 a_2 length variation

In this part, graphs in which the parameter a_2 is varied are illustrated. This is the distance between the barycenter and the mass junction m_2, as mentioned in previous chapters. Like a_1, also this parameter directly affects the mass matrix.

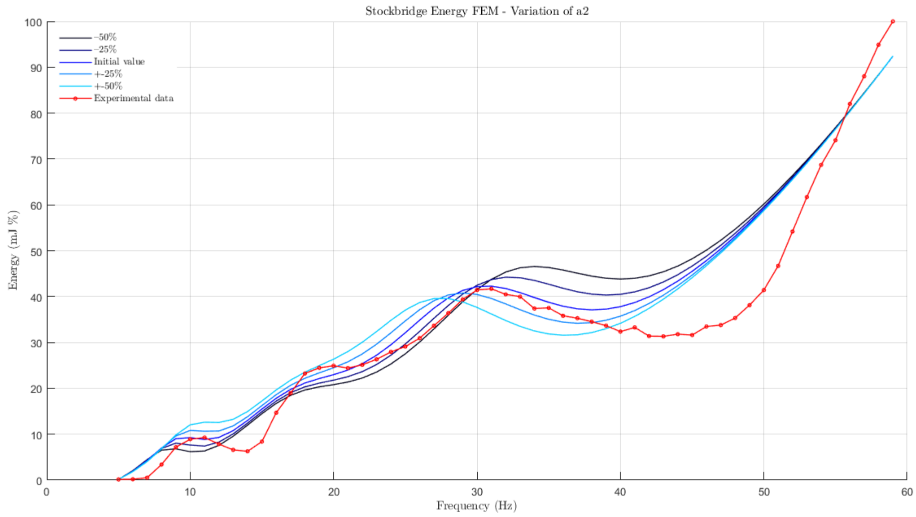

Figure 2.48: Energy curves as a function of a_2, 5-59 Hz

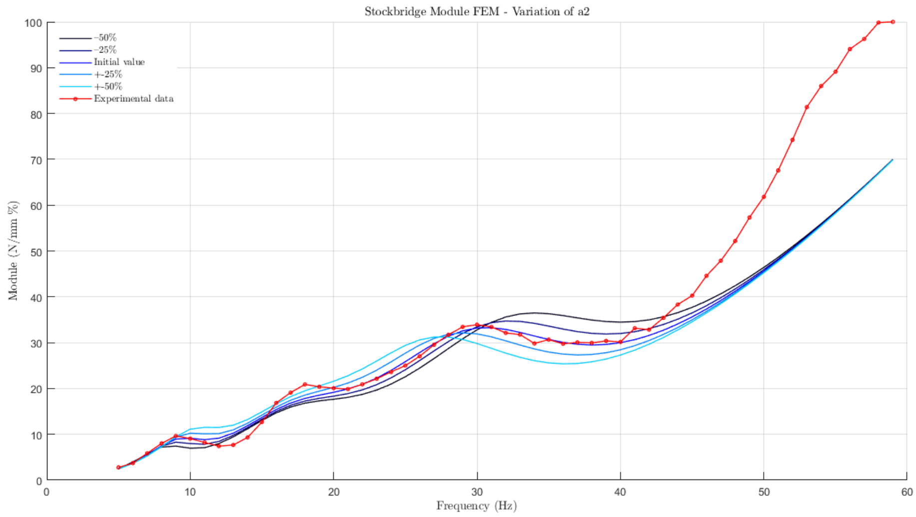

Figure 2.49: Modulus curves as a function of a_2, 5-59 Hz

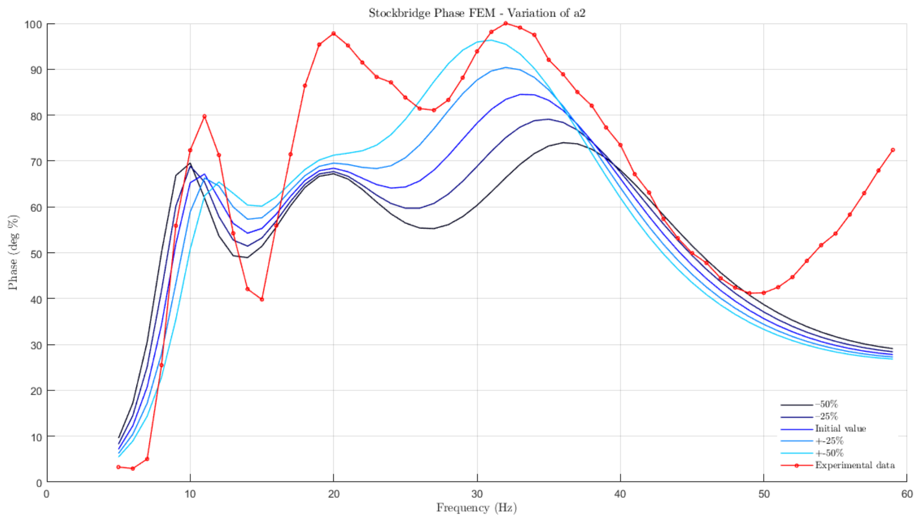

Figure 2.50: Phase curves as a function of a_2, 5-59 Hz

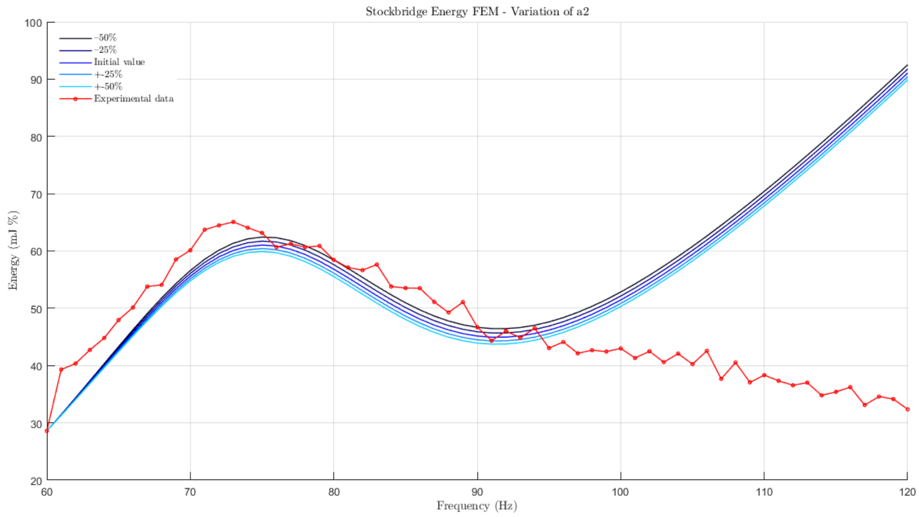

Figure 2.51: Energy curves as a function of a_2, 60-120 Hz

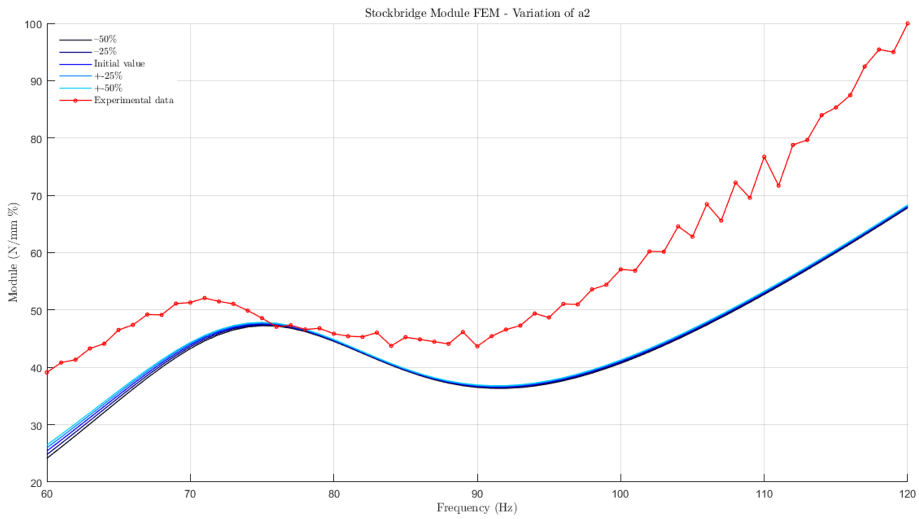

Figure 2.52: Modulus curves as a function of a_2, 60-120 Hz

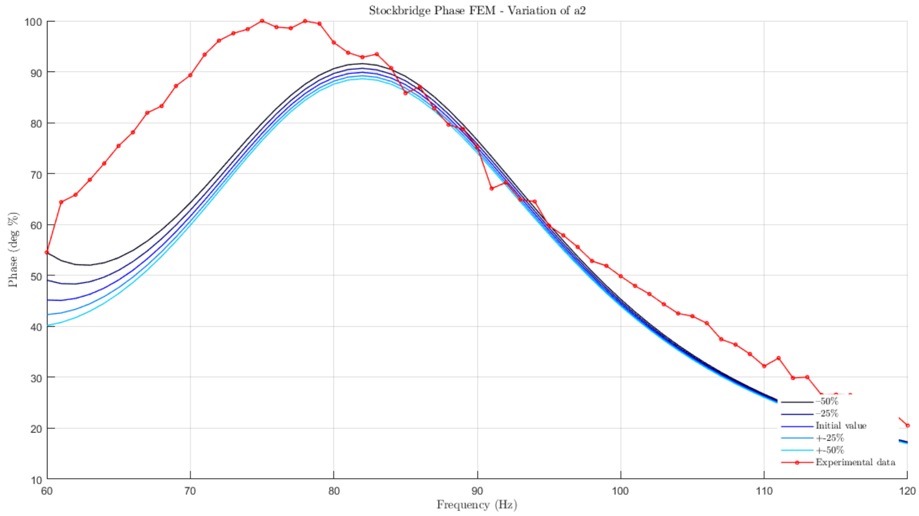

Figure 2.53: Phase curves as a function of a_2, 60-120 Hz

2.2.9 m_1 mass variation

In this part the graphs about the m_1 mass variation are presented. Among the cantilevered masses, this is the lightest one and it is located on the shorter side of the messenger cable. This parameter affects only the mass matrix.

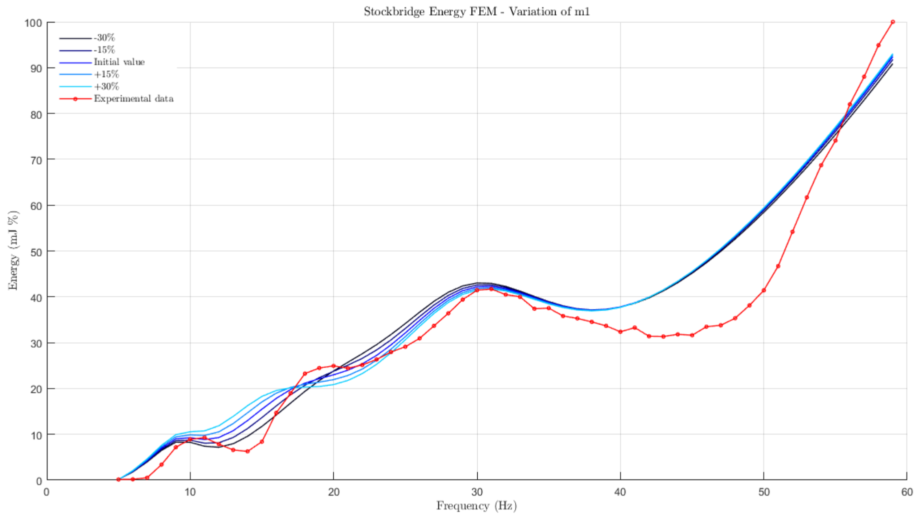

Figure 2.54: Energy curves as a function of m_1, 5-59 Hz

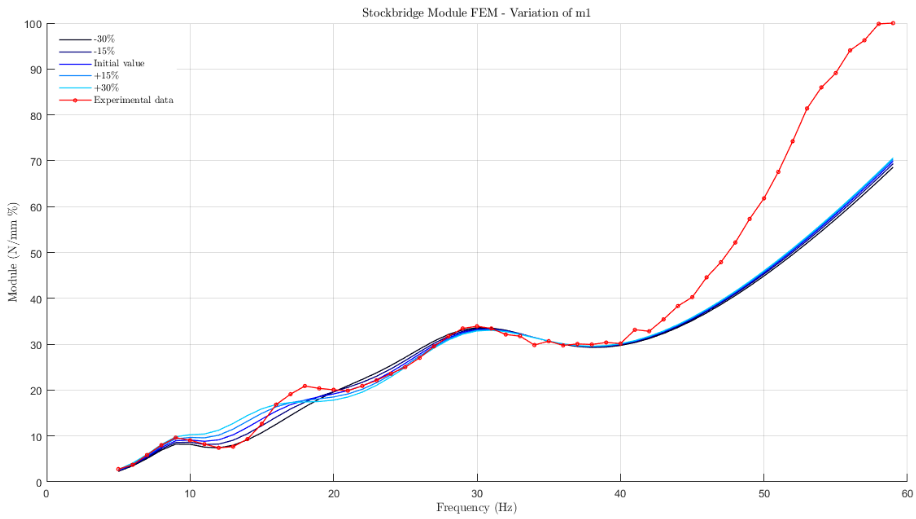

Figure 2.55: Modulus curves as a function of m_1, 5-59 Hz

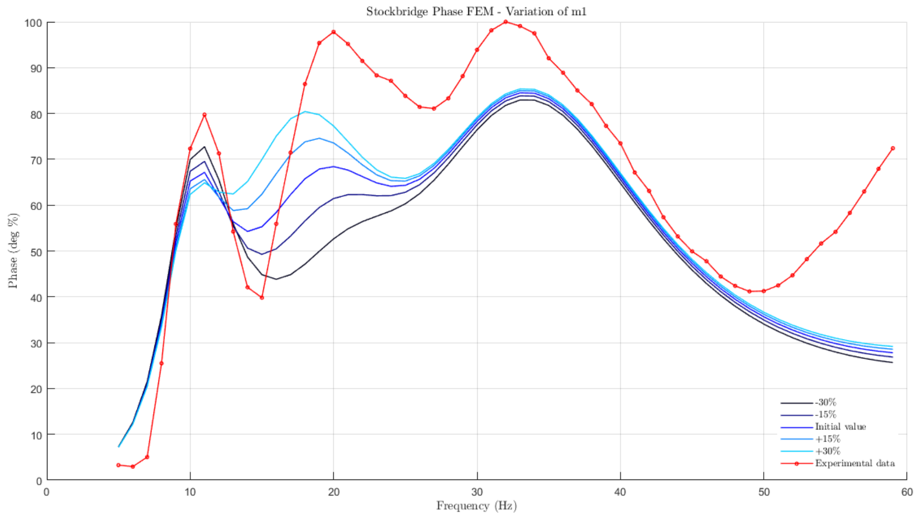

Figure 2.56: Phase curves as a function of m_1, 5-59 Hz

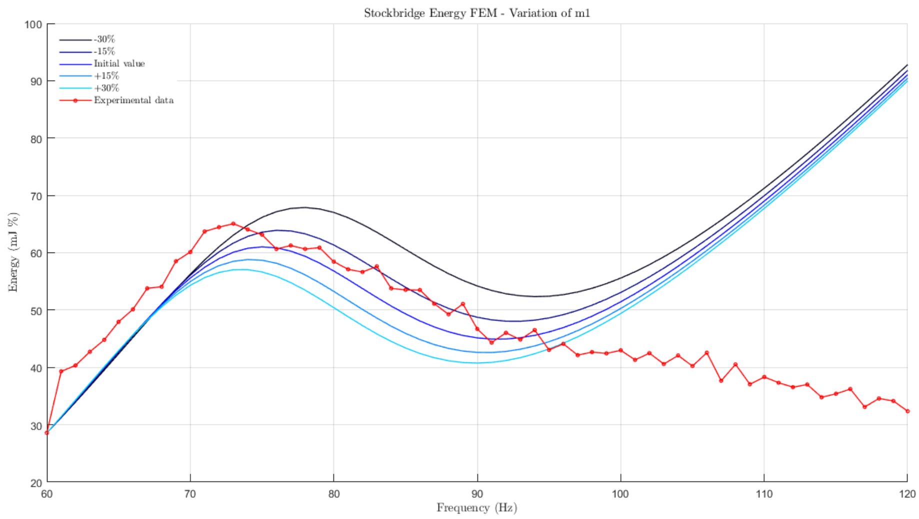

Figure 2.57: Energy curves as a function of m_1, 60-120 Hz

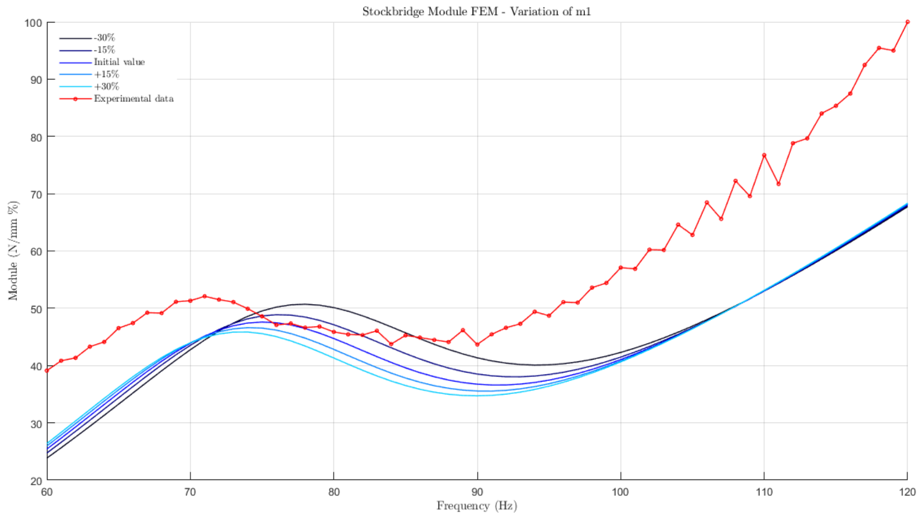

Figure 2.58: Modulus curves as a function of m_1, 60-120 Hz

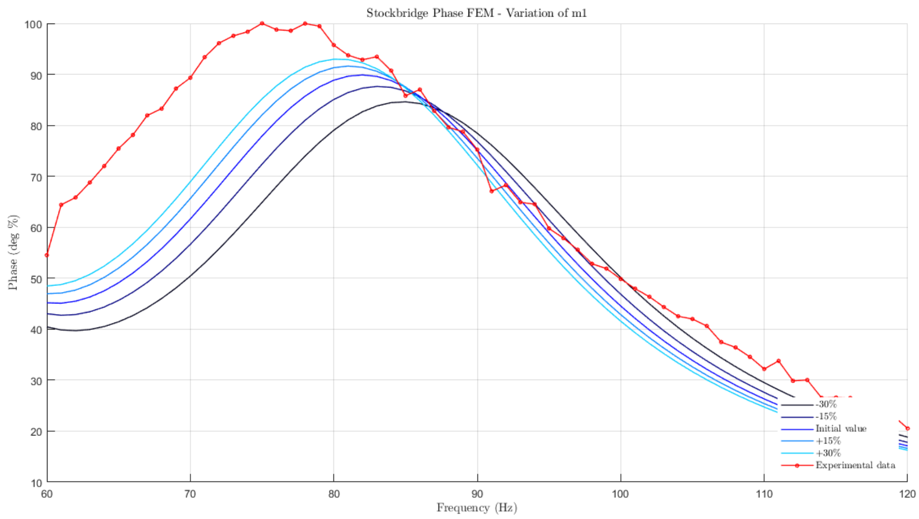

Figure 2.59: Phase curves as a function of m_1, 60-120 Hz

2.2.10 m_2 mass variation

Here are exposed the plots about the variation of the mass m_2. This is the heaviest cantilevered mass and it is located on the longer side of the messenger cable. As the latter, this parameter affects only the mass matrix.

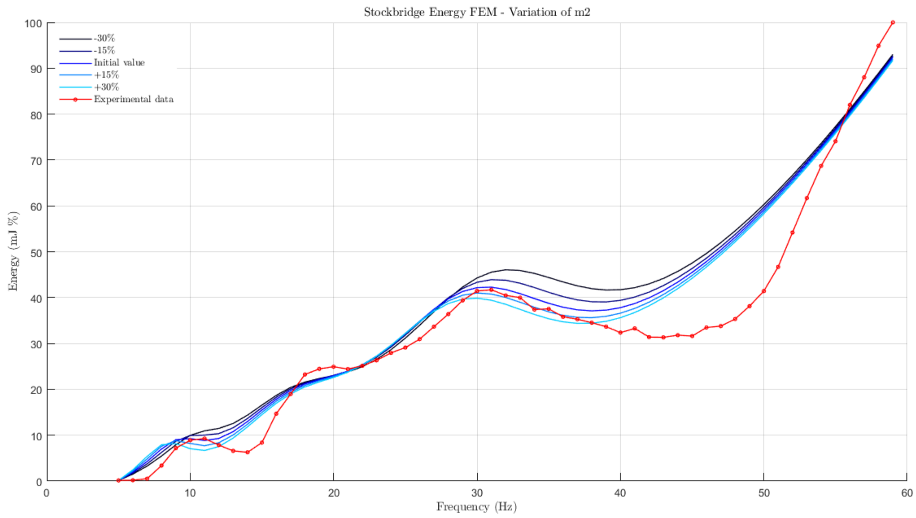

Figure 2.60: Energy curves as a function of m_2, 5-59 Hz

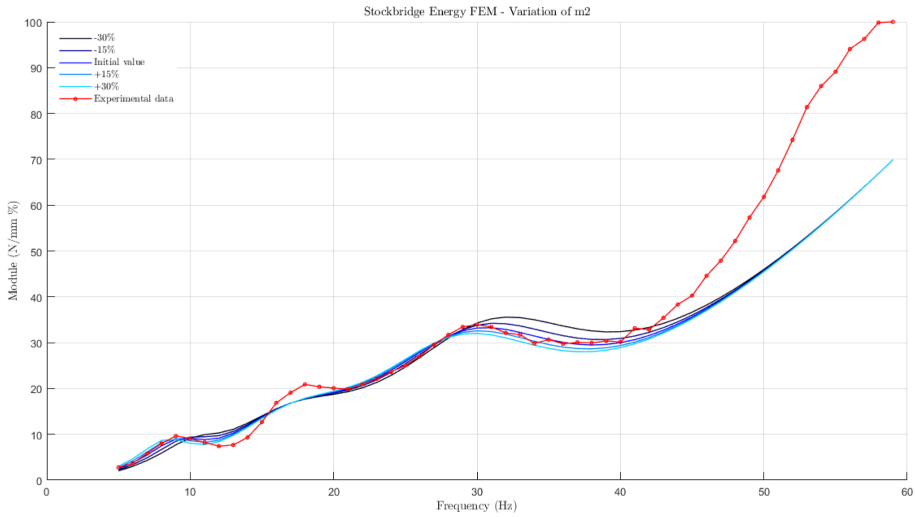

Figure 2.61: Modulus curves as a function of m_2, 5-59 Hz

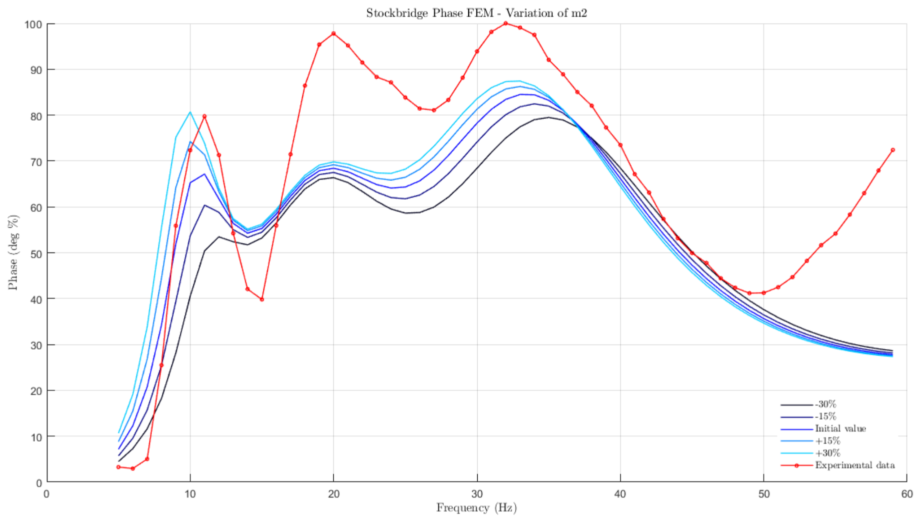

Figure 2.62: Phase curves as a function of m_2, 5-59 Hz

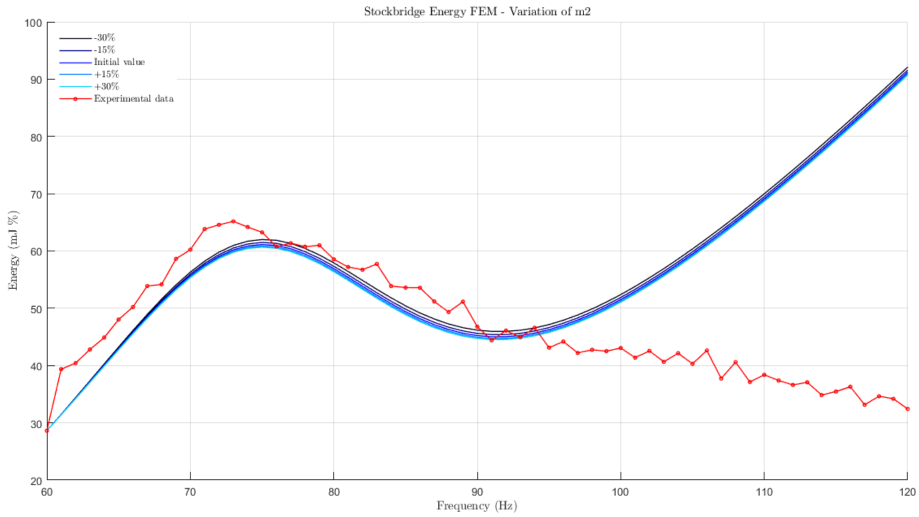

Figure 2.63: Energy curves as a function of m_2, 60-120 Hz

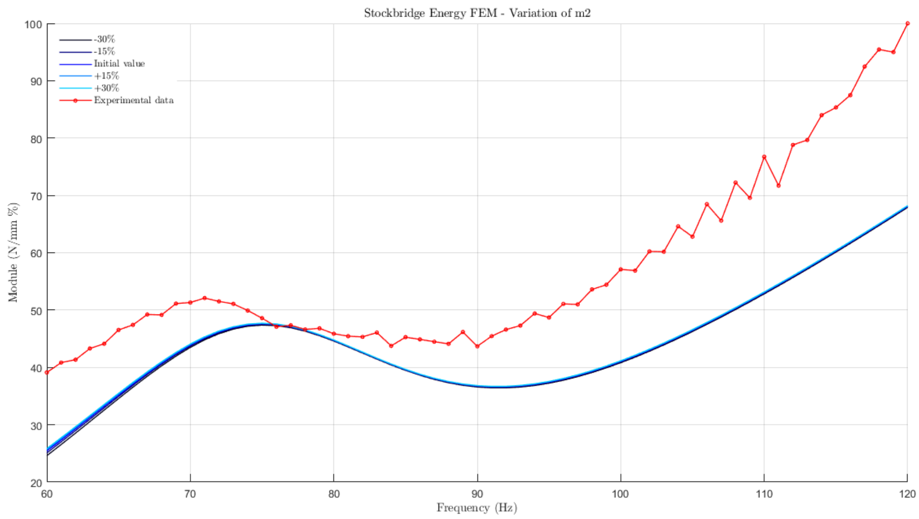

Figure 2.64: Modulus curves as a function of m_2, 60-120 Hz

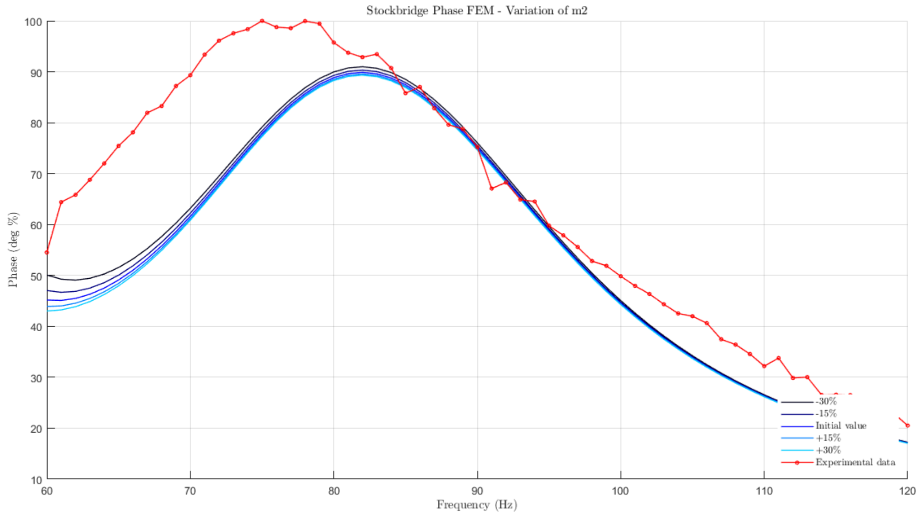

Figure 2.65: Phase curves as a function of m_2, 60-120 Hz

2.2.11 m_c mass variation

The analysis of the change in clamp body mass m_c is presented in this part. This parameter affects all the modal shapes of the damper, intervening only in the mass matrix.

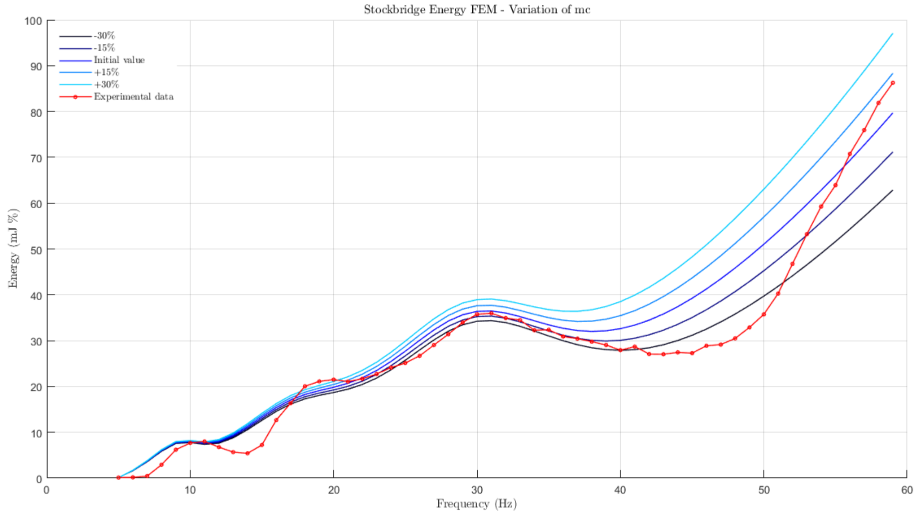

Figure 2.66: Energy curves as a function of m_c, 5-59 Hz

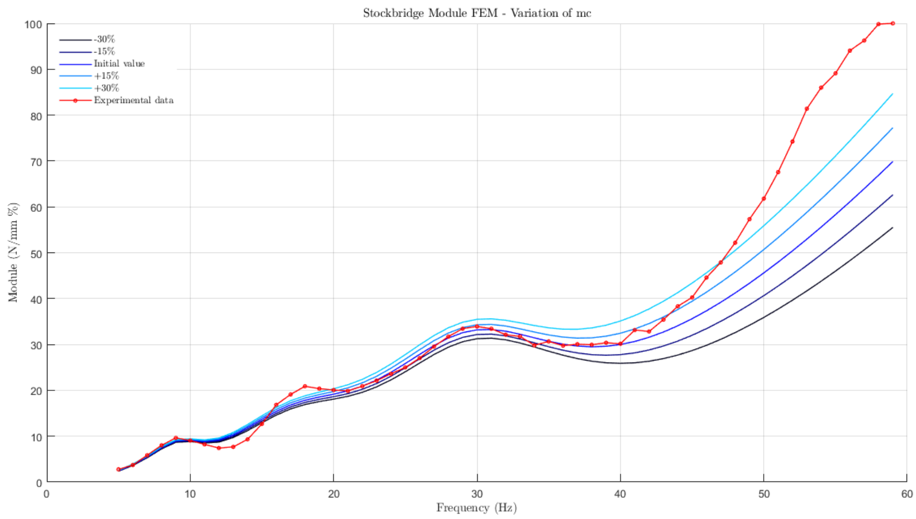

Figure 2.67: Modulus curves as a function of m_c, 5-59 Hz

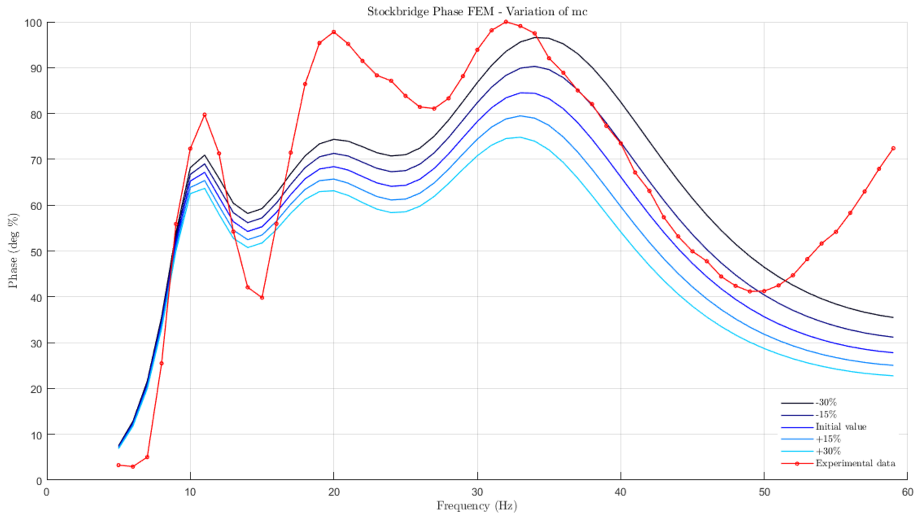

Figure 2.68: Phase curves as a function of m_c, 5-59 Hz

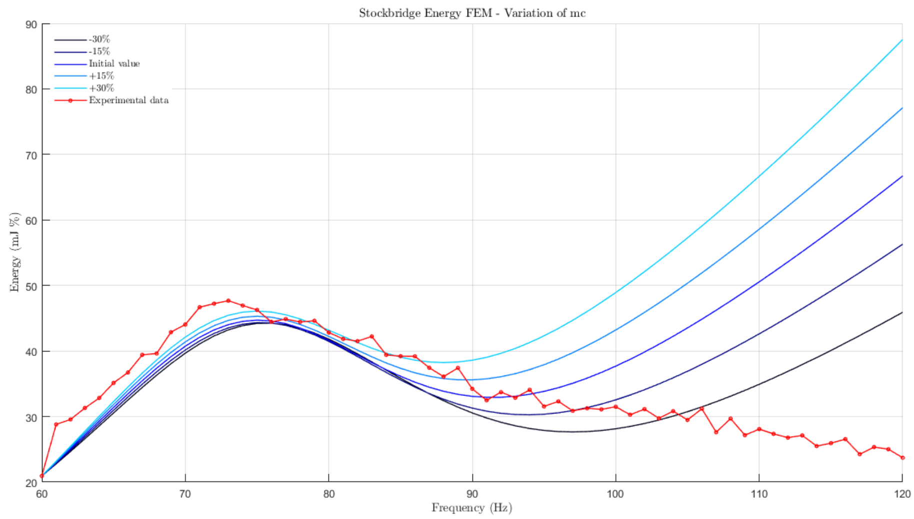

Figure 2.69: Energy curves as a function of m_c, 60-120 Hz

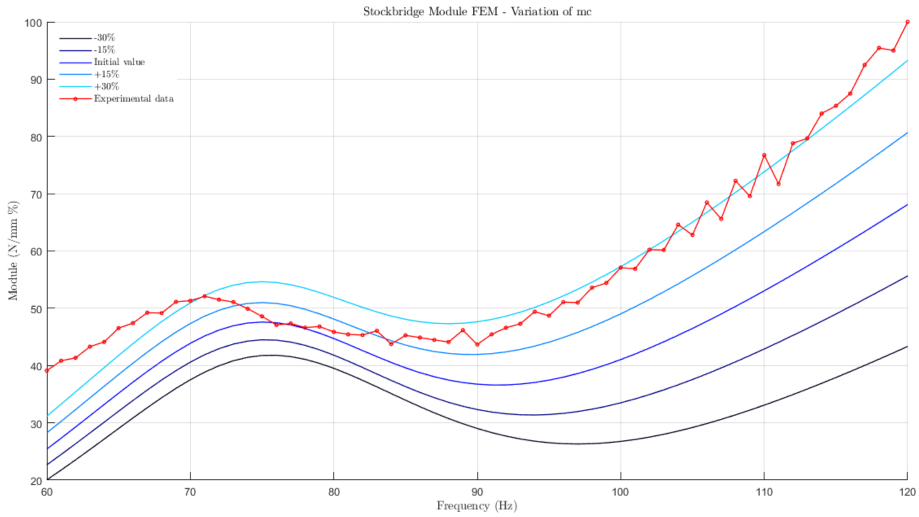

Figure 2.70: Modulus curves as a function of m_c, 60-120 Hz

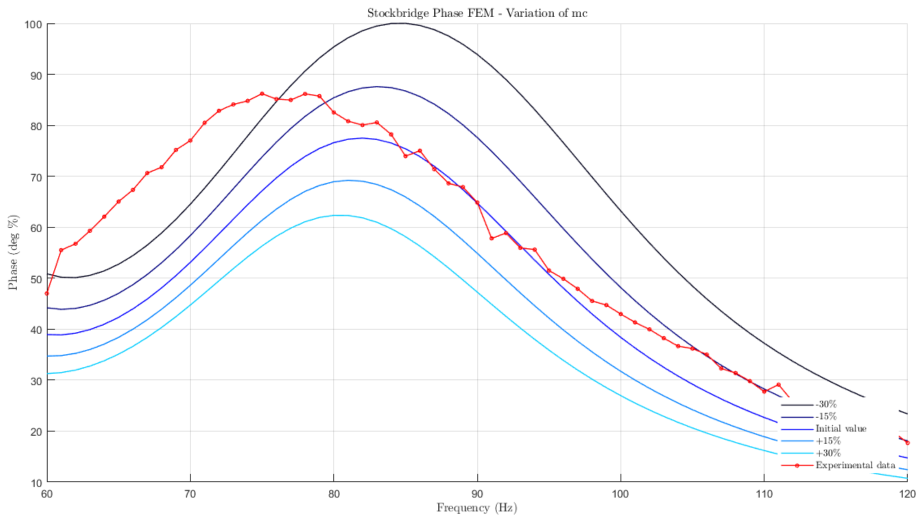

Figure 2.71: Phase curves as a function of m_c, 60-120 Hz

2.2.12 J_1 mass moment of inertia variation

In this section the plots for the variation of the mass moment of inertia J_1 are shown. This parameter affects the mass matrix, so the FEM models, in a similar way to the mass parameter m_1.

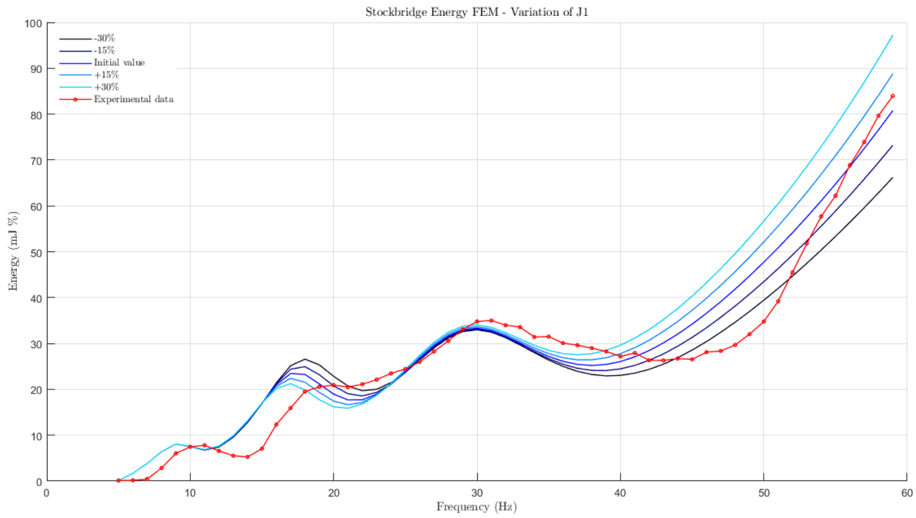

Figure 2.72: Energy curves as a function of J_1, 5-59 Hz

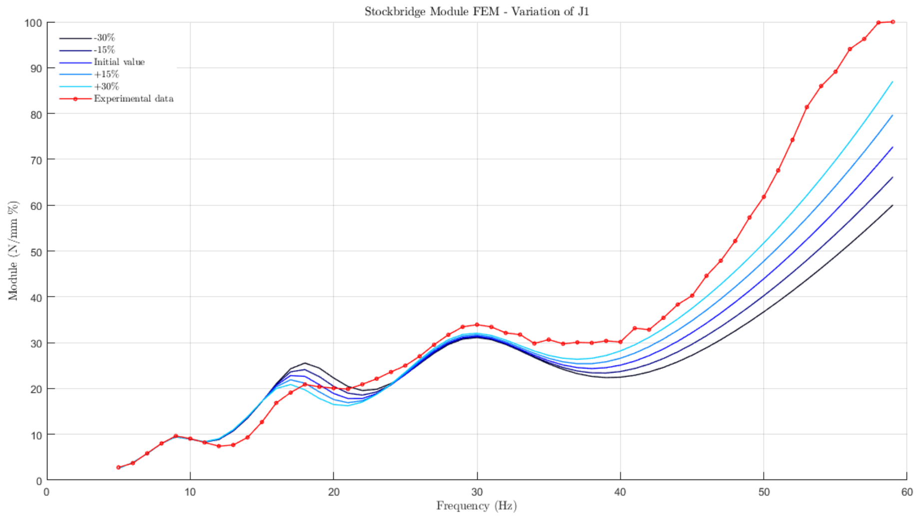

Figure 2.73: Modulus curves as a function of J_1, 5-59 Hz

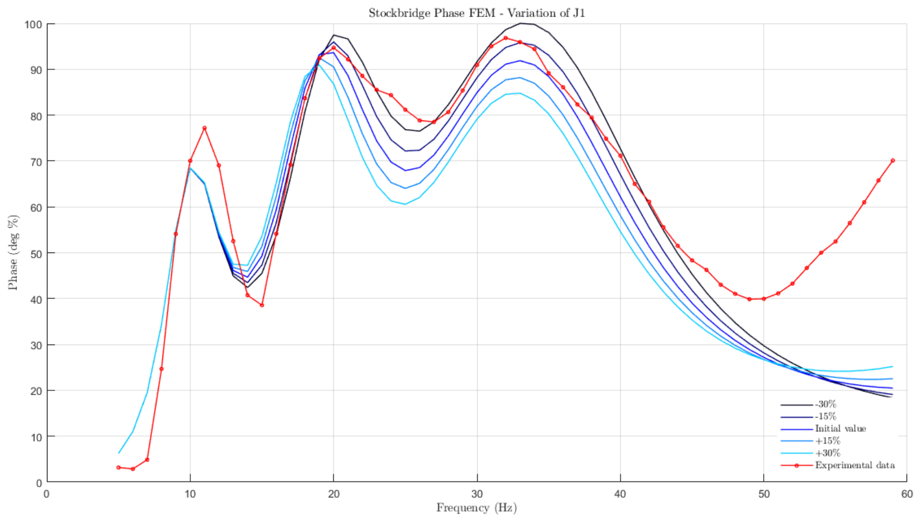

Figure 2.74: Phase curves as a function of J_1, 5-59 Hz

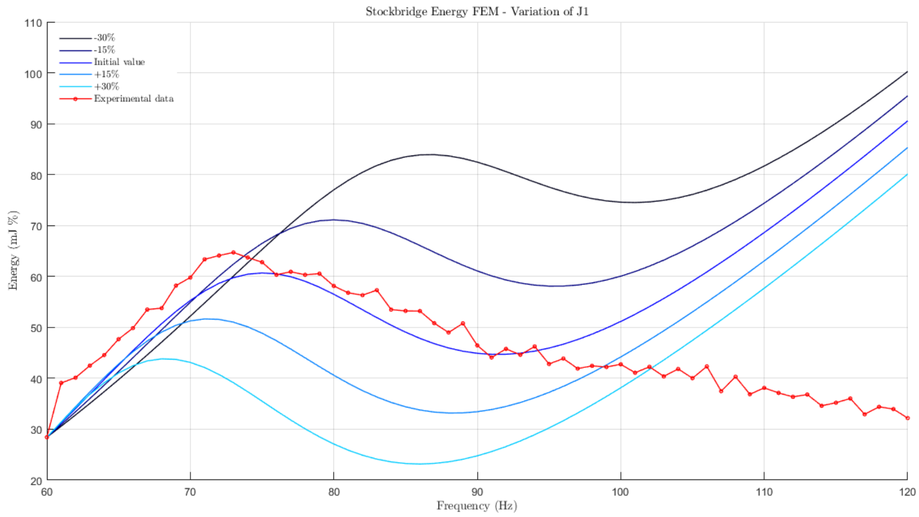

Figure 2.75: Energy curves as a function of J_1, 60-120 Hz

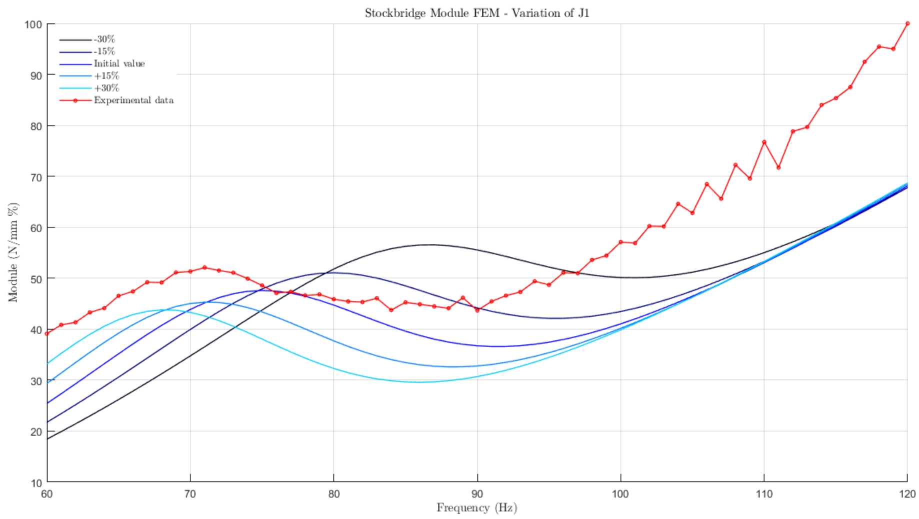

Figure 2.76: Modulus curves as a function of J_1, 60-120 Hz

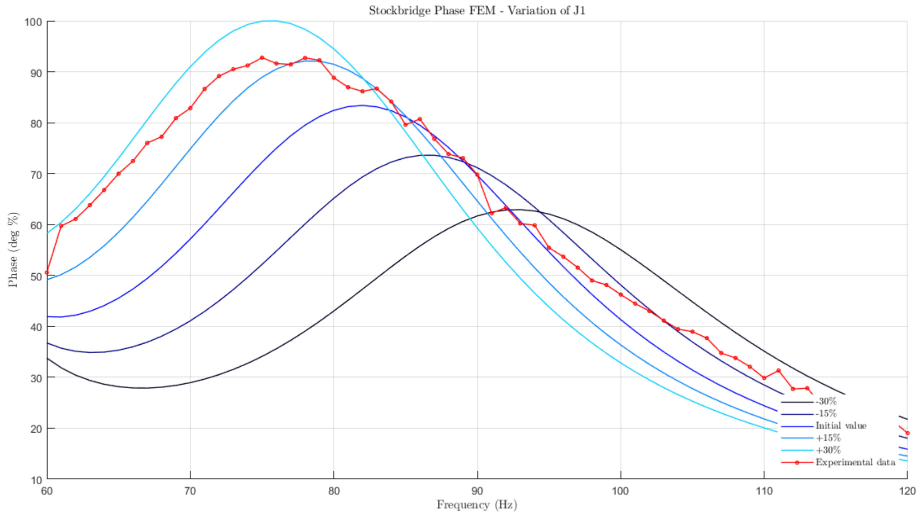

Figure 2.77: Phase curves as a function of J_1, 60-120 Hz

2.2.13 J_2 mass moment of inertia variation

The plots in this section illustrate the variations of the mass moment of inertia J_2. In the mass matrix, this parameter works similarly to mass parameter m_2.

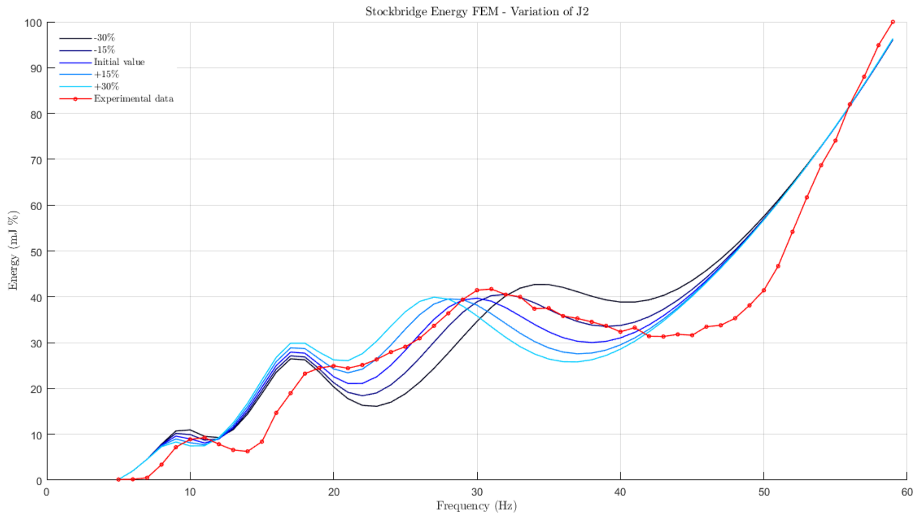

Figure 2.78: Energy curves as a function of J_2, 5-59 Hz

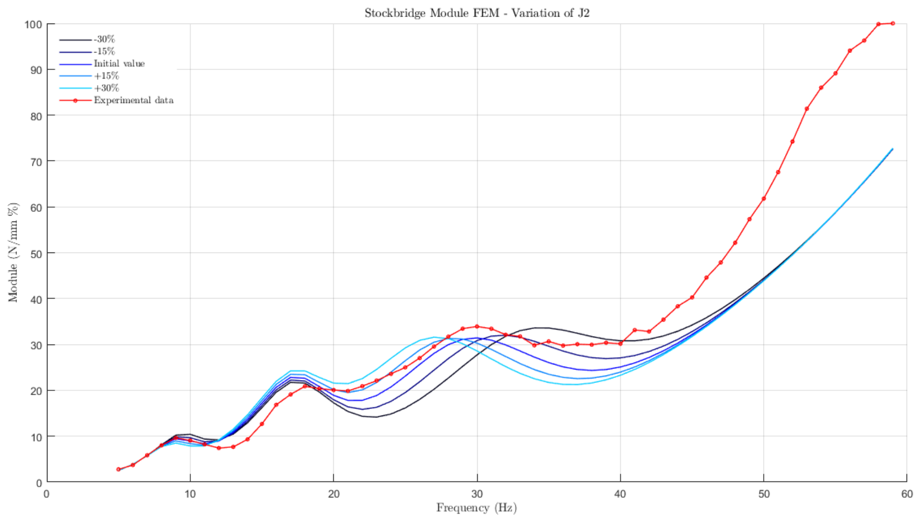

Figure 2.79: Modulus curves as a function of J_2, 5-59 Hz

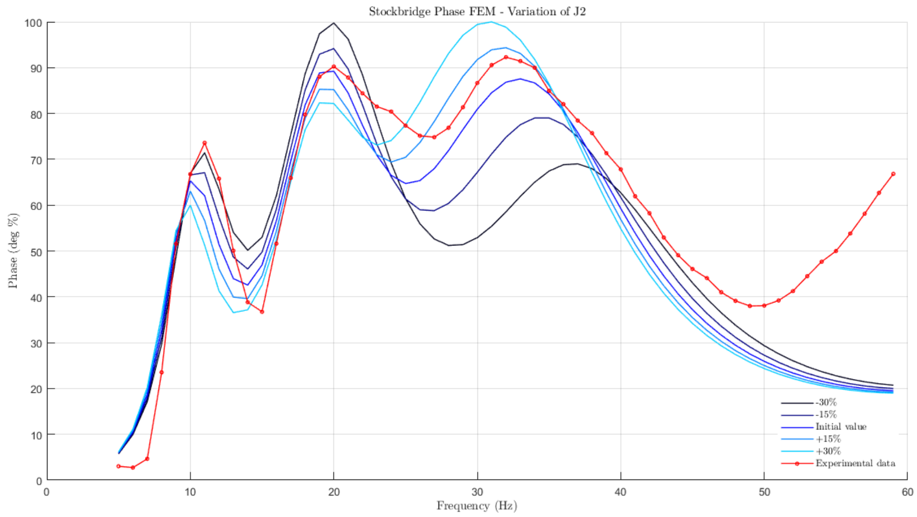

Figure 2.80: Phase curves as a function of J_2, 5-59 Hz

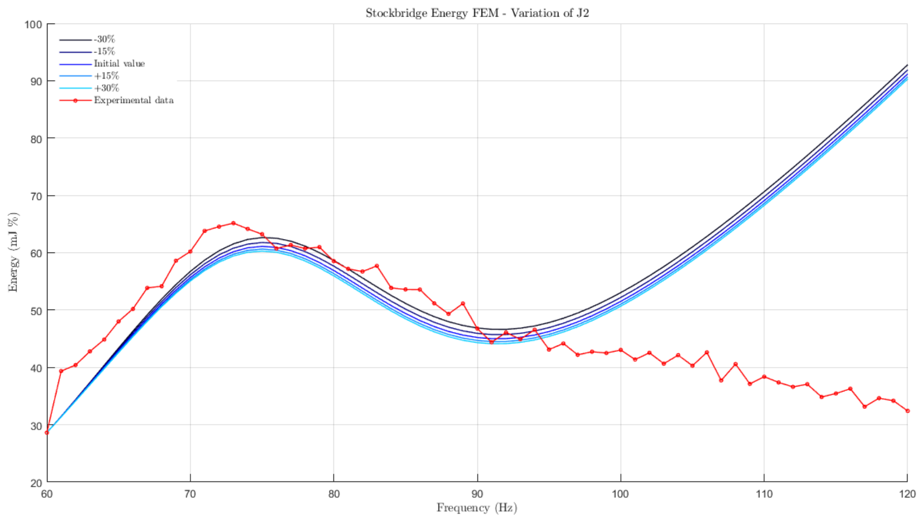

Figure 2.81: Energy curves as a function of J_2, 60-120 Hz

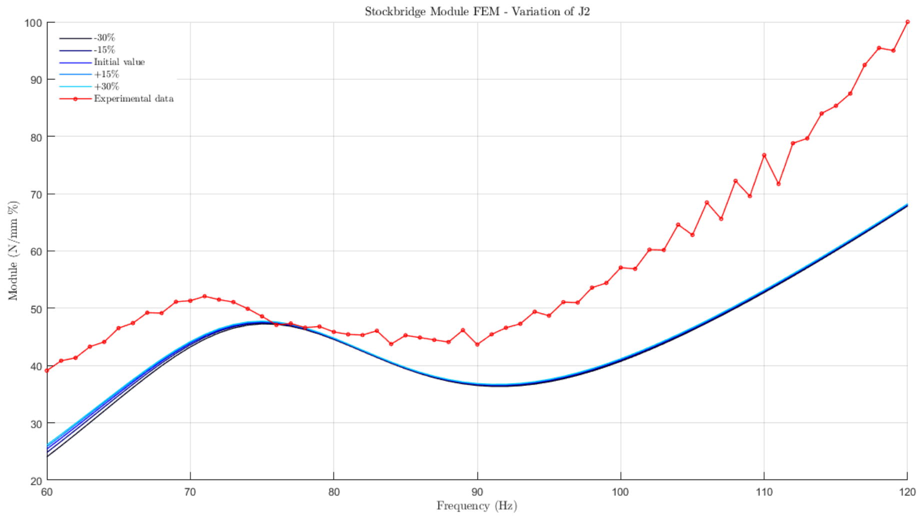

Figure 2.82: Modulus curves as a function of J_2, 60-120 Hz

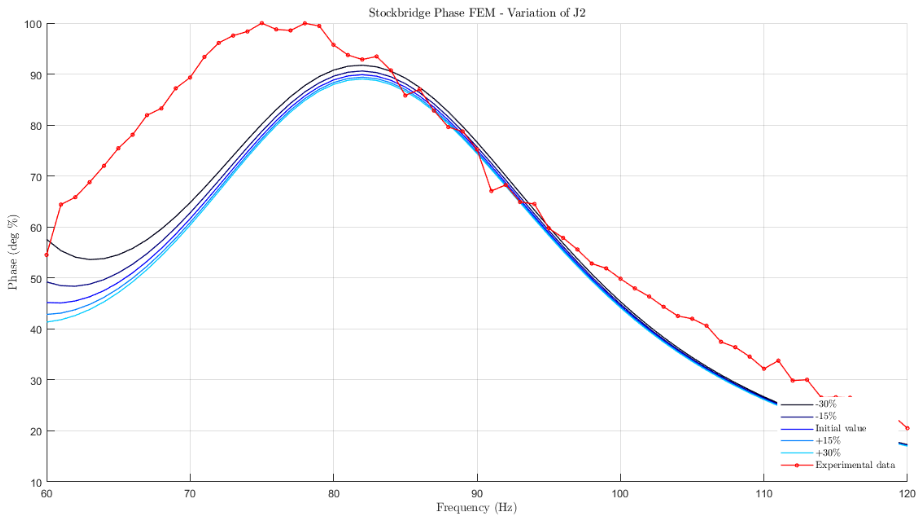

Figure 2.83: Phase curves as a function of J_2, 60-120 Hz

2.2.14 J_c mass moment of inertia

In this last part, the plots about the variation mass moment of inertia J_c are presented. In reality, however, this last parameter does not have much importance in terms of its influence on the model: after assuming that the clamp body rotation is zero, it becomes apparent that the clamp body's largeness is not a factor; the superposition of all calculated FEM curves demonstrates this.

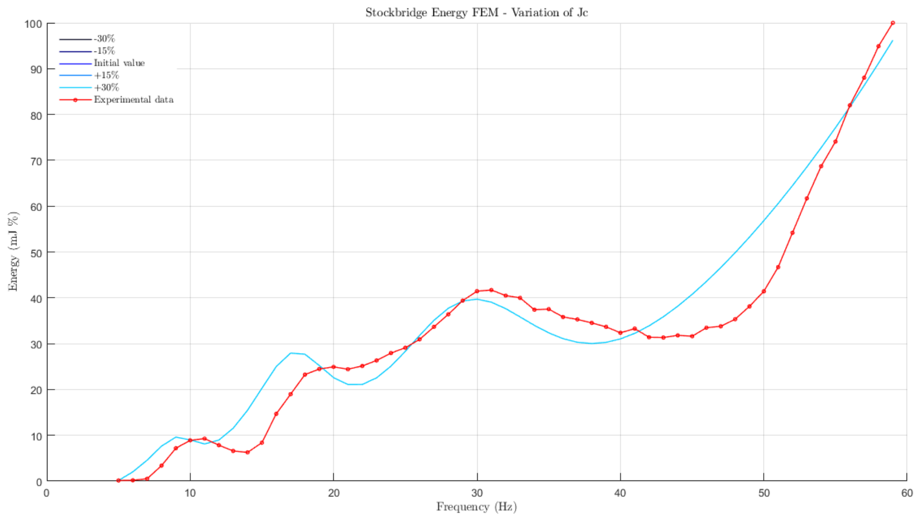

Figure 2.84: Energy curves as a function of J_c, 5-59 Hz

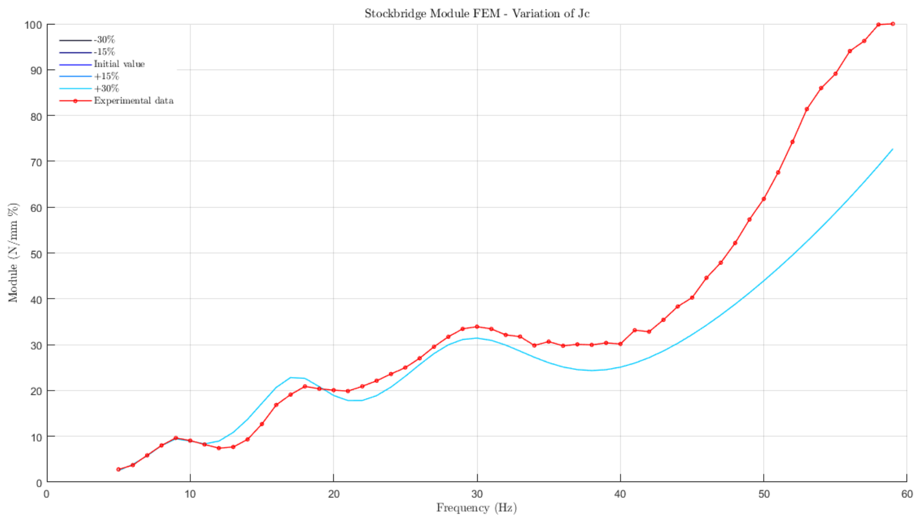

Figure 2.85: Modulus curves as a function of J_c, 5-59 Hz

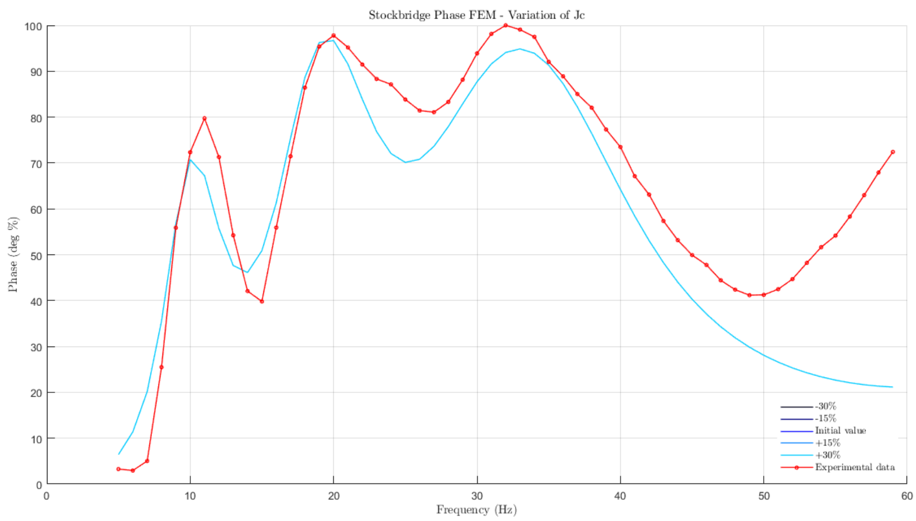

Figure 2.86: Phase curves as a function of J_c, 5-59 Hz

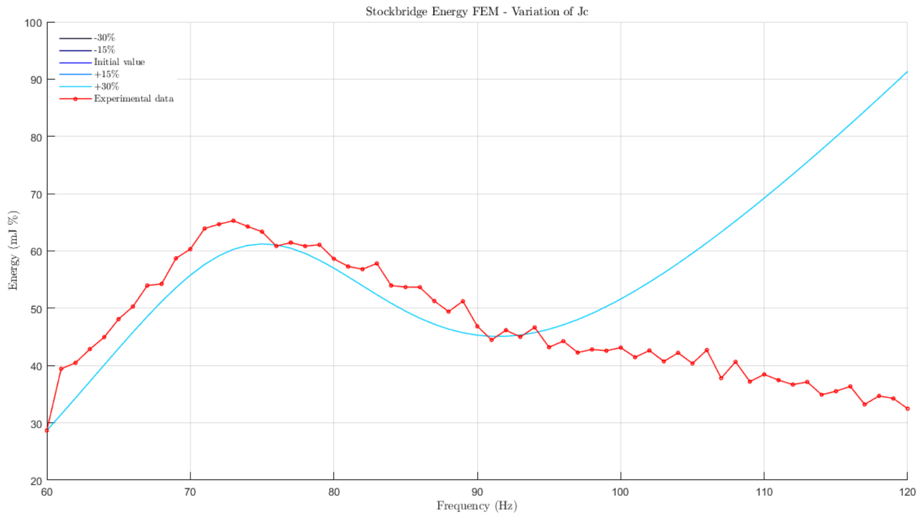

Figure 2.87: Energy curves as a function of J_c, 60-120 Hz

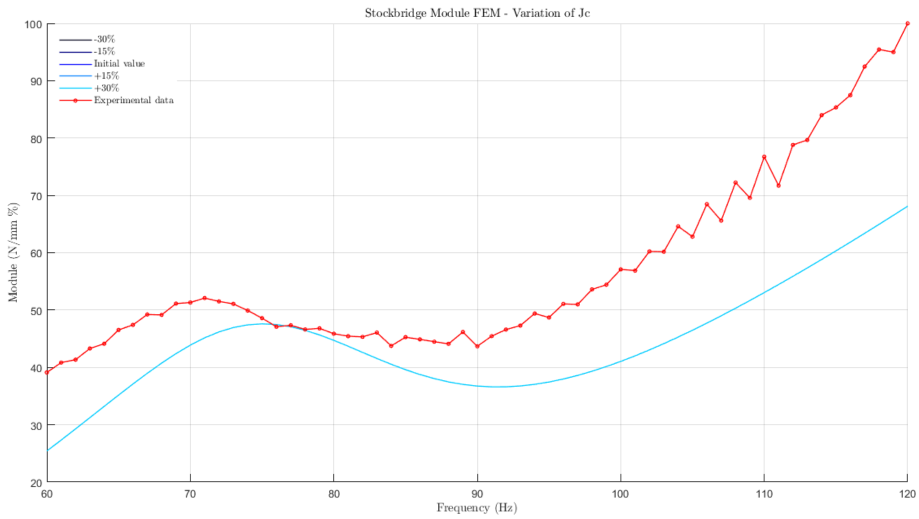

Figure 2.88: Modulus curves as a function of J_c, 60-120 Hz

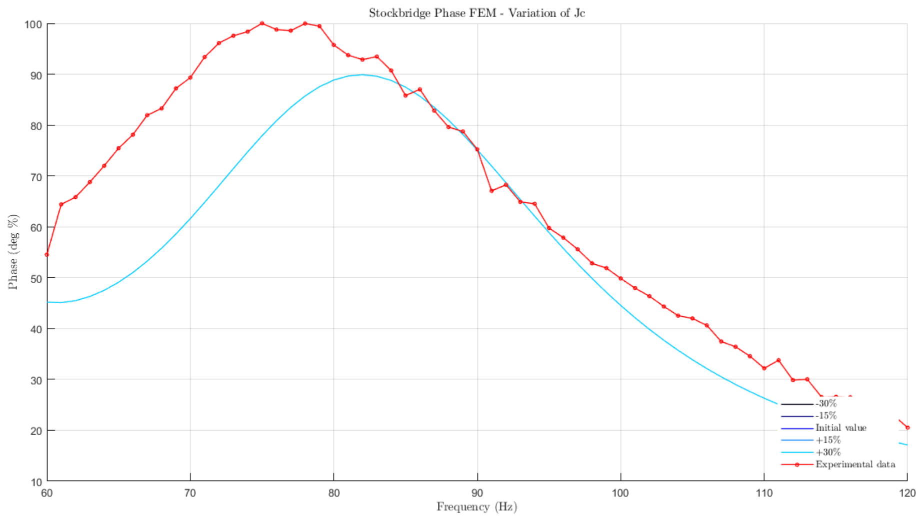

Figure 2.89: Phase curves as a function of J_c, 60-120 Hz

3. Experimental analysis

The first step of the this study is the experimental campaign. To do this, a *direct method* is used; it consists in the direct recording of the *Frequency Response Function* (FRF) of a Stockbridge damper sample that vibrates according the dynamics that the test bench imposes. To be specific, the campaign consists in the execution of n°50 measurements of the prototype damper on the shaker in the identification lab of Officina F.lli Bertolotti S.p.A..

3.1 Test Bench Description

The setup of the test bench shown in Figure 3.1 and Figure 3.2 is as follows: the damper is installed on a beam, supported by 2 load cells and fixed to the base (oscillating plate) of the vibrating table, pneumatically operated. On the base an accelerometer is also installed. The table is controlled to maintain the displacement of the base constant when the frequency varies in the measurement interval. By means of a specific software, a computer analyzes and records the signals.

Fundamental is the execution of the no-load test, with only the sensors and the joist, for calibration; in this way the only energy necessary to the actuation of the system is recorded, in order to be subtracted from the one measured on the damper system (the software requires this operation).

3.2 Measured Data Analysis

A data acquisition system records the measured forces and acceleration of the sensors and a dedicated software computes the system's FRF (module and phase) and the cycle power required by the system.

It is important to point out that the Stockbridge damper is designed according to its working range frequencies (5 - 120 Hz); this is established according to the stresses that the wind produces on the overhead lines (and therefore directly on the

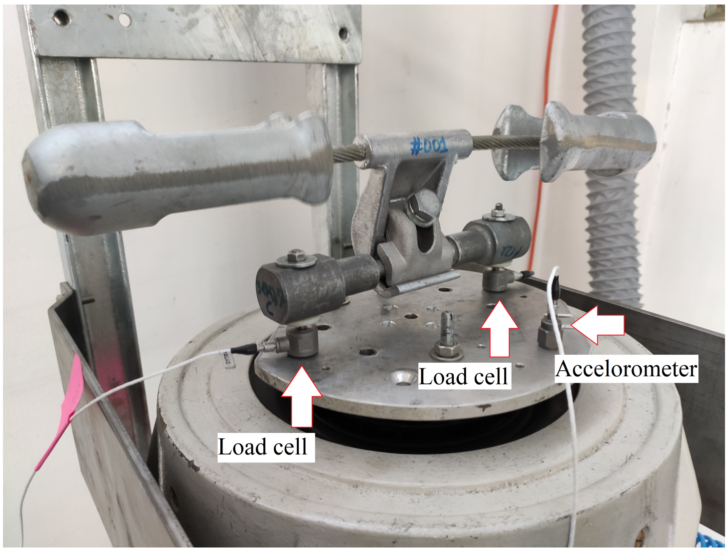

Figure 3.1: Shaker table with load cells and accelerometer


Figure 3.2: Bench test

main conductor), to the conductor size and conductor span zone. So the customer establishes the reference standard for the FRF of the damper, since he has the data of the conductor and of the line on which it is mounted (including wind maps).

3.2.1 Collected data: module and phase

The standards impose the test parameters of the damper, in terms of displacement and frequency. In the examined cases, because of the presence of a threshold frequency, the amplitude peak-peak of the sine waves is 1 mm for the 5-59 Hz frequency range and 0.5 mm for the 60-120 Hz. Hence, medium, maximum and minimum relative values curves for module and phase are obtained (Figure 3.3 and Figure 3.4).

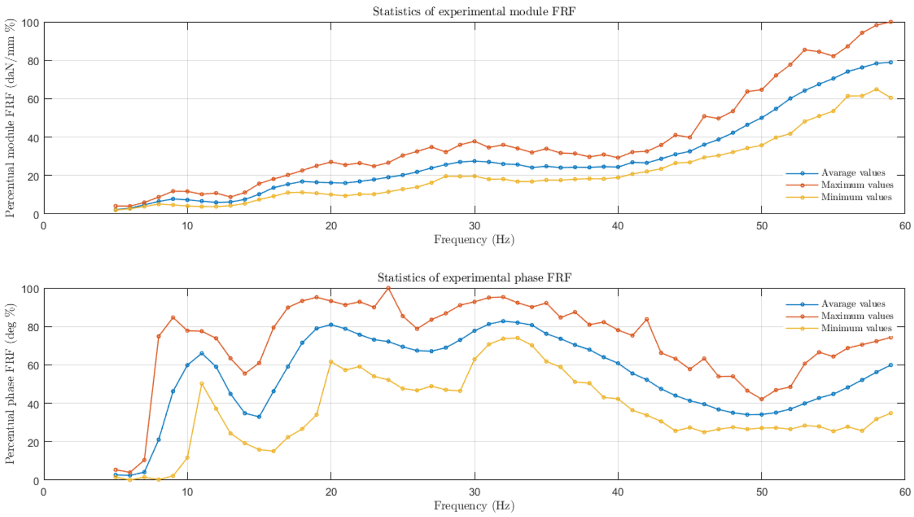

Figure 3.3: Maximum, medium, minimum relative values curves for module and phase, 5-59 Hz range

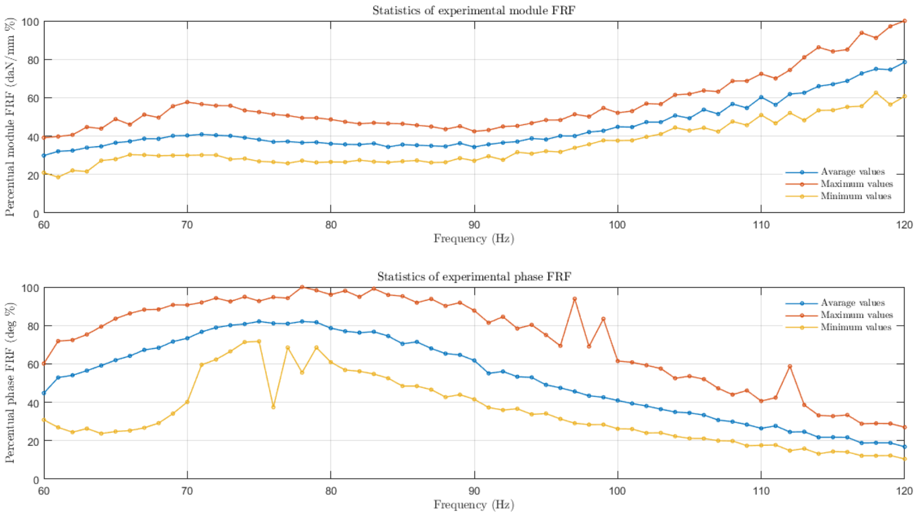

Figure 3.4: Maximum, medium, minimum relative values curves for module and phase, 60-120 Hz range

A study for the distribution of the 50 measured data at the same frequency is done; as it can be possible to see in Figure 3.5 and Figure 3.6, the type of distribution does not follow a Gaussian distribution: this can be explained because of unavoidable errors related to external conditions (weather, temperature, vibration disorders) and coupling conditions of the device on the joist, varying from one test to another.

For instance, the distributions of only a few frequencies are shown, but the trend can be tracked throughout the entire sample interval.

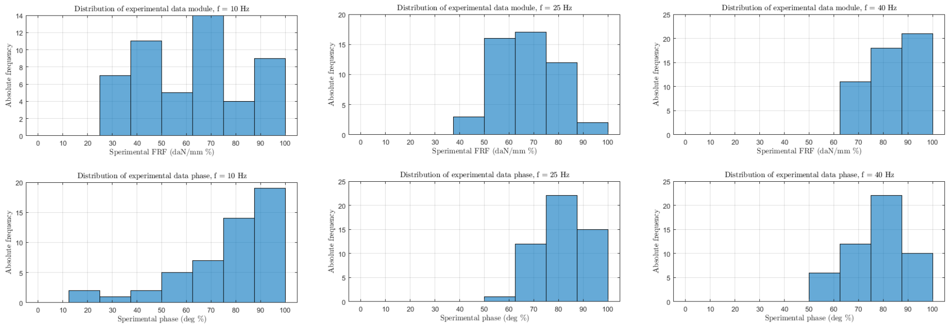

Figure 3.5: Module and phase medium values distributions; on the the left 10 Hz, in the middle 25 Hz, on the right 40 Hz

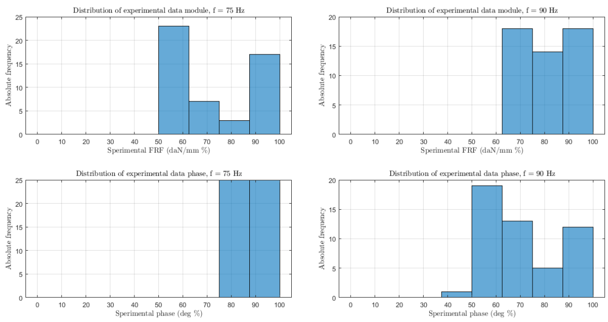

Figure 3.6: Module and phase medium values distributions; on the the left 75 Hz, on the right 90 Hz

3.2.2 Collected data: power and energy

In this section power and energy per cycle data in both 5-59 Hz and 60-120 Hz are reported. As said before, the imposed peak-peak displacement of the shaker is of 1 mm for the first interval and 0.5 mm for the second one.

The experimental power is directly captured by the sensors and recorded by the software, instead the energy associated is computed as follow:

$$E_{exp} = \frac{P_{exp}}{f} \tag{3.1}$$

Where P_{exp} is the experimental power and f is the frequency of the cycle.

At these different displacements (there is a 1:2 ratio between each other) correspond a 1:4 ratio between the first frequency range and second one, both the power and the energy.

As it is possible to see in the Figure 3.9 and Figure 3.10, by 90 Hz up to 120 Hz the measures presents a lot of noise; this because of a technological limit: for higher frequencies the test bench gives out worse measures, still these measures are reliable; also the Stockbridge damper presents some errors about its properly GDT, cause of manufacturing defects.

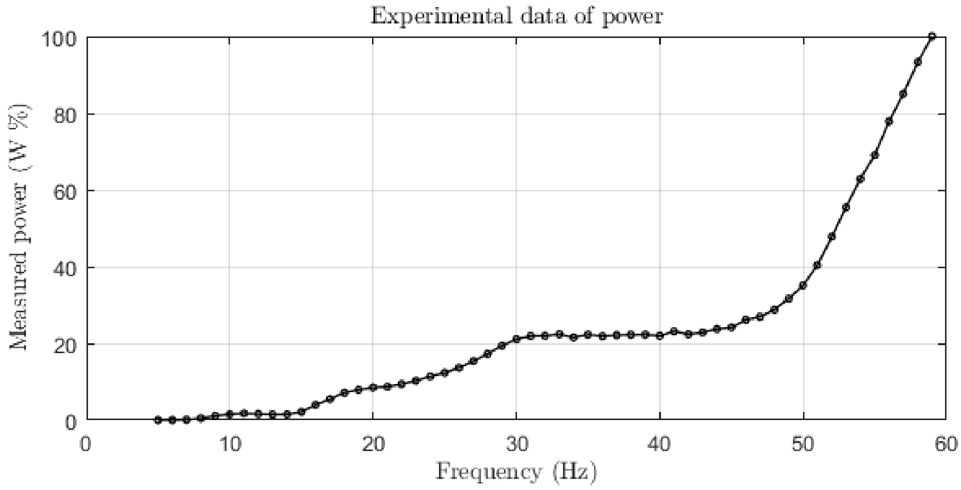

Figure 3.7: Medium relative values curves for cycle power, 5-59 Hz range

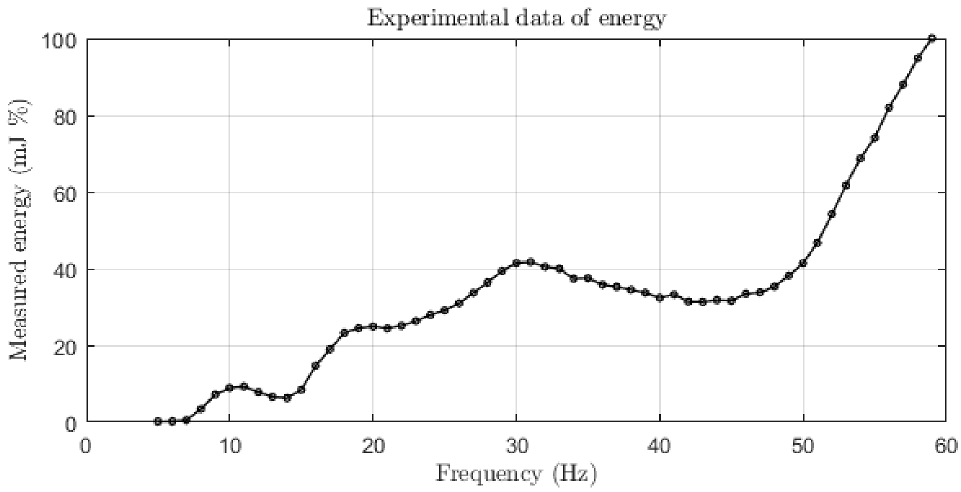

Figure 3.8: Medium relative values curves for cycle energy, 5-59 Hz range

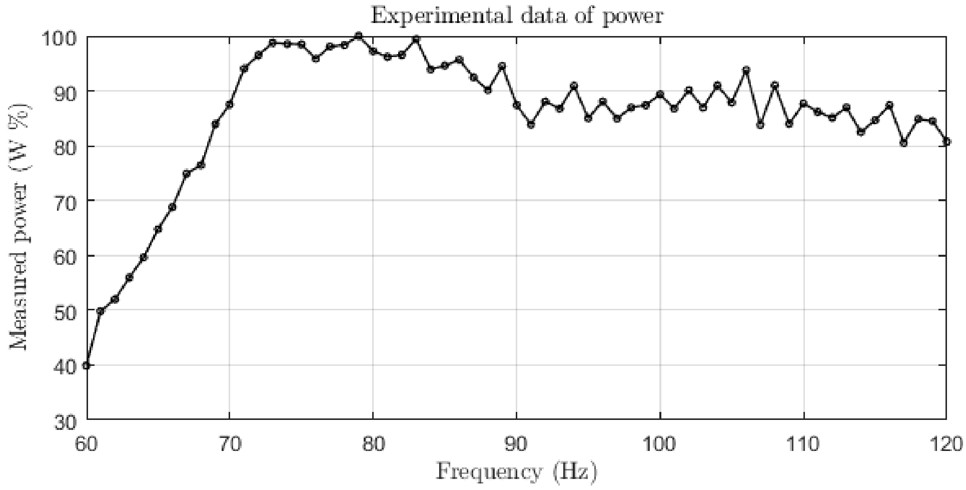

Figure 3.9: Medium relative values curves for cycle power, 60-120 Hz range

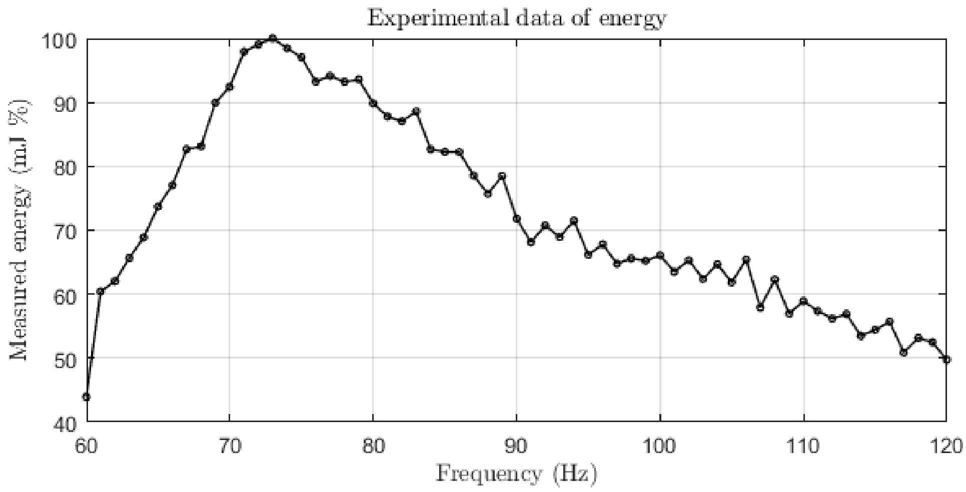

Figure 3.10: Medium relative values curves for cycle energy, 60-120 Hz range

4. Model validation

The final aim is the evaluation of flexural stiffness EI_1 and EI_2 values, as well as hysteresis coefficients h_1 and h_2, so that the curve obtained from the FEM model is inline with the experimental data. Then, on the basis of these values, the eigenfrequencies of the system and their mode shapes are computed.

4.1 Fitting

4.1.1 First Comparison between FEM Analysis and Experimental Data

Starting values of both flexural stiffness and hysteresis coefficients were assumed to define the model.

On the basis of the literature previously described, the values of EI_1 and EI_2 are assumed considering the existence domain defined by EI_{max} and EI_{min}; for simplicity they are initially assumed equal. According to the theory above, Table 4.1 presents the results of the calculations made for the messenger cable used in the system under consideration. The variables are obtained from the related inspection certificate.

$EI_{min}(Nm^2)$	$EI_{max}(Nm^2)$	$EI_1(Nm^2)$	$EI_2(Nm^2)$
2.62	52.6	10	10

Table 4.1: Flexural stiffness

As far as the hysteresis coefficients are concerned, on the basis of the results obtained with the sensitive analyses only, starting values between 0 and 1 have been assumed, which made the model more similar to the experimental data. In Table 4.2 the actual values are shown.

h_1	h_2
0.30	0.40

Table 4.2: Hysterical coefficients

4.1.2 Model Optimization

The least squares optimization is made to fit four parameters (EI_1, EI_2, h_1, h_2).

Moreover, specific graphs are constructed to evaluate the relative error between the experimental data and the model result as a function of the variation of the parameters mentioned above.

Starting from the values assigned by the literature, the following iteration is made: starting from the flexural stiffnesses, keeping the hysteresis coefficients fixed, several curves have been constructed, which refer respectively to certain values of the stiffness EI_1; having in abscissae the other stiffness, EI_2, it is possible to evaluate which are the parameters that guarantee a lower relative error. Once the corresponding values have been memorized, the same analysis is made for the hysteresis coefficients: keeping the stiffnesses fixed, different curves are put on the same graph, each of which refers to a different hysteresis coefficient h_1; having on the abscissae a span of the hysteresis coefficient h_2, it is possible to read on the ordinates the lower relative error, obtaining the hysteresis parameters associated to it. Once these coefficients are found, we start again with the search for the stiffnesses that guarantee the smallest error, as already described. The iteration continues until convergence is reached. The starting modal values of the numerical model differ in the two frequency ranges studied, since changing the peak-to-peak displacement imposed by the test bench consequently changes the dynamics involving the damper. In addition, although the flexural stiffnesses are theorized to be independent of frequency, experimental analyses show that they depend on frequency to a small degree.

Although for the frequency range $5 - 59$ Hz there is convergence for an absolute minimum error, the optimization of the parameters for the range $60 - 120$ Hz presented additional difficulties due to the high noise present in the experimental data. To circumvent this obstacle, data captured up to 90 Hz are used; the final values derived are such that a relative error of about 14% is maintained.

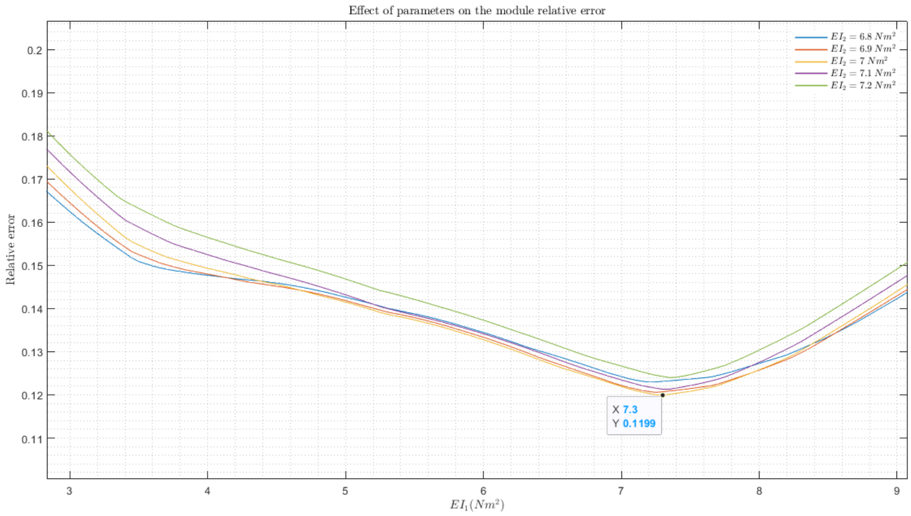

Figure 4.1: Effect of EI_1 and EI_2 on the module relative error, $5 - 59Hz$

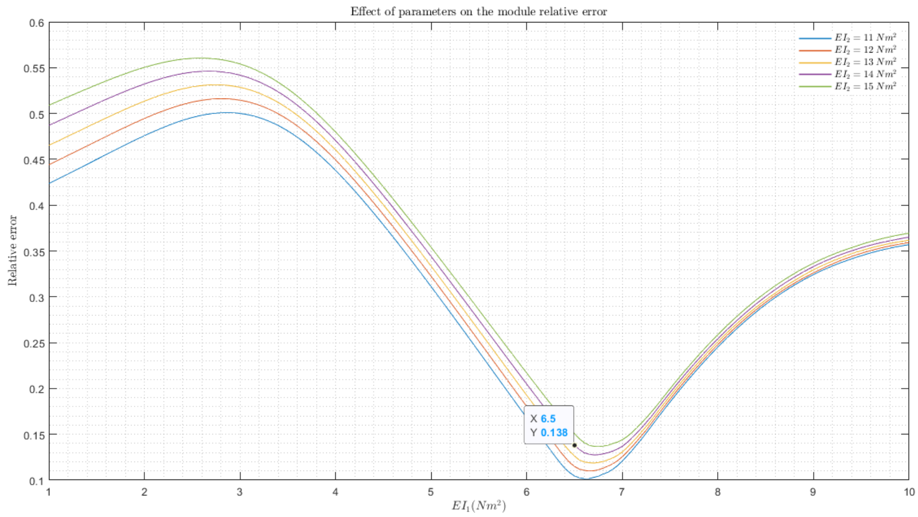

Figure 4.2: Effect of EI_1 and EI_2 on the module relative error, $60 - 120Hz$

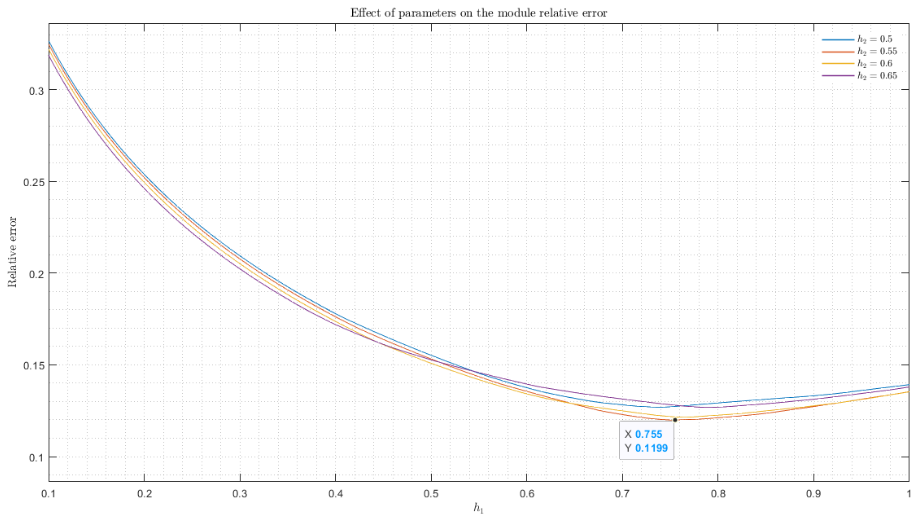

Figure 4.3: Effect of h_1 and h_2 on the module relative error, $5 - 59Hz$

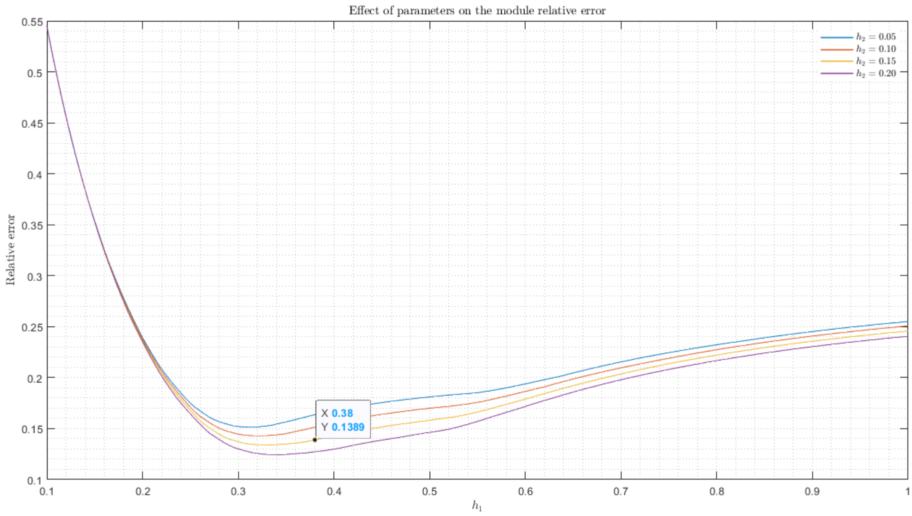

Figure 4.4: Effect of h_1 and h_2 on the module relative error, $60 - 120Hz$

In addition to this, the Figure 4.5 and Figure 4.6 show the real and imaginary numerical energy.

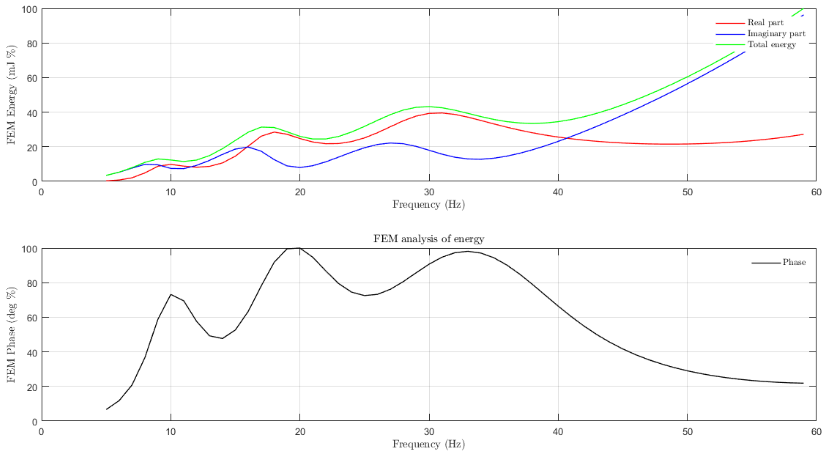

Figure 4.5: Numerical values of energy, $5 - 59Hz$

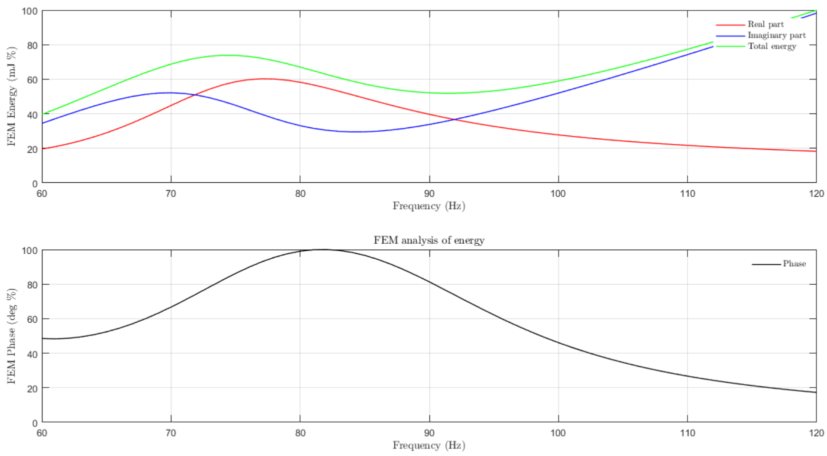

Figure 4.6: Numerical values of energy, $60 - 120Hz$

The optimal values therefore for the range $5-59Hz$ of the above parameters are reported in Table 4.3, while those concerning the characteristic developed in the range $60-120Hz$ are reported in Table 4.4.

$EI_1(Nm^2)$	$EI_2(Nm^2)$	h_1	h_2
7.3	7.0	0.755	0.550

Table 4.3: Modal parameters, range $5-59Hz$

$EI_1(Nm^2)$	$EI_2(Nm^2)$	h_1	h_2
6.5	14.0	0.375	0.150

Table 4.4: Modal parameters, range $60-120Hz$

Below are shown the graphs for the power, the energy, the module and the phase with the optimized fitting.

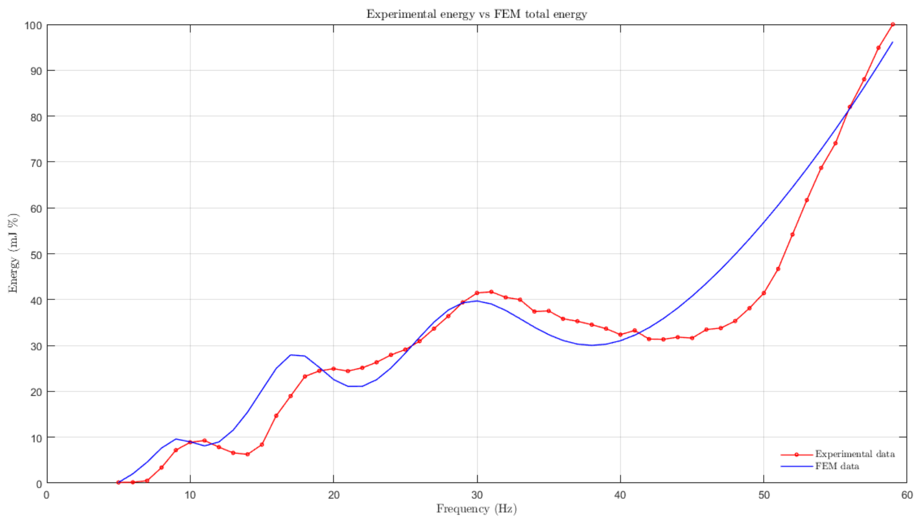

Figure 4.7: Comparison of experimental energy data and FEM energy curve, $5-59Hz$

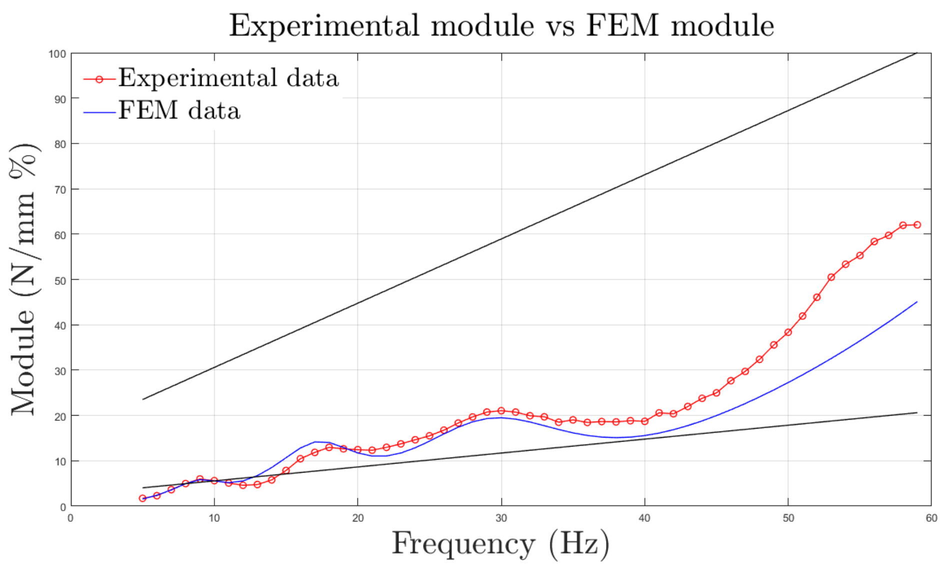

Figure 4.8: Comparison of experimental module data and FEM module curve, $5-59Hz$

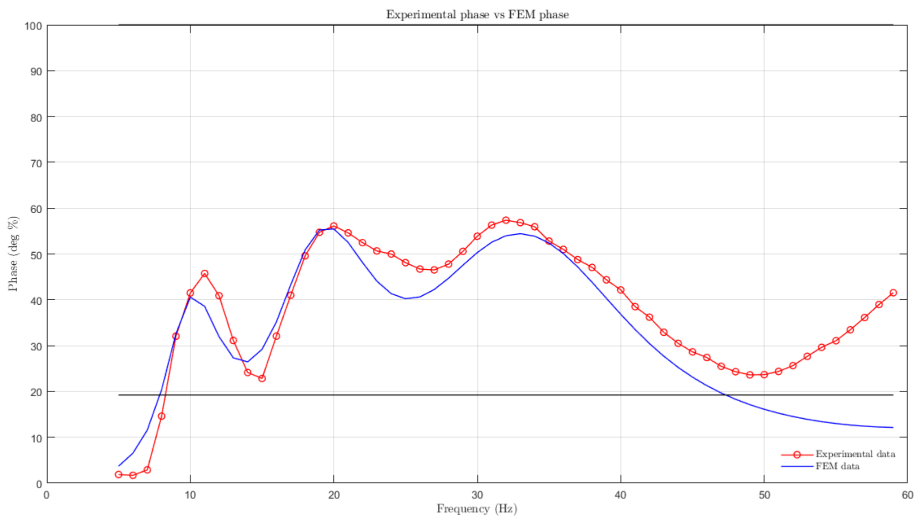

Figure 4.9: Comparison of experimental phase data and FEM phase curve, $5-59Hz$

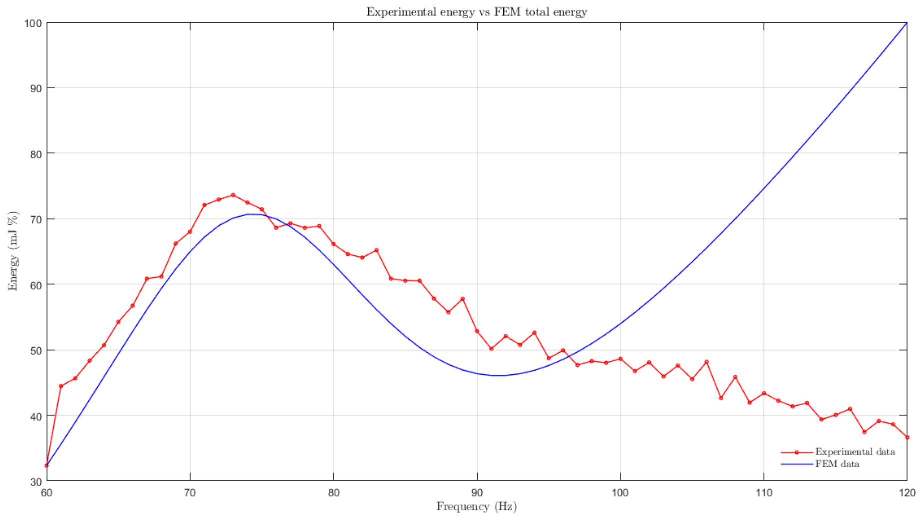

Figure 4.10: Comparison of experimental energy data and FEM energy curve, $60 - 120Hz$

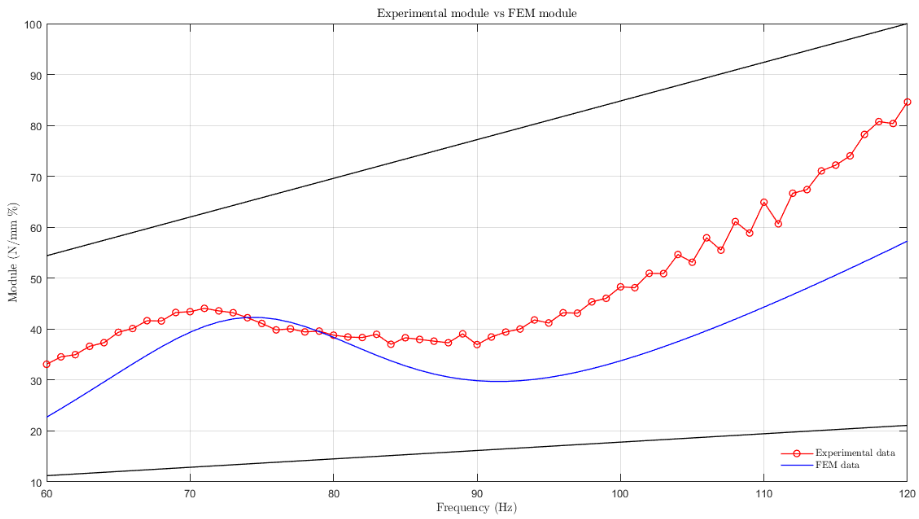

Figure 4.11: Comparison of experimental module data and FEM module curve, $60 - 120Hz$

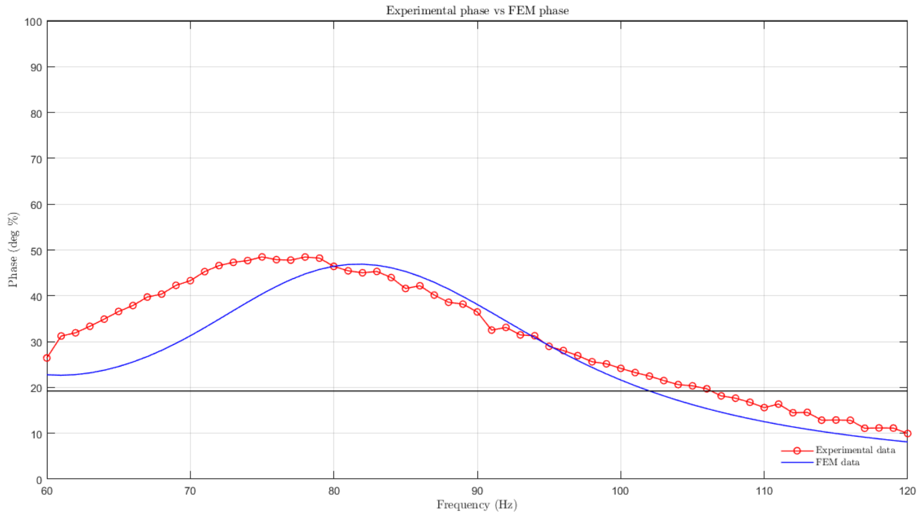

Figure 4.12: Comparison of experimental phase data and FEM phase curve, $60 - 120Hz$

4.2 System Own Frequencies

From the study of the dynamics, four frequencies of the system are detected, which therefore correspond to four mode shapes[1][2].

In the first step, the eigenvalues of the matrix governing the model are computed using Matlab. Given that there are two groups of modal parameters describing the numerical model for two different intervals, two calculations are performed; from each of them, specific frequencies that fall within the corresponding analyzed ranges are taken into consideration: the first three modal forms are placed in the range $5 - 59Hz$, while the fourth modal form is placed in the range $60 - 120Hz$.

The results are presented in Table 4.5.

[1]S. Marchesiello A. Fasana, *Meccanica delle Vibrazioni*, CLUT, Politecnico di Torino, 2006.

[2]C. Gazzola, *Modelling and assessment of aeolian vibrations of overhead transmission line conductors: theory and implementation*, PhD Thesis, Polytechnic of Milan, Italy, 2017.

$f_1(Hz)$	$f_2(Hz)$	$f_3(Hz)$	$f_4(Hz)$
8.77	16.81	28.00	73.16

Table 4.5: Resonance frequencies numerically computed

These frequencies are compared with those obtained graphically from the experimental values; from these experiences it is evident that the system needs more energy (and therefore more power) in the points where the force/displacement ratio is greater; just where the energy reaches local maximum points it is possible to identify the corresponding values of the system's own frequencies.

Following the experimental energy data plots and a summary table with these frequencies are shown.

$f_1(Hz)$	$f_2(Hz)$	$f_3(Hz)$	$f_4(Hz)$
11	20	31	73

Table 4.6: Resonance frequencies numerically computed

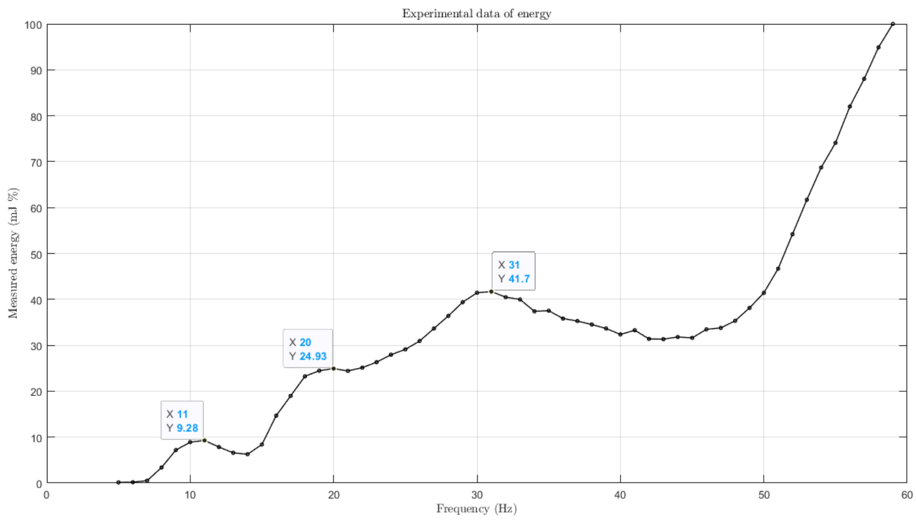

Figure 4.13: Resonance frequencies experimentally derived from the energy curve, $5 - 59Hz$

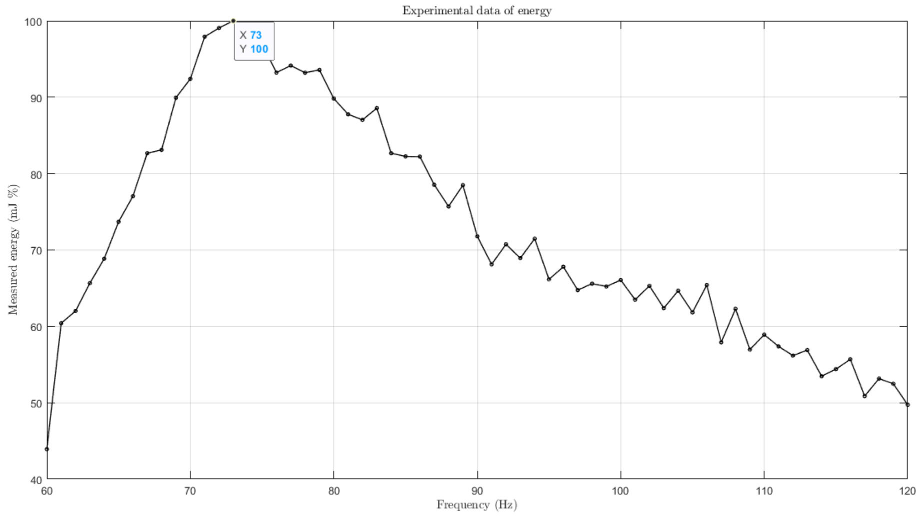

Figure 4.14: Resonance frequencies experimentally derived from the energy curve, $60 - 120Hz$

At the end the computed values are quite similar to the experimental one, so the obtained results are valid.

5. Conclusion

5.1 Final observations

As mentioned above, the objective of this study is to obtain a numerical model that interpolates effectively a set of experimental data from a Stockbridge-type fully inertial damper and to see which parameters are most influential in its dynamics.

First an improvement in the model is to be found in the use of two values of flexural stiffness of the messenger cable: although this parameter depends mainly on the section of the strands and the core of the messenger cable and the Young's modulus of the material, which are given quantities, the flexural stiffness changes in the presence of dynamic stresses because of the different friction that forms between the strands since the movement between the right and left sides is often different, resulting in two different flexural stiffness.

Through the two sets of experimental data measured with a different imposed displacement, it is possible to see that this data also takes action in the definition of the modal forms, since a vertical displacement imposed on the clamp body corresponds to a different bending of the messenger cable, which is followed by certain variations in the displacement and rotation of the cantilever masses: the greater the displacement, the more the system will tend to be in the full-slip condition, thus having lower stiffness due to lower friction.

As far as the geometrical parameters of the damper are concerned, from the sensitive analysis it is possible to understand which are those design parameters on which it is necessary to set more restrictive tolerances during the production phase.

It turns out that the distances between the center of gravity of each of the cantilever masses and the corresponding junction with the messenger cable part, a_1 and a_2, play an important role in the damper dynamics; increasing these parameters means reducing the amount of messenger cable inside the cantilever mass, thus resulting in a basically lower flexural stiffness and a basically higher phase angle between force and displacement; if, on the other hand, this length is decreased by increasing the amount of cable inside the cantilever mass, the result is a tendency to increase stiffness with a tendency to decrease the phase angle between force and displacement. These trends happen for low variations, generating important variation in the resulting FRF; for this reason, a_1 and a_2 must be controlled by means of accurate GDT.

Confirming what we have seen, the same results are also visible for the moments of inertia J_1 and J_2, as they are functions of the quantities mentioned above.

Another geometrical parameter that influences the dynamics of the damper is the mass of the clamp body m_c: it turns out that an increase in mass corresponds to a basically greater modulus of response, followed by a basically smaller phase angle; however, this parameter is of little interest at the technological level since the limits ranges in the definition of this parameter can be traced back to the standards imposed by the customer, thus reducing the space margin in which it is possible to vary the mass during production.

Appendix

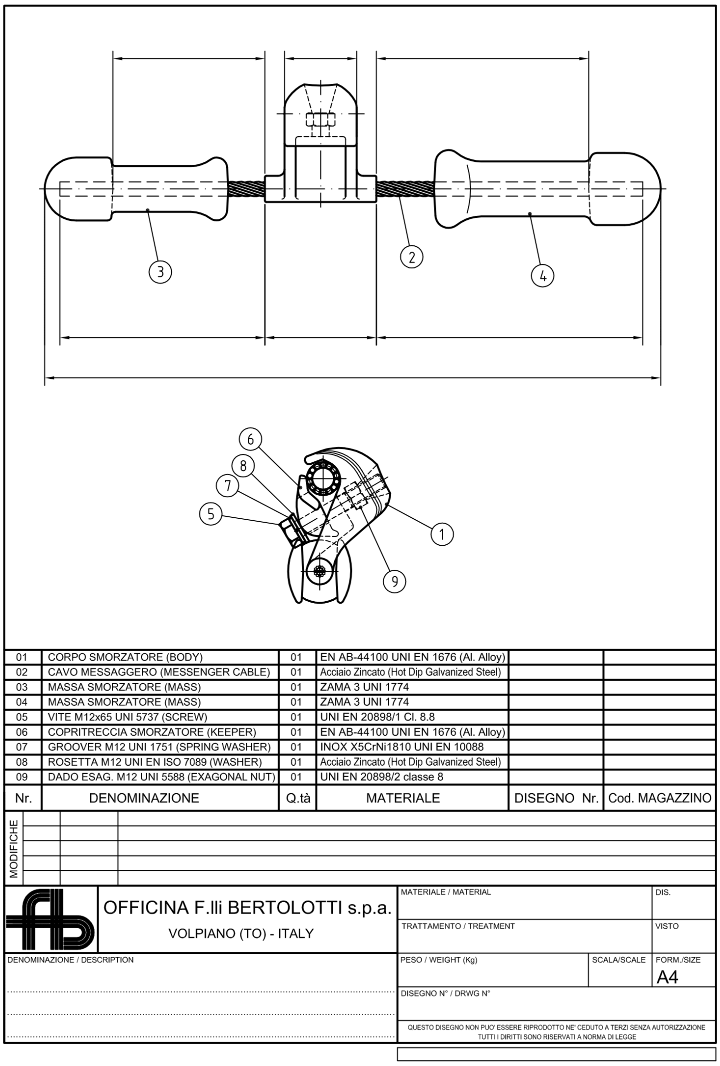

Figure 5.1: Technical drawing of the assembly

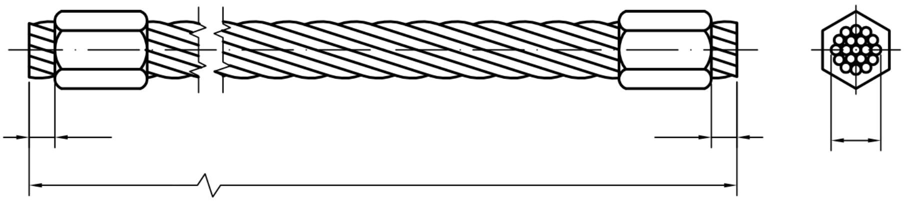

NOTE
-Dimensioni cavo:
-Materiale cavo: Acciaio zincato a caldo
-Materiale tubo: Acciaio

MODIFICHE

OFFICINA F.lli BERTOLOTTI s.p.a. VOLPIANO (TO) - ITALY	MATERIALE / MATERIAL		DIS.
	TRATTAMENTO / TREATMENT		VISTO
DENOMINAZIONE / DESCRIPTION CAVO MESSAGGERO	PESO / WEIGHT (Kg)	SCALA/SCALE 1:1	FORM./SIZE A4
	DISEGNO N° / DRWG N°		

FILE: 801_3-A-FO rev2.dwg

Figure 5.2: Technical drawing of the messenger cable

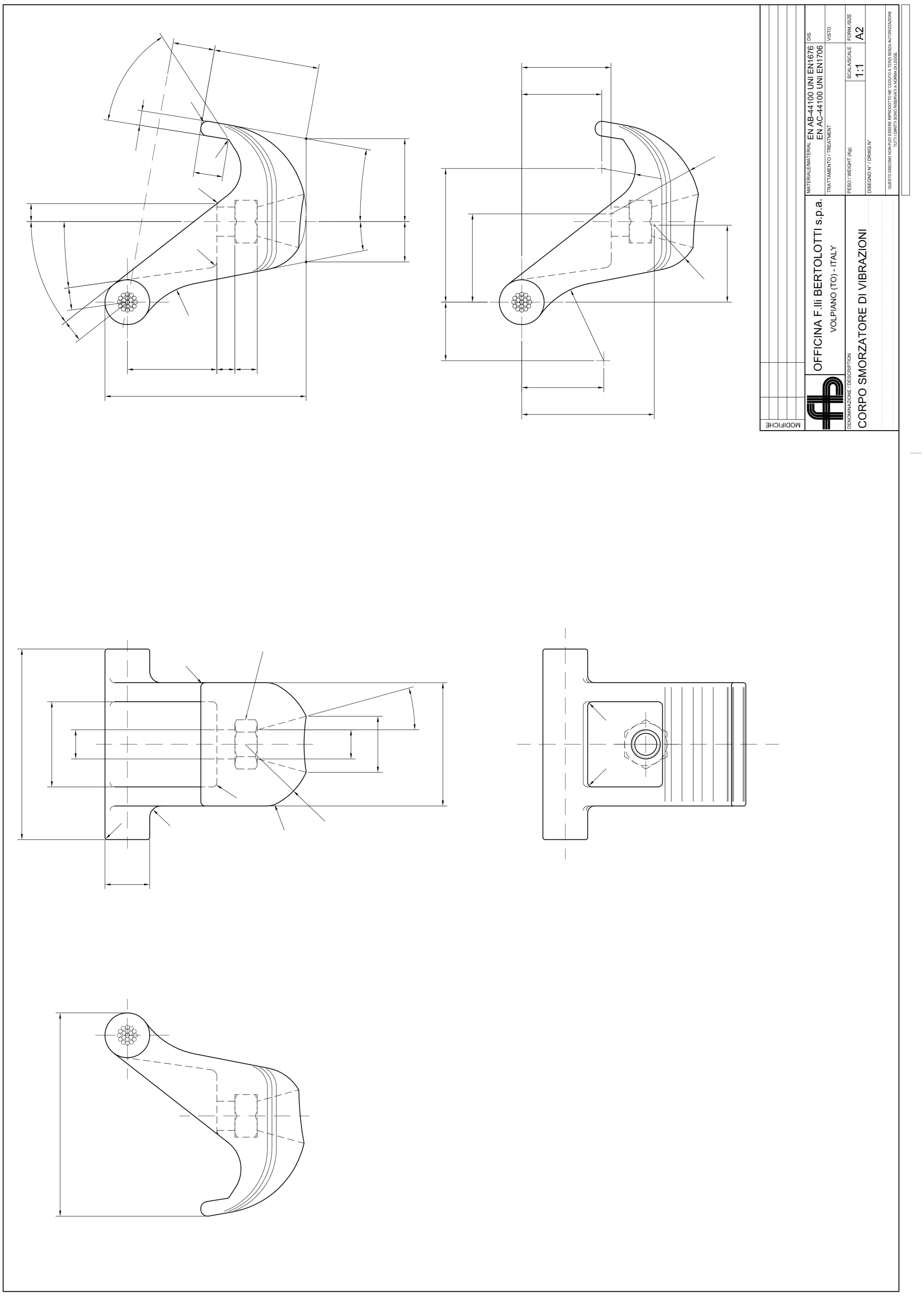

Figure 5.3: Technical drawing of the braid (body clamp part)

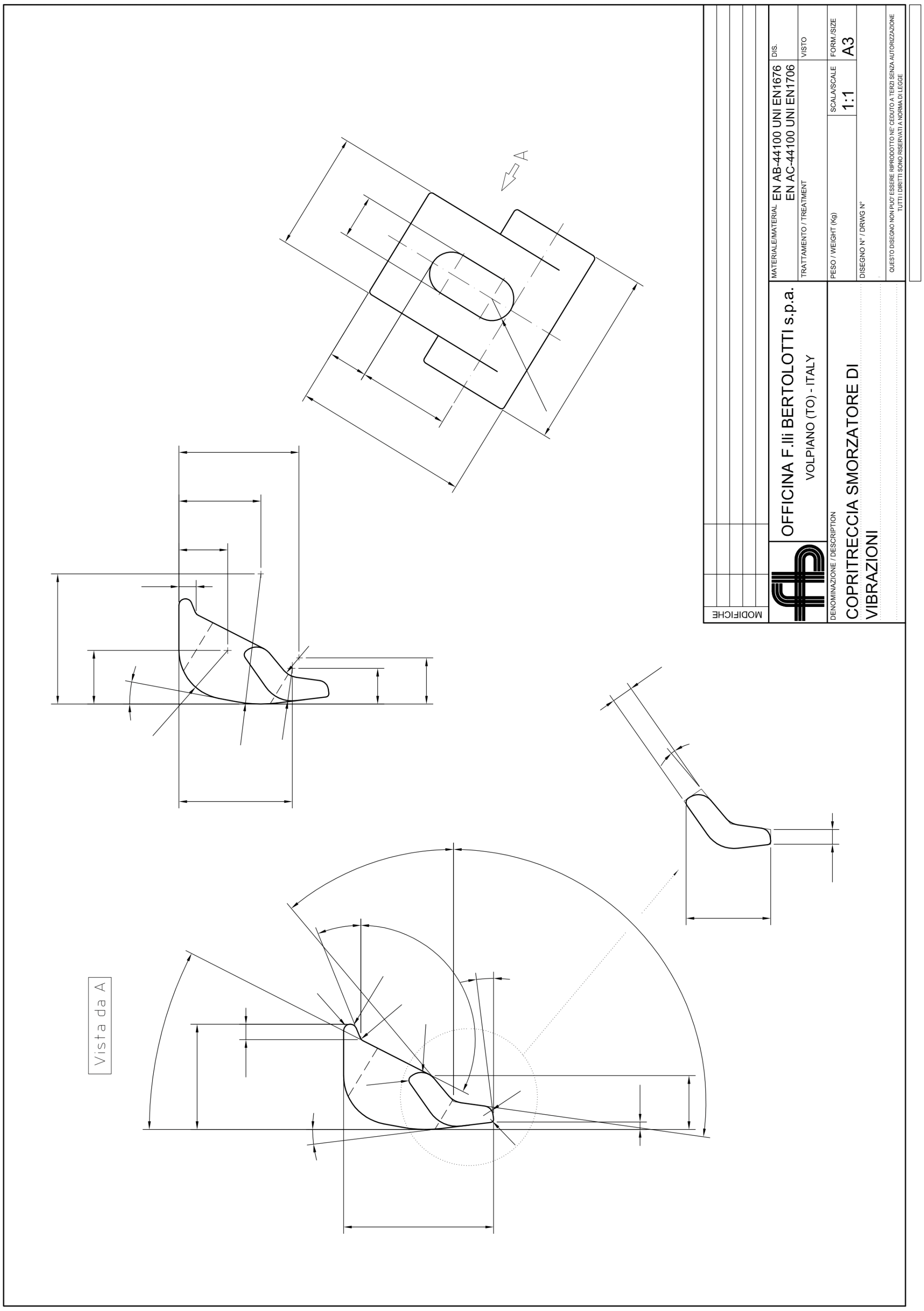

Figure 5.4: Technical drawing of the cover braid (body clamp part)

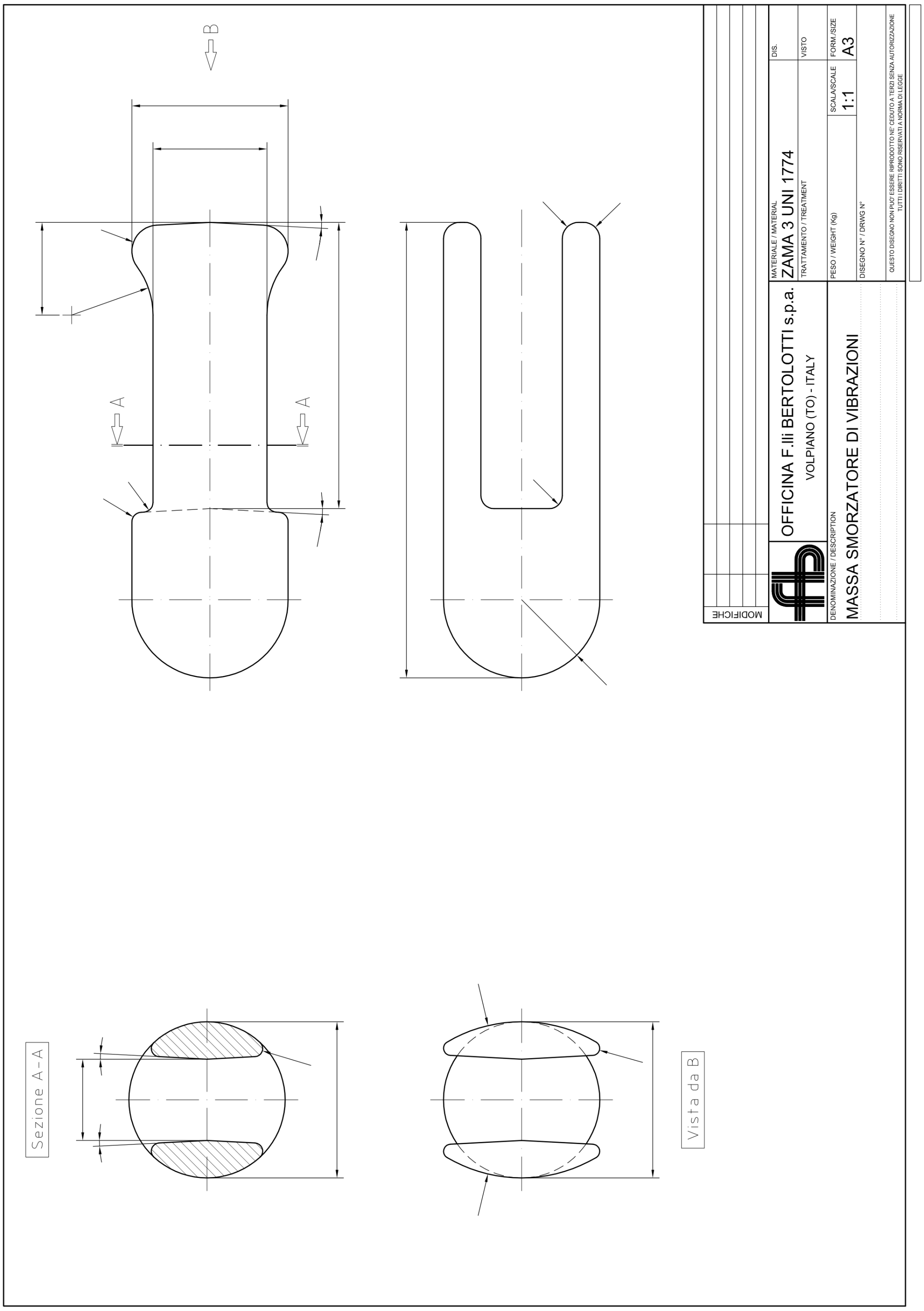

Figure 5.5: Technical drawing of the mass $m1$

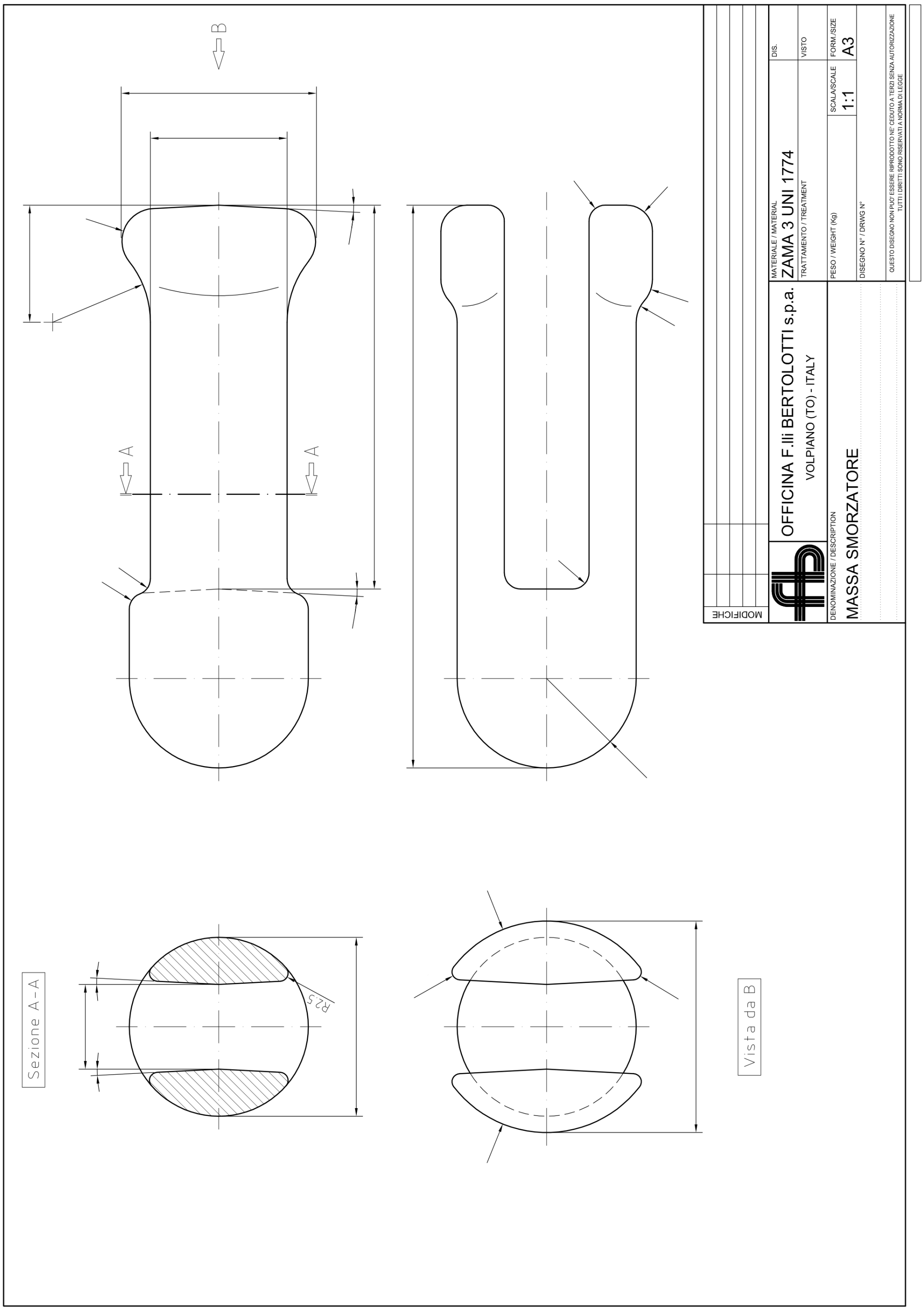

Figure 5.6: Technical drawing of the mass $m2$

Bibliography

[1] S. Marchesiello A. Fasana, *Meccanica delle Vibrazioni*, CLUT, Politecnico di Torino, 2006.

[2] C. Hardy A. Leblond, *On the estimation of a 2 x 2 complex stiffness matrix of symmetric stockbridge-type dampers*, Proc. 3rd Int. Symp. Cable Dynamics, Trondheim, Norway, 1999.

[3] C. Hardy A. Leblond, *C-J Design sensitivity analysis of a Stockbridge damper to control resonant frequencies*, Department of Mechanical Design Engineering, Pukyong National University, 2017.

[4] C.N. Canales et al., *Optimal Design of Stockbridge Dampers*, In: Ingenieria Mecanica Tecnologia y Desarollo 2, 2008, pp. 193–199.

[5] M. Ervik et al., *Report on Aeolian Vibration*, In: Electra 124, 1986, pp. 40–77.

[6] O. Barry et al., *Analytical and Experimental Investigation of Overhead Transmission Line Vibration*, In: Journal of Vibration and Control 21, 2014, pp. 2825–2837.

[7] N. Barbieri and R. Barbieri, *Linear and Non-Linear Analysis of Stockbridge Damper*, In: Proc. of the 21st Brazilian Congress of Mechanical Engineering, Natal, RN, Brazil. Ed. by Proceedings of COBEM, 2011.

[8] M. Buscemi, *Studio di un Sistema di Controllo Attivo per la Riduzione delle Vibrazioni nelle Linee Aeree di Trasmissione dell'Energia Elettrica*, MA thesis, Polytechnic of Milan, Italy, 1985.

[9] CIGRE, *Modeling of Aeolian Vibrations of a Single Conductor Plus Damper - Assessment of Technology*, CIGRE WG B2.11 TF1. Electra Vol. 223, 2005.

[10] CIGRE, *State of the Art of Conductor Galloping*, Technical Brochure no. 322. CIGRE WG TF B2.11.06, 2007.

[11] R. Claren and G. Diana, *Mathematical Analysis of Transmission Line Vibration*, In: IEEE Transactions on Power Apparatus and Systems 88, 1969, pp. 1741–1771.

[12] CTC Global Corporation, *Engineering Transmission Lines With High-Capacity, Low-Sag ACCC Conductor*, CTC Global, 2011.

[13] D.G. Watts D. M. Bates, *Nonlinear Regression Analysis and Its Applications*, Wiley Series in Probability and Statistics, John Wiley Sons Inc, 2007.

[14] S. Singh D. Prasad and G. Agarwal, *Design and Testing of Stockbridge Vibration Dampers*, Electrical India, 2009.

[15] Electric Research Power Institute EPRI, *Transmission Line Reference Book: Wind- Induced Conductor Motion*, Palo Alto, 2006.

[16] Donald G. Fink and H. Wayne Beaty, *Overhead Power Transmission". Standard Handbook for Electrical Engineers (11 ed.)* New York: McGraw-Hill, 1978.

[17] F. Foti and L. Martinelli, *Finite Element Modeling of Cable Galloping Vibrations. Part II: Application to an Iced Cable in 1:2 Multiple Internal Resonance*, In: Journal of Vibration and Control 24, 2016, pp. 1322–1340.

[18] F. Foti and L. Martinelli, *Mechanical Modeling of Metallic Strands Subjected to Tension, Torsion and Bending*, n: International Journal of Solids and Structures 91, 2016, pp. 1–17.

[19] F. Foti and L. Martinelli, *Hysteretic Behaviour of Stockbridge Dampers: Modelling and Parameter Identification*, In: Mathematical Problems in Engineering, 2018.

[20] N. Amati G. Genta, *On the equivalent viscous damping for systems with hysteresis*, Trabalho de Conclusão de Curso, Universidade Tecnológica Federal do Paraná, Curitiba, 2018.

[21] C. Gazzola, *Modelling and assessment of aeolian vibrations of overhead transmission line conductors: theory and implementation*, PhD Thesis, Polytechnic of Milan, Italy, 2017.

[22] P. Hagedorn, *Wind-Excited Vibrations of Transmission Lines: A Comparison of Different Mathematical Models*, In: Mathematical Modelling 8, 1987, pp. 352–358.

[23] J.P. Den Hartog, *Mechanical Vibrations*, Dover Publications, 1985.

[24] B.C. De Jong, *Analytical and experimental analysis of the capacity of steel wire ropes subjected to forced bending*, M.Sc Thesis submitted to the faculty of Civil Engineering and Geoscience, TU Delft, 2015.

[25] H. Kasap, *Investigation of Stockbridge Dampers for Vibration Control of Overhead Transmission Lines*, MSc Thesis, Middle East Technical University, Turkey, 2012.

[26] S. Langlois and F. Legeron, *Prediction of Aeolian Vibration on Transmission-Line Conductors Using a Nonlinear Time Hystory Model - Part I: Damper Model*, In: IEEE Transactions on Power Delivery 29, 2012, pp. 1168–1175.

[27] S. Langlois and F. Legeron, *Prediction of Aeolian Vibration on Transmission-Line Conductors Using a Nonlinear Time Hystory Model - Part II: Conductor and Damper Model*, In: IEEE Transactions on Power Delivery 29, 2014, pp. 1176–1183.

[28] V.J.Z. Merino M.E. Marchi, *Análise dinâmica de amortecedores tipo stockbridge*, Trabalho de Conclusão de Curso, Universidade Tecnológica Federal do Paraná, Curitiba, 2014.

[29] L. Meirovitch, *Elements on vibration analysis*, College of Engineering, Virginia Polytechnic Institute and State University, 1986.

[30] M. Onore, *Smorzatore Stockbridge e soppressione delle vibrazioni dei cavi tesi: analisi numerica e sperimentale*, Polytechnic of Turin, 2018.

[31] J. Slegers, *Transmission Line Loading: Sag Calculations and High-Temperature Conductor Technologies*, Iowa State University, 2011.

[32] J. Vecchiarelli, *Aeolian Vibration of a Conductor with a Stockbridge – Type Damper*, PhD Thesis, University of Toronto, Canada, 1997.

[33] B. Wareing, *Types and Uses of High Temperature Conductor*, CIGRÉ (International Council on Large Electric Systems) Seminar. Bangkok: CIGRÉ Study Committee B2 Working group 11, 2011.

[34] Liang Wang Xiaoyu Luo and Yisheng Zhang, *Nonlinear numerical model with contact for Stockbridge vibration damper and experimental validation*, Journal of Vibration and Control, 2014.

Websites links

[1] D. Bryant, *ACSR and ACCC,* 3 September 2013, in https://bit.ly/3HRLzrs.

[2] A. Cardou, *Taut Helical Strength Bending Stiffness,* 2006, in http://www.utfscience.deI/2006.

[3] Spedona/J.H. Mora, *Lignes à haute tension (Sagy, Val d'Oise),* 16 June 2005, in https://bit.ly/34UxhaU.